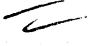


THE UNIVERSITY OF MICHIGAN
INDUSTRY PROGRAM OF THE COLLEGE OF ENGINEERING

DRAG COEFFICIENTS OF INERT, BURNING, OR
EVAPORATING PARTICLES ACCELERATING IN GAS STREAMS

Clayton T. Crowe


A dissertation submitted in partial fulfillment
of the requirements for the degree of
Doctor of Philosophy in The
University of Michigan
Department of Aeronautical Engineering
1961

December, 1961

IP - 544

en 8m

UMR0819

Doctoral Committee:

Professor Richard B. Morrison, Chairman
Associate Professor Thomas C. Adamson, Jr.
Associate Professor Arthur G. Hansen
Associate Professor William Mirsky
Associate Professor James A. Nicholls

PREFACE

The advent of highly metallized solid propellant rocket fuels has created a renewed interest in the study of two phase flow. Small metal oxide particles formed upon combustion and subsequently entrained in the exhaust gases will reduce the rocket's specific impulse as a result of the particle-gas temperature and velocity lags. In the design of a rocket to employ such a fuel, it is most imperative to be able to estimate the specific impulse loss which, in turn, requires information concerning the particles' drag coefficients.

The fact that the particles are small, burning and entrained in highly accelerated gases suggests the importance of Reynolds number, acceleration modulus, dimensionless burning rate, Mach number, and Knudsen number in the determination of the drag coefficients. This particular study, however, deals only with the first three parameters as a preliminary effort in the solution of the complete problem.

The present study further restricts itself to Reynolds numbers ranging from 250 to 1600. Actually the particle in a rocket nozzle may experience Reynolds numbers extending from the Stokes's flow regime ($Re \approx 1$) to orders of a thousand. It is felt, however, that the Reynolds number range considered in this study is the most important since the most critical portion of a particle's trajectory is in the throat region where the Reynolds numbers are large. For Reynolds numbers exceeding those considered in this study it is felt that the effect of burning will be less significant. However, further studies are required to investigate burning effects in the smaller Reynolds number regimes where the boundary layer thickness becomes the same order of magnitude as the particle's diameter.

Grant NsG-86-60 from the National Aeronautics and Space Administration and an Institute of Science and Technology Fellowship provided financial support for this study. This support is deeply appreciated.

The author would like to sincerely thank the members of his doctoral committee for their helpful suggestions and criticisms. In particular he is most indebted to Professor R. B. Morrison who suggested the study and continually provided suggestions and encouragement and to

Professor J. A. Nicholls who so often gave most freely of his time. In addition the author would like to thank Dr. R. D. Ingebo of NASA's Lewis Research Center for fruitful discussions concerning the problem.

Messrs. Peter Kirschner and Paul Willoughby drew many of the original figures and performed many of the calculations. The original manuscript was typed by Miss Louis Olshansky. Mr. Cletus Iott assisted with the electronic instrumentation while Mr. Harry Orr assisted with the shock tube construction. The author would like to thank these people as well as other staff members of the Aircraft Propulsion Laboratory for their efforts.

The author also wishes to thank the Industry Program of the University of Michigan for their preparation of the final manuscript.

Finally the author is indebted to his parents whose guidance, encouragement, and support through the years of study were indispensable.

TABLE OF CONTENTS

	<u>Page</u>
PREFACE.....	ii
LIST OF TABLES.....	vii
LIST OF FIGURES.....	viii
NOMENCLATURE.....	x
ABSTRACT.....	xiv
I. INTRODUCTION.....	1
1.1 Origination of Problem.....	1
1.2 Review of Studies Concerned with Problem.....	4
1.3 Purpose of this Study.....	6
1.4 Experimental and Analytical Work Pertaining to Particle Drag Coefficients.....	7
1.5 Reynolds Number Range of Interest.....	10
II. EQUATIONS OF MOTION FOR A PARTICLE WITH MASS FLUX THROUGH THE SURFACE.....	12
III. EXPERIMENTAL ARRANGEMENT AND PROCEDURE.....	16
3.1 Choice of Experimental Facility.....	16
3.2 Description and Design of Experimental Set-Up.....	16
3.2.1 Shock Tube and Driver Section.....	18
3.2.2 Test Section.....	20
3.2.3 Optical Bench.....	23
3.2.4 Particle Injection System.....	25
3.2.5 Wave Speed Recording System.....	25
3.2.6 Sequence Timing System.....	30

TABLE OF CONTENTS (CONT'D)

	<u>Page</u>
3.3 Experimental Procedure.....	31
IV. DATA REDUCTION AND ERROR ANALYSIS.....	34
4.1 Scope of Experimental Results.....	34
4.2 Data Reduction Equations.....	36
4.3 Typical Example of Data Reduction.....	39
4.4 Error Analysis.....	48
V. THEORETICAL ANALYSIS.....	53
5.1 Scope of Analysis.....	53
5.2 Basic Equations.....	53
5.3 Evaluation of Integrals.....	60
5.4 Steady State Drag Coefficient for a Sphere.....	61
5.5 Rate of Evaporation of Spherical Drop in Steady Flow..	67
5.6 Effect of Evaporation on Drag Coefficient.....	74
5.7 Effect of Burning on Drag Coefficient.....	81
5.8 Effect of Acceleration on Drag Coefficient.....	94
VI. DISCUSSION OF THEORETICAL AND EXPERIMENTAL RESULTS.....	99
6.1 Comparison of Present Experimental and Theoretical Results.....	99
6.2 Comparison of Present Results with those of Other Ex- periments.....	101
6.2.1 Torobin and Gauvin's Data.....	101
6.2.2 Ingebo's Data.....	104
6.2.3 Rabin's Data.....	108

TABLE OF CONTENTS (CONT'D)

	<u>Page</u>
6.2.4 Hanson's Results.....	109
6.2.5 Balloon Experiments.....	110
6.2.6 Bolt's Results.....	111
VII. CONCLUSIONS.....	112
7.1 Reynolds Number Effect.....	112
7.2 Acceleration Modulus Effect.....	112
7.3 Evaporation Effect.....	113
7.4 Burning Effect.....	113
7.5 Application to Rocket Exhaust Problem.....	114
7.6 Suggestions for Further Study.....	116
APPENDICES.....	119
A. EFFECT OF HOT GASES ON SHOCK WAVE AND CONVECTIVE FLOW VELOCITY IN A SHOCK TUBE.....	120
B. ORDER OF MAGNITUDE ANALYSIS ON GOVERNING EQUATIONS....	125
C. SERIES SOLUTION FOR A NON LINEAR ORDINARY DIFFER- ENTIAL EQUATION.....	132
REFERENCES.....	140

LIST OF TABLES

<u>Table</u>		<u>Page</u>
I	Wave Speeds for Diaphragm Materials.....	20
II	Particle Characteristics.....	34
III	Data Summary.....	44-45
IV	Wave Speed Probable Errors.....	51

LIST OF FIGURES

<u>Figure</u>		<u>Page</u>
1	Maximum Specific Impulse Loss versus Ratio of Particle Mass Fraction to Gas Mass Fraction.....	3
2	Summary of Experimental Data for Particles Accelerating in a Gas Stream as Obtained by Various Investigators.....	8
3	Coordinate Systems for Particle Dynamic Equations.....	13
4	Schematic Diagram of the Experimental Apparatus.....	17
5	Overall Experimental Set-up.....	19
6	Test Section Detail.....	21
7	Optical Bench.....	24
8	Detail of Particle Injection System.....	26
9	Circuit Diagram for Amplifier and Thyatron Unit.....	28
10	Circuit Diagram for Time Delay Unit.....	32
11	Samples of Particles Used in Experiment.....	35
12	Typical Example of Measurements to Determine Particle Acceleration.....	40
13	Sample Data Reduction Acceleration Curve.....	41
14	Drag Coefficient versus Reynolds Number - Non Burning Particles.....	46
15	Drag Coefficient versus Reynolds Number - Burning Particles.....	47
16	Velocity Distributions Corresponding to the Three Shear Distributions.....	64
17	Variation of Skin Friction over Sphere Surface.....	65
18	Drag Coefficient versus Reynolds Number for Three Assumptions of Shear Distribution.....	68

LIST OF FIGURES (CONT'D)

<u>Figure</u>		<u>Page</u>
19	Variation of Evaporation Rate on Surface of Liquid Sphere.....	73
20	Correction Factor for the Skin Friction Coefficient of an Evaporating Sphere.....	78
21	Schematic Diagram of Model for Burning Particle.....	82
22	Variation of "A" and "B" with Temperature.....	85
23	Skin Friction Distribution over Surface of Burning Sphere.	88
24	Variation of Separation Angle with Burning Rate for Reynolds Numbers Greater than 490.....	91
25	Separation Angle versus Reynolds Number.....	92
26	Theoretical Drag Coefficient versus Reynolds Number for a Burning Particle.....	93
27	Torobin and Gavvin's Drag Coefficients for Spheres as a Function of Relative Turbulent Intensity.....	102
28	Correlation between Torobin's Theory and Experiment for Effect of Turbulence on Critical Reynolds Number.....	105
29	X-T Diagram for Shock Tube with Hot Gas Section.....	122

NOMENCLATURE

A	Constant in Evaluation of Momentum Integral
<i>a</i>	Sphere Radius
a	Speed of Sound
<i>A</i>	Representative Area for Drag Coefficient
B	Constant in Evaluation of Displacement Integral
C	Constant in Evaluation of Density Integral
C_f	Skin Friction Coefficient $(\tau_s / \frac{1}{2} \rho_e U^2)$
C_D	Drag Coefficient $(F_D / \frac{1}{2} \rho_e U^2 A)$
C_p	Pressure Coefficient $(P - P_e) / \frac{1}{2} \rho_e U^2$
c_k	Mass Fraction of Species "k"
c_s	Velocity of Shock Wave
D	Diffusion Coefficient
d	Sphere Diameter
\vec{F}	Force Vector
f_c	Correction Factor for Drag Coefficient
f	Dimensionless Burning Rate $[\frac{(\rho u_r)_s}{\rho_e U}]$
g	Radial Distance Measured from Surface
h	Constant
g	Acceleration Due to Gravity
I_{sp}	Specific Impulse
K	Velocity Ratio Between Particle and Gas $(\frac{u_p}{u_g})$
Kn	Knudsen Number (λ/L)
k	Proportionality Factor for Burning Rate and Pressure
\bar{K}	Wave Speed Attenuation Factor

L	Characteristic Length
l	Constant
m	Mass
M	Mach Number (c_s/a)
\bar{M}	Molecular Weight
\vec{n}	Unit Outward Normal Vector
p	Pressure
p_v	Vapor Pressure
$Q(\theta)$	Functional Relationship for Evaporation Studies
q_0	Dynamic Pressure ($\frac{\rho_e U^2}{2}$)
\bar{Q}	Constant
Re	Reynolds Number ($\frac{\rho_e U d}{\mu_e}$)
Re _c	Critical Reynolds Number
r	Radial Coordinate, Burning Rate
S	Characteristic Surface Area
Sh	Sherwood Number [$\frac{\dot{m}}{\rho D S} (\frac{1}{c_e - c_s})$]
Sc	Schmidt Number ($\frac{\mu}{\rho D}$)
T	Temperature
Th	Thrust Per Unit Area
\bar{T}	Temperature Ratio Between Surface and Environment (T_s/T_e)
t	Time
t_c	Characteristic Time ($\frac{U}{\alpha}$)
\bar{t}	Nondimensional Time ($\frac{t}{t_c}$)
U	$ \vec{u} $
U _e	Relative Speed Tangential to Particle Surface

u_c	Convective Flow Velocity
\vec{u}	Relative Velocity Vector Between Particle and Medium
\vec{u}_k	Flow Velocity of Species "k"
u_p	Particle Velocity in Rocket Exhaust Exit
u_g	Gas Velocity in Rocket Exhaust Exit
\vec{v}	Velocity of Particle with Respect to Inertial Reference System
V	$ \vec{v} $
\dot{W}_k	Net Mass Rate of Production of Species "k" per Unit Volume
x_i	Spatial Coordinate
x_p	Mass Fraction of Particles in Rocket Exhaust
x_g	Mass Fraction of Gas in Rocket Exhaust
ξ	$\frac{9}{4} \frac{\sin^3 \theta}{C_f \sqrt{Re}}$
α	Particle Acceleration $(\frac{dV}{dt})$
β	$\frac{\xi}{\sin^2 \theta}$
γ	Dimensionless Vapor Concentration $(\frac{c-c_s}{c_e-c_s})$
δ	Boundary Layer Thickness
Δ	Probable Error Operator
ϵ	Perturbation Factor used in Evaporation Studies, Arbitrarily Small Number
η	Dimensionless Boundary Layer Velocity $(\frac{u_\theta}{U_e})$
Θ	Momentum Thickness
θ	Cone Angle in Spherical Coordinate System
θ_s	Separation Angle
λ	Mean Free Path
Λ	Constant in Evaporation Study
$\bar{\Lambda}$	Shape Factor

μ	Viscosity
ρ	Density
τ	Shear Stress
τ_{ij}	Stress Tensor Component
ϕ	Dummy Variable
χ	Dependent Variable in Acceleration Study
$\vec{\omega}$	Particle Rotational Vector

Subscripts

D	Diffusion
e	External Conditions
f	Contribution Due to Shear Forces
g	Gas Conditions
i	Vector Component
k	Species Component
p	Contribution Due to Pressure Forces
r	Radial Component
s	Surface Condition
v	Velocity
w	Wake Conditions
θ	Tangential Component

Superscripts

V	Viscosity
D	Diffusion

DRAG COEFFICIENTS OF INERT, BURNING, OR
EVAPORATING PARTICLES ACCELERATING IN GAS STREAMS

Clayton Thomas Crowe

ABSTRACT

A study was made to determine the effects of burning, evaporation, and acceleration on the drag coefficients of particles suspended and accelerating in gas streams. The problem was studied both analytically and experimentally in a Reynolds number range extending from 250 to 1600.

The effects of burning and acceleration were studied experimentally by subjecting burning particles (gunpowder) and non-burning particles to the convective flow behind a shock wave in a shock tube. The variation of the particle size and displacement with time were obtained by photographing the particle shadows with a high speed framing camera and concentrated light source. A conservative estimate of the contribution of the surface mass flux due to burning to the particle's inertial force indicated it was negligible compared to the pressure and viscous forces. Thus, the same equation for data reduction was used for both the burning and non-burning particles. The particle density, the speed of the shock wave, the atmospheric conditions, together with the photographic data provided sufficient information to calculate the particle's drag coefficient.

The model chosen for the analytical portion of the study was a spherical particle with mass flux through the surface to simulate burning and evaporation. An integrodifferential representation of the tangential equation of motion of a thin boundary layer on a sphere was used for the governing equation in the analysis. Assuming a velocity

distribution outside the boundary layer corresponding to incompressible inviscid flow, the governing equation was solved satisfying the appropriate boundary conditions. The solutions indicated that burning, evaporation, and acceleration will reduce the skin friction coefficient. The fractional reduction was found to be a function of; the mass fraction of vapor at the surface (c_s) and Schmidt number (Sc) for the evaporating particle, the ratio of mass flux from the particle surface to that in the free stream (\hat{r}) for the burning particle, and the accelerating modulus (Ac) for the accelerating particle. The form drag coefficient was estimated by assuming a relatively simple pressure distribution as suggested by other experimental results. The total drag coefficient was obtained by summing the skin friction and form drag coefficients.

The analytical expressions predicted and experimental results verified that the particle drag coefficient was insensitive to burning, evaporation, or acceleration effects if;

$$\frac{c_s}{Sc^{2/3}} < 0.1 \quad (Sc \geq 1), \quad Ac < 0.1, \quad \hat{r} < 0.025.$$

When the parameters satisfy the above stated conditions, other phenomena such as free stream turbulence, particle rotations, and particle roughness can cause larger variations in the drag coefficient than the mechanisms considered in this study.

An attempt was made to correlate the data of the present experiment with those of other investigators. A fair degree of success was achieved.

I. INTRODUCTION

1.1 Origination of Problem

The relatively large heats of formation of certain metal oxides and chlorides suggest the inclusion of such metals in solid propellant rocket fuels to improve their density and specific impulse characteristics. These metals are usually mixed into the propellant in the form of small particles which may vary from approximately 2 to 50 microns in diameter.

The improved characteristics of the fuel, however, are accompanied by a new problem. As the propellant burns these small particles will ignite upon or after breaking away from the deflagrating surface and may be carried out with the exhaust gases. Photographic studies of the particles' ignition phenomena have been presented by Wood⁽¹⁾. The large acceleration of the exhaust gases in the throat region creates appreciable velocity and temperature lags between the particles and the gas and is ultimately responsible for a loss in thrust.

A crude estimate as to the effect of suspended particles in rocket exhausts can be achieved in the following way. Denote the velocities of the particles and gas at the exit of an ideally expanded nozzle as u_p and u_g respectively. Assume the mass fractions of the two phases are x_p and x_g . The thrust per unit area is equal to the momentum flux per unit area, or

$$Th = \rho x_p u_p^2 + \rho x_g u_g^2 \quad (1.1)$$

From this expression the specific impulse can be written

$$I_{sp} = \frac{x_p u_p^2 + x_g u_g^2}{g(x_p u_p + x_g u_g)} \quad (1.2)$$

Introducing the term "K" defined as

$$K = \frac{u_p}{u_g} \quad (1.3)$$

and utilizing the following expression for particle-free flow

$$I_{sp_{x_p=0}} = \frac{u_g}{g} \quad (1.4)$$

one obtains

$$\frac{\Delta I_{sp}}{I_{sp_{x_p=0}}} = - \frac{x_p}{x_g} \frac{K(1-K)}{1 + \frac{x_p}{x_g} K} \quad (1.5)$$

The above analysis neglects gas-particle thermal lag and the effect of the particles on the gas exit velocity.

Equation (1.5) indicates that for a given value of x_p/x_g there will be a corresponding value of K for which the specific impulse loss is a maximum. Taking the derivative of Equation (1.5) with respect to K and equating it to zero one finds

$$K_c = \frac{x_g}{x_p} \left[\left(1 + \frac{x_p}{x_g}\right)^{1/2} - 1 \right]$$

where K_c is the value of K when $\Delta I_{sp}/I_{sp_{x_p=0}}$ is a maximum. Figure 1 illustrates the maximum loss in I_{sp} for x_p/x_g ranging from zero to 1.6 along with the corresponding values of K_c .

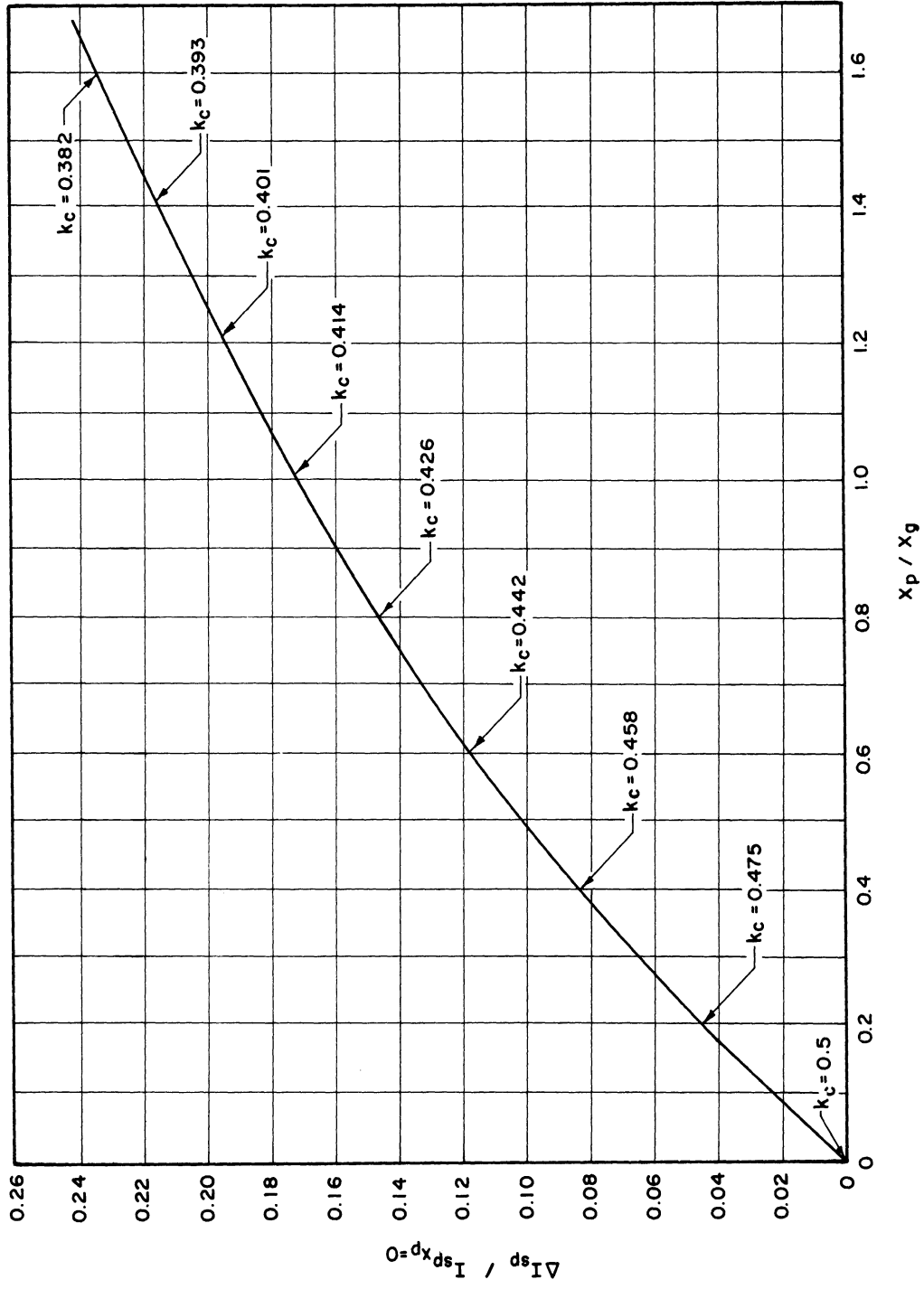


Figure 1. Maximum Specific Impulse Loss versus Ratio of Particle Mass Fraction to Gas Mass Fraction.

The evaluation of K depends on many factors, namely; particle density, mass, and drag coefficient as well as the variation of density and velocity through the rocket nozzle. The importance of drag coefficient can be assessed immediately by noting that $K = 1$ for $C_D = \infty$ and $K \approx 0$ for $C_D = 0$ (provided U_p is small initially). Thus very small or very large particle drag coefficients will improve nozzle performance.

1.2 Review of Studies Concerned with Problem

One of the earliest works on the effects of particles in rocket nozzles was presented by Maxwell et al.⁽²⁾ in 1946. In particular, they investigated the effect of smoke on the rocket performance. They assumed the particles were 0.5 microns in diameter and that Stokes's drag coefficient was valid. Assuming constant acceleration of gases through the nozzle with a velocity gradient of 6500 sec^{-1} they were able to show the velocity lag was negligible. Consequently, from Equation (1.5), the specific impulse would be essentially unaffected.

Considering larger particles, Gilbert et al.⁽³⁾ did a similar analysis in 1955. They chose to use the steady state drag coefficient for a sphere. This was accomplished by using the same equations as Maxwell et al. and correcting the Stokes's drag coefficient by a factor " f_c " to give the desired drag coefficient, or

$$f_c = \frac{C_D (\text{sphere in steady flow}) Re}{24}$$

Utilizing a 1300 sec^{-1} velocity gradient through a typical 1300-lb-thrust rocket nozzle, it was found that a 10 micron particle would produce a 1%

loss in specific impulse while a 100 micron particle would result in a 3% loss. The mass ratio of particles (x_p) was assumed to be 20%. Both this analysis and the previous one neglected the effect of the particles on the gas exit velocity.

The effect of the particles on the velocity of the surrounding medium was included in an analysis by Carrier⁽⁴⁾ in which he derived the equations for the trajectories of dust passing through a normal shock wave. Assuming the following relationship for drag coefficient, Nusselt number, and Reynolds number,

$$C_D = \frac{Nu}{Re}$$

he was able to represent the momentum and energy balance by the same equation. He then proceeded to use this equation to find relationships between the significant parameters of the problem.

Following this work Kliegel⁽⁵⁾ employed essentially the same assumption for the drag coefficient relationship and applied the equations to the study of a one dimensional rocket nozzle. He restricted his analysis to constant thermal and velocity lags and presented a qualitative discussion of lag effects. In a later paper⁽⁶⁾ he applied the equations to an axisymmetric nozzle and modified the Stokes's drag law by a factor " f_c " to give a more representative drag coefficient.

Kliegel's equations for one dimensional flow have been numerically integrated by Bailey et al.⁽⁷⁾. They used the " f_c " factor for modifying the Stokes's drag coefficient to give the steady state value for a sphere. The calculations were concerned with a typical truncated

nozzle of radius ratio 2 (radius ratio = contour radius of curvature/ throat radius). Assuming particle sizes from 2 to 5 microns they found thrust losses of more than 5% could be encountered with a particle mass ratio of 40%.

Stonecypher⁽⁸⁾ has recently performed analyses in which he considered the velocity variations of nozzles of different geometries and assumed the particle's drag coefficient was that of a sphere in steady flow corrected by Cunningham's factor for rarefied gas effects. This one dimensional analysis neglected the particles' influence on the exhaust gases but did account for the gas-particle thermal lag.

In addition to the analytical work, some experiments have been performed to evaluate the efficiency loss due to the presence of particles. One such study has been reported by Brown⁽⁹⁾. Testing rocket nozzles of different geometries he found experimental values for $\Delta I_{sp}/I_{sp_{x_p=0}}$ ranging from 5% to 9%. Although part of these inefficiencies may have been due to heat transfer, he concluded the major portion was due to particle lag.

1.3 Purpose of this Study

In the analyses described above one of the major assumptions was the choice of a representative drag coefficient for the particles. Some analyses used Stokes's drag coefficient, or a modified version of same, while other analyses used the steady state drag coefficient for a sphere. The purpose of this study is the attainment of analytical and experimental values of drag coefficients which are valid for a burning particle in an accelerating flow field.

1.4 Experimental and Analytical Work Pertaining to Particle Drag Coefficients

Some experimental work has been done to determine the drag coefficients of accelerating, burning, and evaporating liquid drops as well as accelerating solid particles. The results of these experiments appear in Figure 2.

Ingebo⁽¹⁰⁾ has done a considerable amount of experimental work to determine the drag coefficients of evaporating liquid fuel drops and solid particles. He injected small spheres and droplets with negligible entrance velocity into a stream moving from 140 to 180 feet per second. By use of a specially designed camera he was able to determine the size and velocity of the particles at different distances from the injection point. Correlating this data gave the velocity variation with distance for certain size particles from which the particles' accelerations were obtained. He found the drag coefficients for solid particles as well as droplets fell on a single curve best represented by

$$C_D = \frac{27}{Re} 0.84$$

Ingebo accredited the difference between his results and those for a sphere in steady flow to acceleration and rotational effects.

Fledderman and Hanson⁽¹¹⁾ performed a similar investigation by photographing spray droplets entrained and accelerating in streams

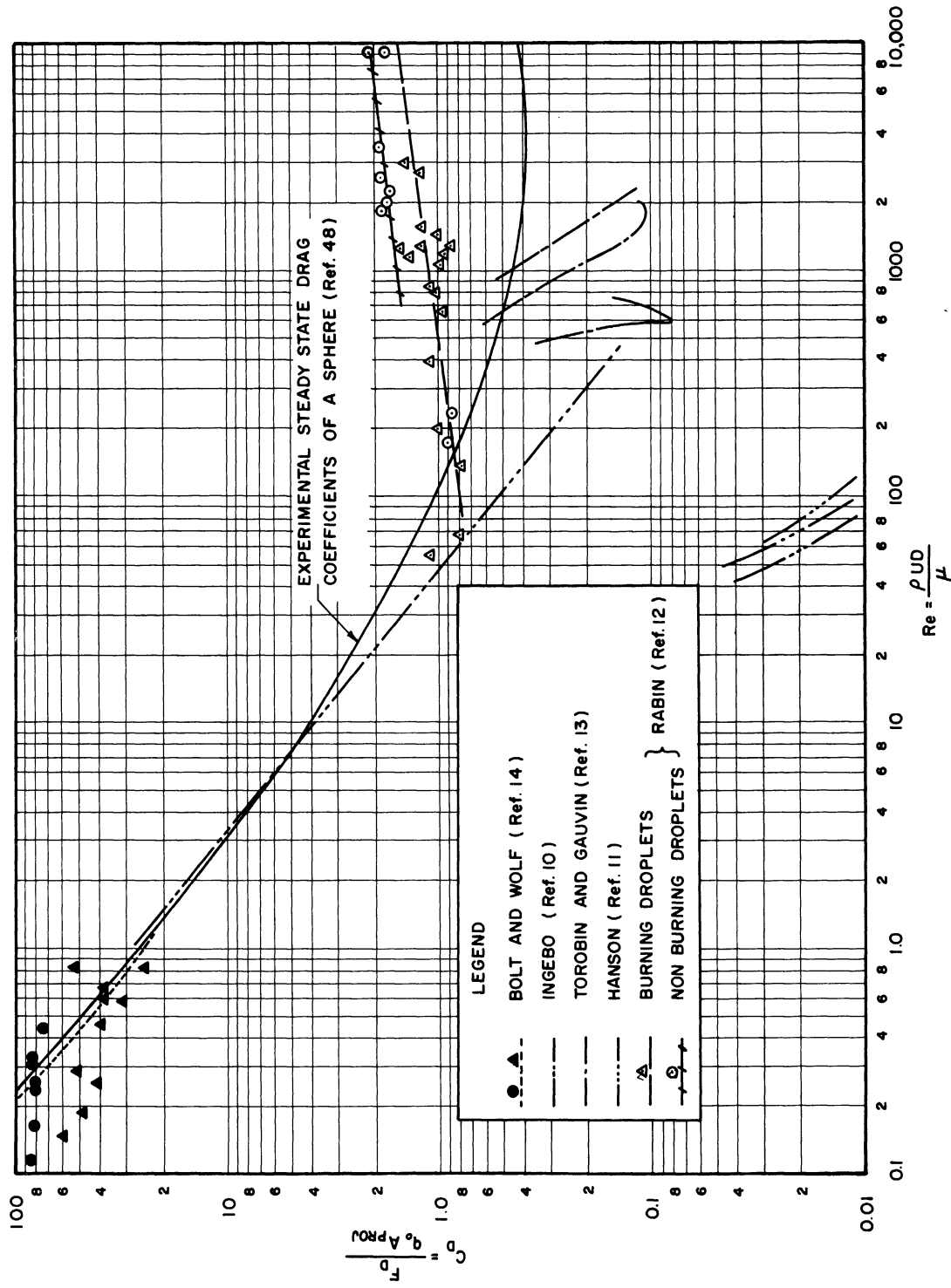


Figure 2. Summary of Experimental Data for Particles Accelerating in a Gas Stream as Obtained by Various Investigators.

moving from 50 to 75 feet per second. The resulting Reynolds number ranged from 20 to 100. Their results indicated a definite dependence on velocity and were the order of one hundredth the steady state value for a sphere.

Recently, Rabin et al. ⁽¹²⁾ determined the drag coefficients of burning and nonburning liquid fuel droplets subjected to the convective flow behind a shock wave. For Reynolds numbers in excess of 200 the drag coefficients were greater than those for a sphere in steady flow. Below Reynolds numbers of 100 the two points obtained appear to correspond with Ingebo's results. It was also interesting to note that the nonburning particles appeared to have larger drag coefficients for Reynolds numbers in excess of 1000.

The effect of turbulence on the particle drag coefficient was the subject of a most interesting study by Torobin and Gauvin. ⁽¹³⁾ They fired small radio-active spheres into a tube of known turbulence intensity and recorded the particles' motion with radio-active sensing devices. They found an increase in turbulence intensity could shift the critical Reynolds number down to the order of 1000.

Experimental drag coefficients for burning kerosene drops have been reported by Bolt and Wolf. ⁽¹⁴⁾ The results lie in the $Re < 1$ regime and indicate a decrease in drag coefficient over the nonburning particles of corresponding Reynolds numbers.

Experiments have been reported in which the effect of acceleration on the drag coefficient of spheres was studied. ^(15,16) However, it is felt that the results are not applicable to the present problem since the spheres were accelerated into a stagnant fluid and

the acceleration and relative velocity vectors were of opposite sense. The present study is concerned with problems in which these vectors have the same sense.

Very little analytical work has been done to study the effects of acceleration, burning, or evaporation on drag coefficients. Particle acceleration at very low Reynolds numbers ($Re < 1$) has been treated theoretically by Basset⁽¹⁷⁾ and more recently by Pearcey and Hill.⁽¹⁸⁾ Basset extended Stokes's equation to include the unsteady term while Pearcey and Hill concerned themselves with Oseen's equation. Both analyses indicate the effect of acceleration is small for small spheres in air and the effect will decrease with decreasing fluid densities. For the larger Reynolds numbers, there appears to be no analytical treatment concerning either acceleration or burning effects on drag coefficients for spheres.

1.5 Reynolds Number Range of Interest

In order to determine the Reynolds number range of interest for the particle problem, a calculation was performed using Stonecypher's results.⁽⁸⁾ A 7 micron particle in a nozzle formed by the mating of a truncated 45° convergent cone and a 15° divergent cone experiences a 2500 feet per second velocity lag at the throat. Using other flow characteristics corresponding to the throat conditions gives a Reynolds number of 266 for the particle. Larger particles would have larger Reynolds numbers due to greater velocity lags and particle diameters. Consequently it appears reasonable that the range of interest should extend from Stokes's flow to Reynolds numbers of the order of 1000.

The small diameter of the particles encountered in the exhaust gases suggest that rarefied flow effects may be significant. Using the same conditions as above and defining a Knudsen number based on the boundary layer thickness, as suggested by Schaaf⁽¹⁹⁾, one finds:

$$\text{Kn} \approx 1.6 \times 10^{-2}$$

The boundary layer thickness used to determine the Knudsen number was that which would exist at the stagnation point. Thus, the particles' flow characteristics appear to exist between the continuum and slip flow region.⁽²⁰⁾ For the theoretical analysis, however, continuum flow will be assumed.

II. EQUATION OF MOTION FOR A PARTICLE WITH MASS FLUX THROUGH THE SURFACE

Newton's second law of motion states that the inertial force acting on an arbitrary control volume is equal to its net rate of change of momentum with respect to an inertial frame of reference. In addition, the third law states that the inertial force must be equal and opposite to the applied force.

Consider a particle of mass "m" and of arbitrary shape and imagine a control surface to be located on the particle surface thus making the particle itself the control volume. Locate a coordinate system at the center of mass of the particle and allow it to move with a velocity \vec{v} with respect to inertial space. It will be assumed that this vector, \vec{v} , does not rotate with respect to inertial space. Denote \vec{u} as the velocity of the surrounding medium with respect to the particle's coordinate system or, in other words, relative to the particle itself. Allow the particle coordinate system to rotate about its origin with the rotational vector $\vec{\omega}$. Figure 3 illustrates the coordinate systems.

The net rate of change of momentum is equal to the sum of the momentum change per unit time within the control volume and the net momentum flux through the control surface. Expressing the statement using mathematical symbols one has

$$\vec{F}_I = \frac{d}{dt} \int_V \rho (\vec{v} + \vec{\omega} \times \vec{r}) dV + \int_S \rho \vec{u} \cdot \vec{n} (\vec{v} + \vec{u}) dA \quad (2.1)$$

where \vec{F}_I = inertial force vector

\vec{n} = unit outward normal vector from control surface

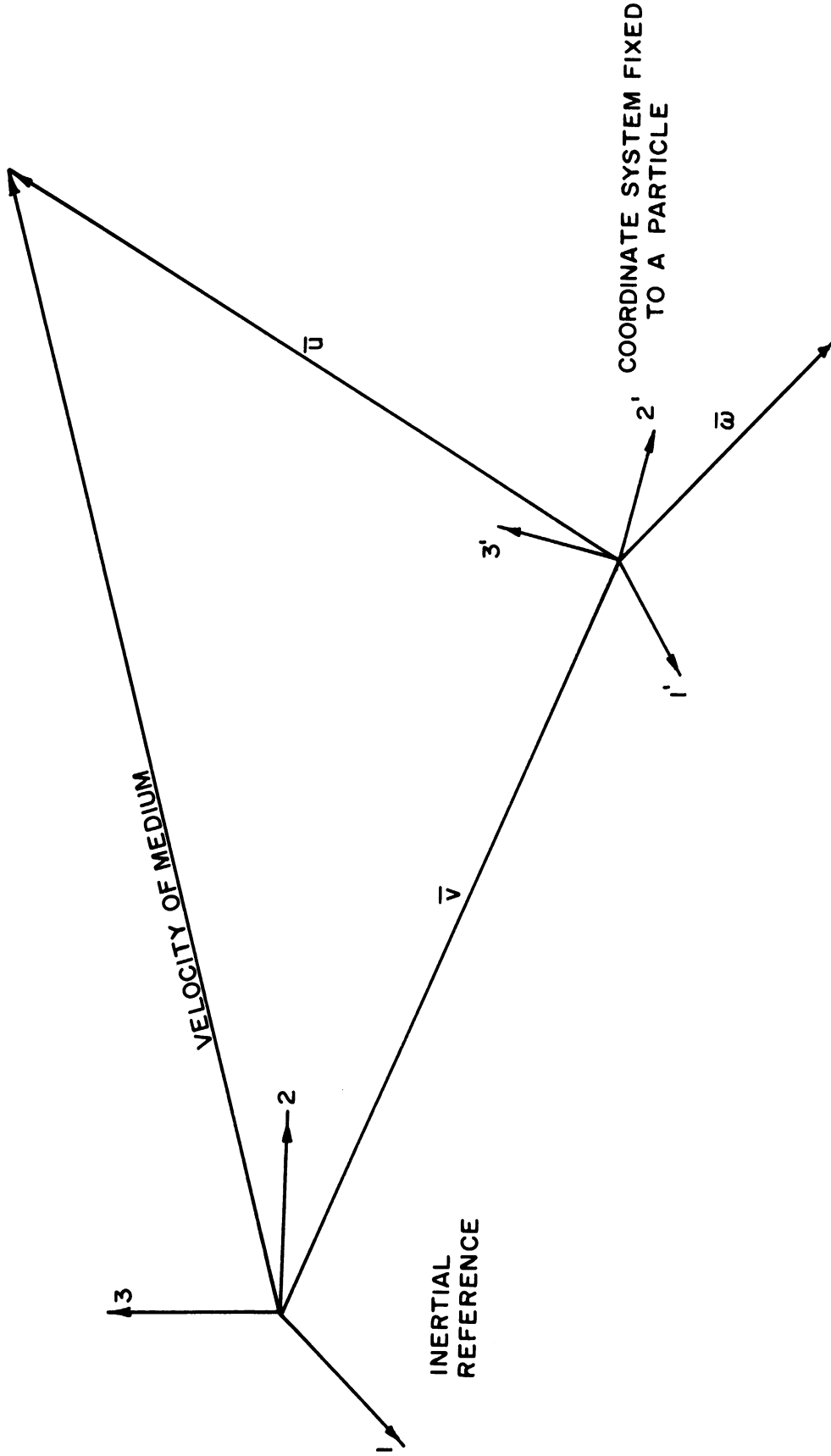


Figure 3. Coordinate Systems for Particle Dynamic Equations

V = control volume

S = control surface

A = area

ρ = density

t = time

$\int_V dV$ = integration over control volume

$\int_S dA$ = integration over control surface

\vec{r} = radius vector of a point with respect to particle coordinate system.

In writing the above equation, it is assumed that the particle is a rigid mass.

Rewriting Equation (2.1), one obtains

$$\begin{aligned} \vec{F}_I = & \frac{\partial}{\partial t}(m\vec{U}) + \frac{\partial}{\partial t}\vec{\omega} \times \int_V \rho \vec{r} dV + \vec{U} \int_S (\rho \vec{u} \cdot \vec{n}) dA \\ & + \int_S (\rho \vec{u} \cdot \vec{n}) \vec{u} dA \end{aligned} \quad (2.2)$$

However, by using the definition of center of mass

$$\int_V \rho \vec{r} dV = 0 \quad (2.3)$$

and continuity equation

$$\int_S \rho \vec{u} \cdot \vec{n} dA = - \frac{\partial m}{\partial t} \quad (2.4)$$

Equation (2.2) becomes

$$\vec{F}_I = m \frac{\partial \vec{U}}{\partial t} + \int_S (\rho \vec{u} \cdot \vec{n} dA) \vec{u}$$

The applied forces are the pressure and viscous forces which act on the control surface and the body forces which act on the control volume. If the pressure and viscous forces are expressed in terms of a drag coefficient, the equation expressing the balance of forces on a

particle may be written as

$$C_D \frac{\rho}{2} |\vec{u}| \vec{u} \mathcal{A} + m \vec{f} = m \vec{a} + \int_s (\rho \vec{u} \cdot \vec{n} dA) \vec{u} \quad (2.5)$$

where \vec{f} = body force per unit mass

\vec{a} = acceleration of particle with respect to an inertial coordinate system,

\mathcal{A} = representative particle area.

For a particle in continuum flow, the tangential component of velocity at the surface is zero so the velocity at the surface, with respect to the particle coordinate system, is the normal velocity. Thus, Equation (2.5) has the form

$$C_D \frac{\rho}{2} |\vec{u}| \vec{u} \mathcal{A} + m \vec{f} = m \vec{a} + \int_s (\rho u^2) \vec{n} dA \quad (2.6)$$

It is interesting to note at this point that if ρu^2 is a constant over the surface, then

$$\int_s (\rho u^2) \vec{n} dA = \rho u^2 \int_s \vec{n} dA \equiv 0 \quad (2.7)$$

and the mass flux from the surface does not contribute to the inertial forces. Thus, it is evident that the contribution to inertial forces by the rate of change of particle mass can only be computed when the variation of ρu^2 is known over the surface.

Equation (2.6) will be considered again below in the discussion concerned with the reduction of experimental data.

III. EXPERIMENTAL ARRANGEMENT AND PROCEDURE

3.1 Choice of Experimental Facility

The crude analysis performed in the introduction indicated that the Reynolds number range of interest for the rocket exhaust particle problem lied between the Stokes's flow regime and Reynolds numbers of 1000. Thus, the experimental facility should be capable of providing drag coefficient and burning rate data for reacting particles in this flow regime. The present study, however, will limit itself to Reynolds numbers larger than two hundred while an ensuing study^{*} will attempt to include the smaller Reynolds number range.

For the present study various experimental set-ups were considered, such as; introducing particles upstream of a stationary normal shock or standing detonation wave and recording their motion upon passage through the wave, passing particles through an oblique shock wave, accelerating particles by magnetic fields and, lastly, subjecting particles to the convective flow behind a shock wave in a shock tube. The last scheme was selected because of its relative simplicity and adaptability to the equipment at hand. In addition, this type of facility had been used successfully by Rabin⁽¹²⁾ to study the shattering of liquid drops.

3.2 Description and Design of Experimental Set-Up

The schematic sketch in Figure 4 illustrates the fundamental idea behind the experimental set-up. Particles were injected into a vertical shock tube above the test section and fell toward the testing region. A flame in the test section ignited the particles. Then a

* Current project at Aircraft Propulsion Laboratory, The University of Michigan, sponsored by NASA.

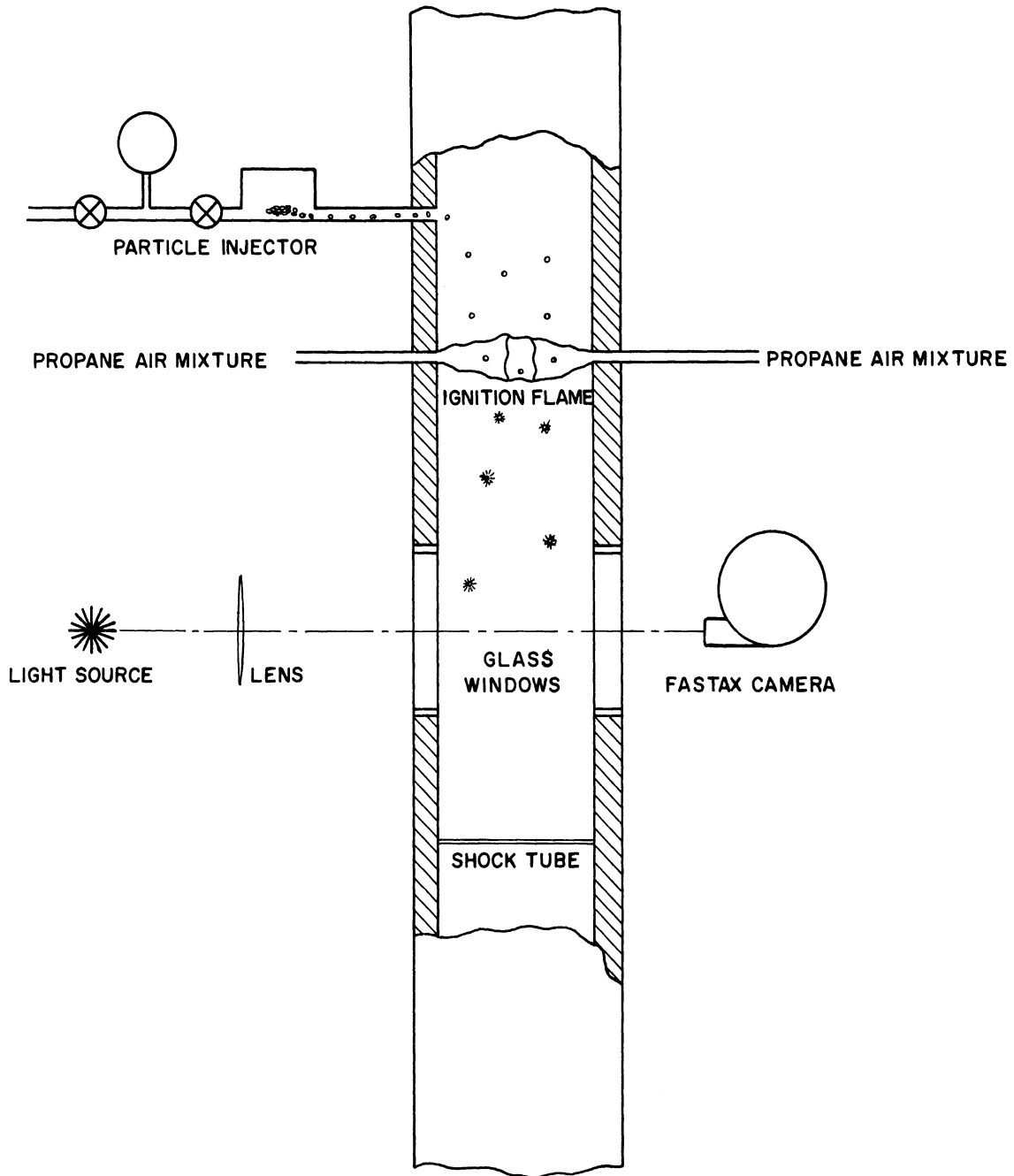


Figure 4. Schematic Diagram of the Experimental Apparatus.

shock wave, coming from below, subjected them to a convective flow field accelerating them upwards. A high speed framing camera coupled with a light source took moving pictures of the particles from which particle acceleration and burning rate data could be obtained. The occurrence of the shock wave had to be so timed that it met the particles shortly after they came into the field of view. This insured the largest particle acceleration and smallest velocity; a condition most attractive to the photographic tracking technique.

Figure 5 is a photograph of the experimental equipment.

3.2.1 Shock Tube and Driver Section

The shock tube, fabricated from cold rolled steel bars, had an inside $1/2''$ x $3/8''$ rectangular cross section and an eleven foot length. The test section was located in the center and the driver section was attached at the bottom. The top of the shock tube extended through a piece of fiberglass to prevent particles which escaped through the top from falling down on the experimental equipment.

The driver section had the same inside dimensions as the shock tube and was one foot in length. It was separated from the shock tube by a sliding bar mechanism which facilitated the installation of diaphragm material. The other end of the driver section was connected by means of a $1/4''$ tube and aircraft-type solenoid valve to a nitrogen bottle. The pressure out of the nitrogen bottle was controlled by a Airco regulator valve. The diaphragm was ruptured by setting the regulator valve to a sufficiently high pressure and opening the solenoid valve which pressurized the driver section. For a particular diaphragm

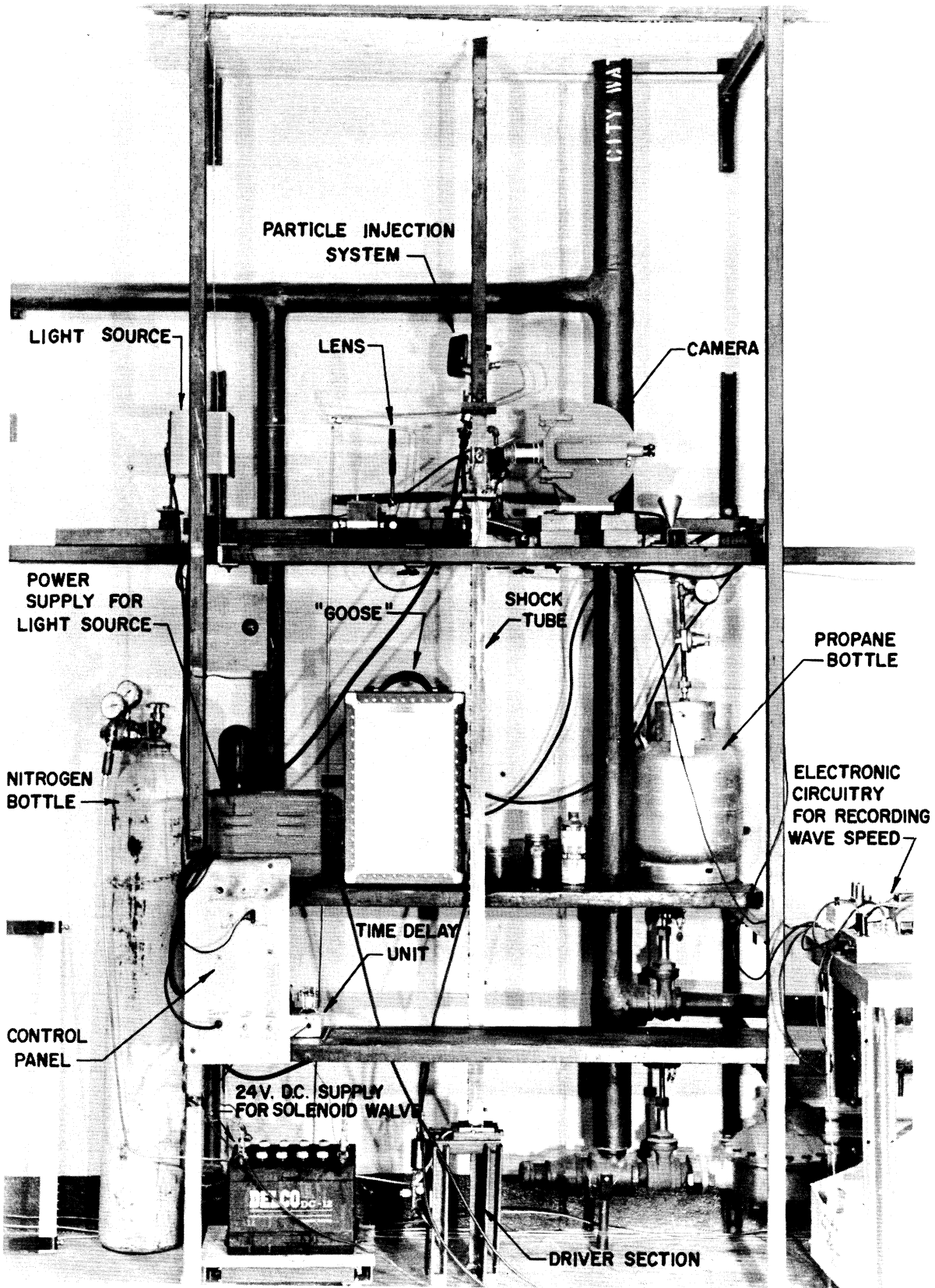


Figure 5. Overall Experimental Set-Up.

material the wave speed appeared to be independent of the pressure setting on the regulator so long as it was sufficient to break the diaphragm.

In this particular study, three diaphragm materials were used, namely; tissue paper, rough scratch paper and bond paper. Each gave an increasingly larger wave speed in the above mentioned order. The range of wave speeds attained with these diaphragm materials is shown in the following table:

TABLE I

WAVE SPEEDS FOR DIAPHRAGM MATERIALS

<u>Diaphragm Material</u>	<u>Wave Speed (ft./sec.)</u>
Tissue paper	1220-1260
Scratch paper	1286-1341
Bond paper	1459

Because of the relatively weak waves used in the present experiments and the length of the shock tube the run time was dictated by the length of the driver section. That is, the test was over when the downward progressing expansion wave, initiated by the diaphragm rupture, had reflected from the end of the driver section and reached the test section. The run time was of the order of 2 milliseconds.

3.2.2 Test Section

The test section, shown in detail in Figure 6, was a separate component 8 1/2" in length.

The windows consisted of 1/2" thick pyrex glass. The window nearest the camera was etched on the inside surface to provide a reference

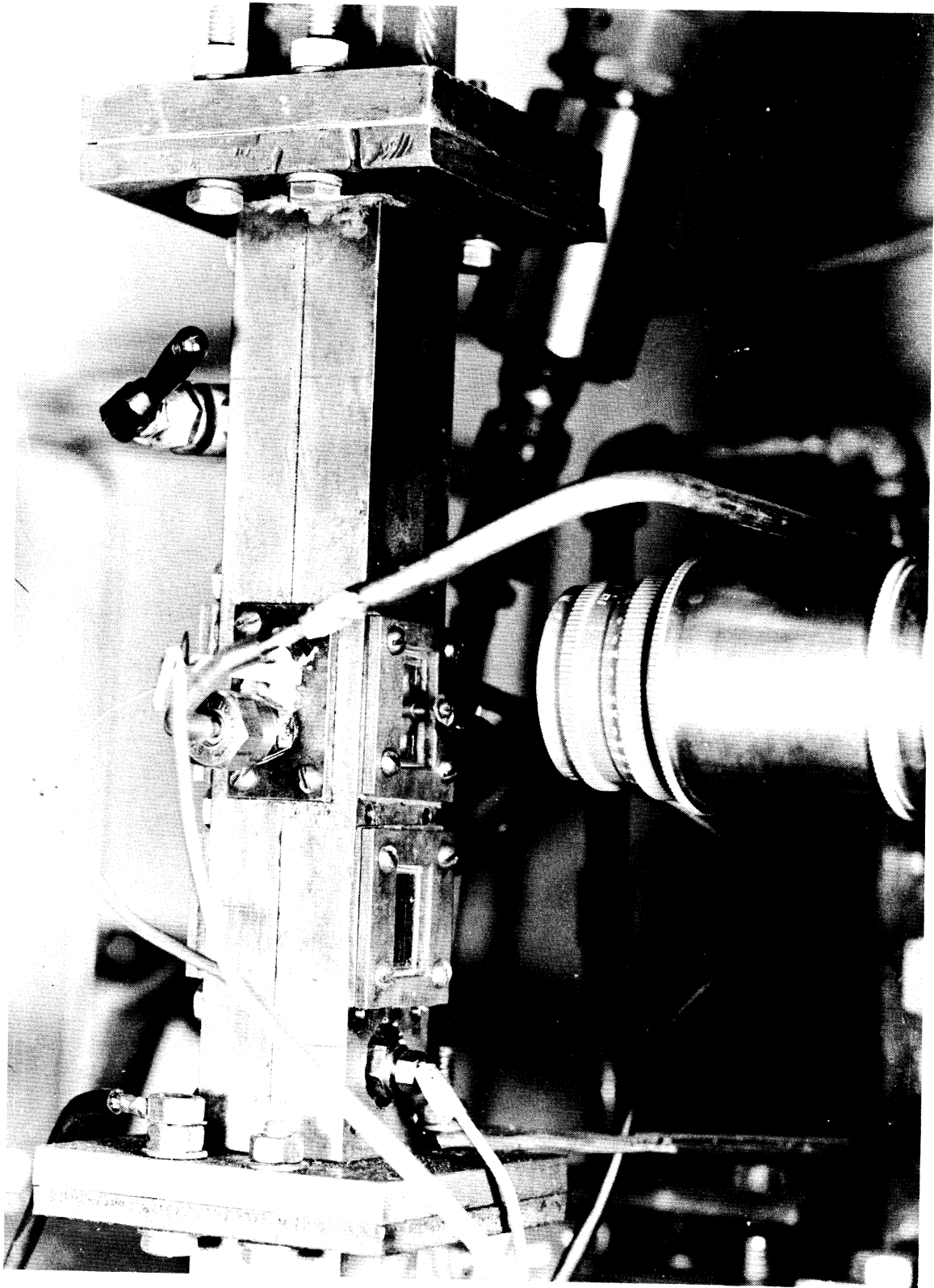


Figure 6 Test Section Detail.

line on the photographs. The windows could easily be removed by removing the cover plates and gaskets. This operation was often necessary to clean the glass and replace windows cracked by the hot flame in the test section.

The particles were ignited by a propane-air flame fed by two opposing jets installed in the two removable sections of tunnel wall. The propane and air supplies were regulated by two needle valves situated upstream of a mixing chamber. The mixed gases from the chamber were fed to the jets inside the tunnel by $1/4$ " stainless steel tube. The stabilization of the flame was assisted by a small hot wire mounted in the tunnel wall and heated by a 6 volt battery.

The electrical connection, which can be seen emerging from the center of a viewing window, was a high voltage electrode which furnished a spark between itself and the inside tunnel wall for ignition of the propane-air flame. It consisted of an $1/8$ " diameter copper rod glued, to prevent leaks, to a hole in the viewing window. One end was flush with the inside glass surface while the other end was drilled and tapped to facilitate an electrical connection. The high voltage to this copper rod was supplied by an old Ford coil and six volt battery.

The small toggle valve located above the test section was employed to relieve the initial pressure pulses created by attempting to ignite a flammable mixture inside a tube. Once the flame had been ignited the valve was slowly closed and the mass flow through the jets would slowly adjust itself to the larger downstream pressure without extinguishing the flame.

Below the bottom window in Figure 6 an SIM pressure transducer can be seen which was used, in conjunction with another one just below, to measure the speed of the shock wave.

3.2.3 Optical Bench

A shadowgraph technique was used to photograph the particles and the system used is shown in Figure 7.

A 100 watt Sylvania zincronium arc lamp, located in the tin box on the left, supplied a sufficiently intense light to photograph particle shadows at high framing rates. The lens between the lamp and shock tube served to focus the light on the test section. The arc lamp had its own especially adapted power supply.

The camera, pictured on the right, was a 16 mm Wollensak Fastax camera fitted with extension tubes to provide a magnification of 1.174. The camera speed was controlled by a Woolensak "Goose" which regulated the voltage applied to the camera. It was possible, using the "Goose", to obtain framing rates of approximately 7300 frames per second over the last 30 or 40 feet of film. The film used in this experiment was Dupont Reversible 931A sprocketed for Fastax cameras. The framing rate was calculated by observing timing marks on the edge of the film made by a neon light which flashed 120 times a second.

The lens magnification was calculated using the lens focal length and distance between the film and test section center. This method was also checked by computing the magnification of the shadowgraph picture of a small hole in a piece of metal positioned in the test section.

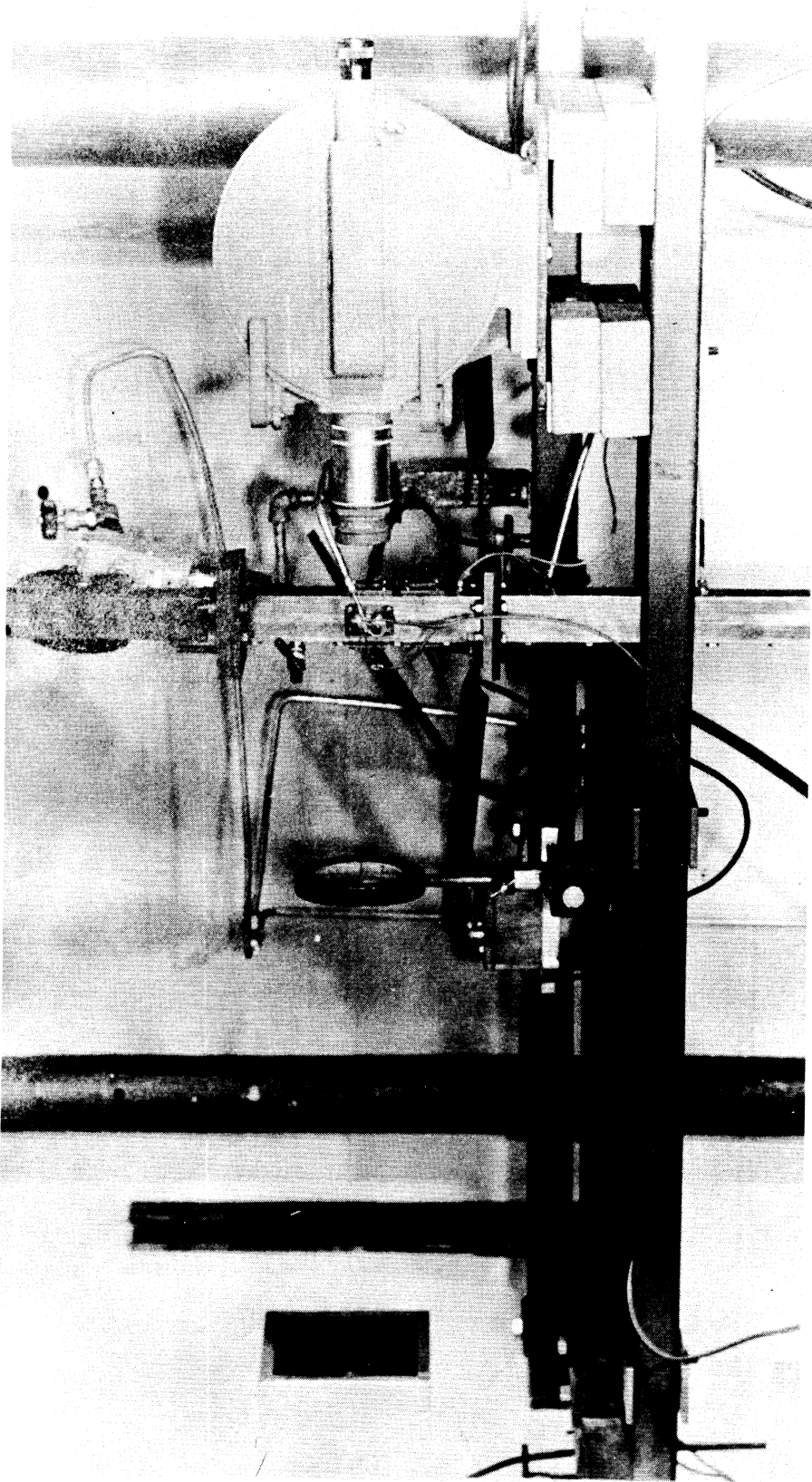


Figure 7. Optical Bench.

3.2.4 Particle Injection System

Figure 8 illustrates the particle injection arrangement.

The purpose of the particle injection system was to blow the particles into the tube by a gust of air. First, the particles were fed by means of a funnel into the top hole in the square metal part next to the tube and sealed by an 1/8" pipe plug. A valve, hidden by the pressure gauge in Figure 8, was then opened to pressurize the section above the solenoid valve to about 5 psig. Energizing the solenoid valve then blew the particles into the tube. The needle valve located between the solenoid valve and particle holder was used to control the duration of the gusts. The solenoid valve was of an aircraft variety which required 24 volts D.C. to operate.

3.2.5 Wave Speed Recording System

As mentioned above SLM pressure transducers were used to measure the wave speed. These transducers along with a signal amplifier, thyatron switching circuit and Berkely interval timer(model 5120) indicated the time for passage of the wave between the two transducers and consequently the wave speed.

The principle of operation was conventional. The charge created by the pressure transducer was converted to a voltage signal (by the grid-cathode capacitance of a 6AU6), amplified and fed to the grid of a thyatron. This signal was sufficient to trip the thyatron into conduction and the voltage increase across a resistor in the thyatron circuit supplied a voltage pulse to the Berkely timer. The lower transducer then started the timer and the upper transducer supplied a stop pulse.

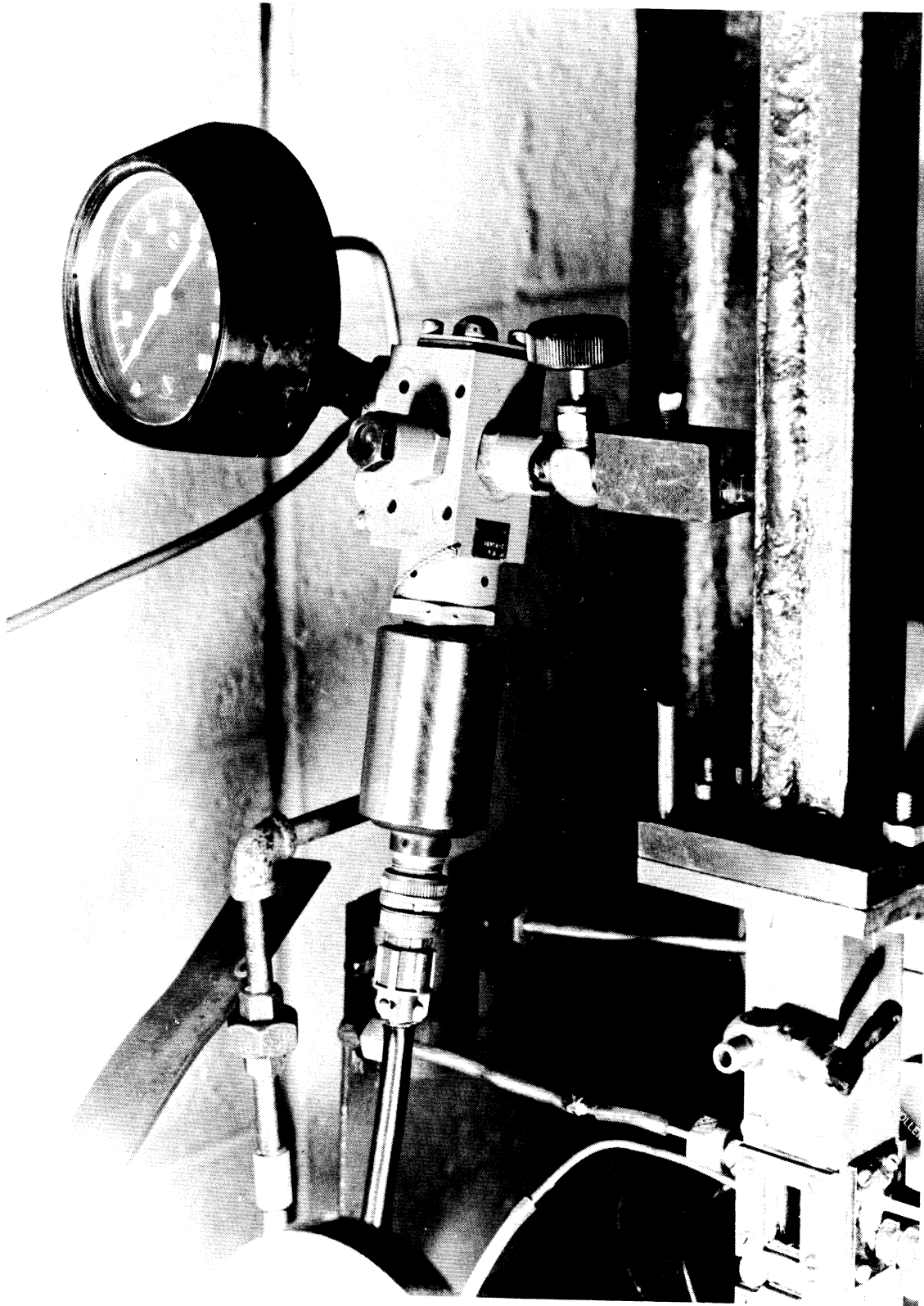


Figure 8 Detail of Particle Injection System.

Figure 9 illustrates the circuit diagram for one channel of the amplifier and thyatron circuit.

The major limitation of the experimental set-up was the difficulty in recording the speeds of the weaker shock waves. The weaker signals necessitated a more critical thyatron grid bias setting and, in turn, stray signals from the relays, solenoids, and other equipment were sufficient to trip the tube into conduction. For further studies a more sensitive pressure transducer will be required. However, the system employed above sufficed for the present experiment.

Each thyatron channel had its own power supply. This was found to increase the sensitivity of the thyatron circuit for the following reason; when the start circuit fired, the plate voltage would drop about five volts and would increase the bias necessary to fire the second thyatron by about a volt. This difficulty was eliminated and the sensitivity increased by using separate power supplies for the thyatron plate circuits.

In order to determine the difference in time lag between the two circuits a series of runs were performed and compared with the results obtained by interchanging the stop and start channels including the transducers. There was a time difference of 5 microseconds. The circuit was then set up to give the largest time interval and a tare reading of 2.5 μ 's was subtracted from all the readings to follow.

The choice of a satisfactory location for the pressure transducers required the consideration of two problems; shock wave attenuation and the effect of a flame in the test section. The small

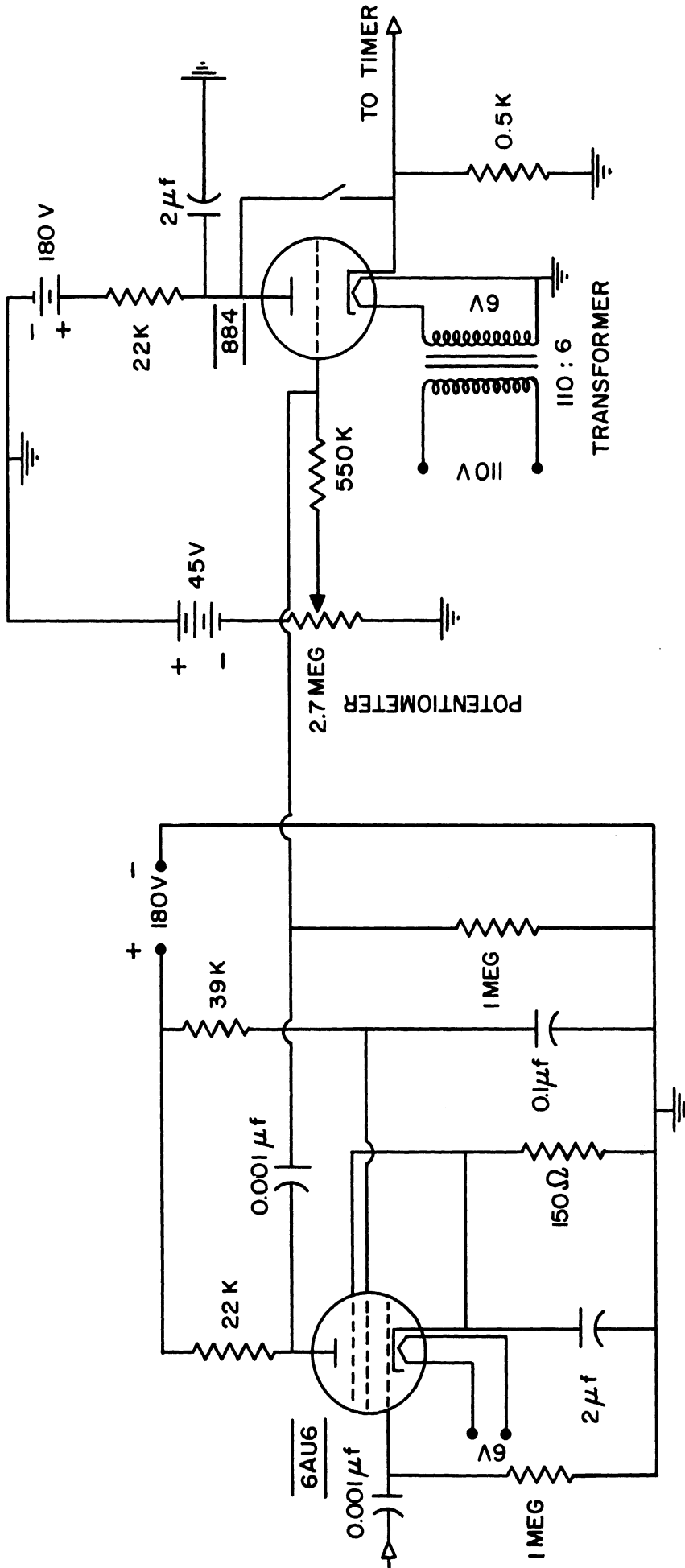


Figure 9. Circuit Diagram for Amplifier and Thyatron Units.

cross-sectional area of the tube aggravated the attenuation problem as wave speeds decreased as much as four percent over a four foot length. Ideally the best location for the transducers would have been across the test section had not a flame existed in this region. The effect of the hot gases produced by the flame was to increase the wave speed and convective flow velocity.

In order to estimate the magnitude of the hot gas effect it was necessary to estimate the temperature above the test section. This was done as a separate test by removing the toggle valve and inserting a loosely fitting thermocouple. The fact that the thermocouple did not fit tightly in the hole left by removal of the toggle valve caused considerable leakage of the gases from the test section when the mixture was ignited. A temperature of 500°F was measured. However, this value was probably high since, in the actual case, the pressures in the test section would be larger, the mass flows less, and consequently less energy release per unit time for heating of the gases.

Nevertheless a temperature of 500°F was used in Appendix A to determine the effect of the hot gases. The simplified analysis presented therein indicated the wave speed increased by as much as 40% while the convective flow velocity was augmented by 15%. The particle's velocity being much less than the flow velocity, the particle experienced a change in free stream velocity of only a fraction of this value. However, the inertial effect of the cooler gases together with a high assumption for gas temperature make a number like 3 or 4 a most logical choice for the change in the particle's free stream velocity.

If the wave speed had been measured across the test section it would have been most difficult to interpret the time interval reading since the wave speed varies so in this region. Consequently it was decided to measure the wave speed as close to the test section as possible but below it to avoid the hot gases. One pressure transducer was placed 3" below the test section while the other one was placed 8" below the first. A series of runs were then performed to determine the extent of attenuation between the test section and where the wave speed was measured. These data were then used to correct the readings for attenuation in the experiments to follow.

Readings on the interval timer ranged from 462 to 533 microseconds.

3.2.6 Sequence Timing System

The correct timing of operations in the experiment was most crucial. The timing sequence centered around having the shock wave encounter the particles at the test section as the camera approached its highest framing rate. The slowest operation was bringing the camera up to speed which required about $3/4$ of a second. Shortly after the camera had been started, the solenoid valve on the particle injection system would open injecting the particles into the tube. Almost immediately the solenoid valve between the nitrogen bottle and driver section would open bursting the diaphragm and sending a shock wave up the tube. Thus, two time delay units were necessary. One of the time delay units was an integral part of the "Goose" and timed the activation of the particle injection system. Another time delay unit, capable of time delays up

to $3/4$ second, was built to time the bursting of the diaphragm and its circuit diagram is shown in Figure 10. All time delays were initiated by a single start switch.

3.3 Experimental Procedure

Prior to performing an experiment it was necessary to check the thyatron bias setting, camera focus, and cleanliness of the pyrex glass windows and to make sure all the electronic circuitry was performing normally.

The normal experimental procedure was as follows:

- 1) load camera
- 2) install diaphragm
- 3) load injector and pressurize
- 4) ignite mixture*
- 5) activate light source
- 6) set thyratrons and zero timer
- 7) engage start switch .

While running the experiment the test section was closely observed to verify the ignition of the particles.

After each run the atmospheric temperature and pressure were recorded as well as the time interval reading on the Berkely timer. The film was also removed from the camera and marked.

One important feature of the experimental procedure was the amount of particles to be loaded in the injector. Too many particles caused the particle tracing to be difficult in the reduction of data as well as appreciable attenuation of the wave velocity. Too few particles increased the probability that no particle may have existed at the test

* In the experiments with non-burning particles this step was omitted.

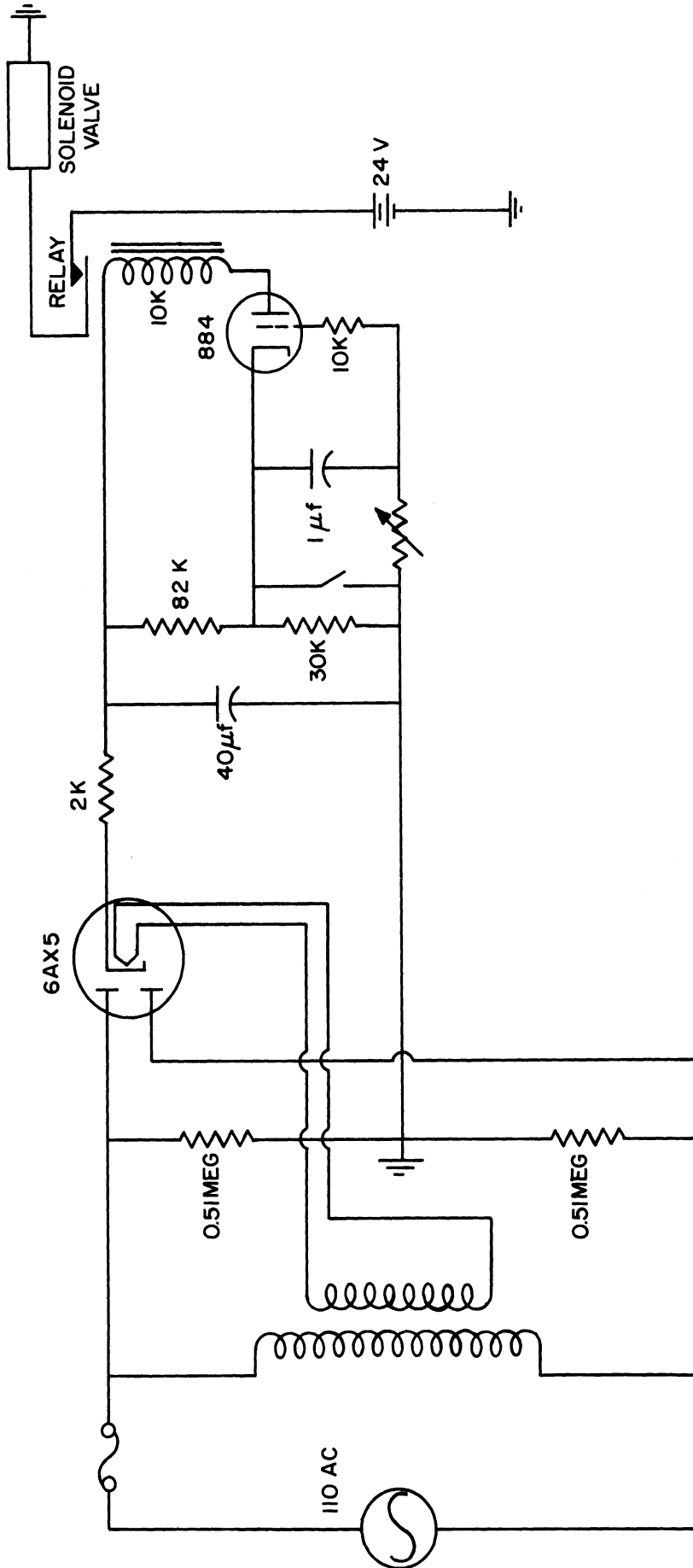


Figure 10. Circuit Diagram for Time Delay Unit.

section when the wave passed. By experimenting with different amounts of particles, it was found that about one tenth of a cubic centimeter was best for reliability of the run and observational purposes. In addition, a test was performed to measure the magnitude of attenuation due to the presence of the particles. It was found that the convective flow velocity would decrease, at the very most, four percent due to the presence of a 1/10 of a cubic centimeter of particles. This particular test was performed at the lower Mach numbers. However, a simple but crude analysis indicated the magnitude would be the same for the larger Mach numbers used in the experiments. The attenuation effect tends to compensate for the existence of hot gases in the test section and the magnitude of the effects were probably of the same order.

The final step in the operational procedure was to develop the film using a manually operated Morse developer kit for 16 mm film. Although a reversal film was used it was not developed in reversal.

IV. DATA REDUCTION AND ERROR ANALYSIS

4.1 Scope of Experimental Results

Although the primary purpose of this study was to determine the drag coefficients of burning particles, a series of tests were performed with non-burning particles in order to gain a comparison between the two cases.

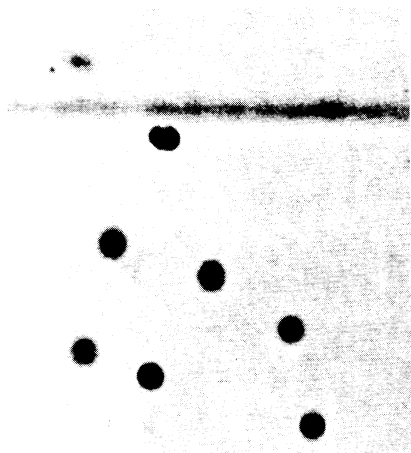
Two kinds of particles were used, gun powder and small glass beads. The gun powders used were ball powders; military ball powder - Type C and Winchester-Western 295 HP ball powder. The glass beads were purchased from Potters Brothers of Carlstadt, New Jersey, in lots of ten pounds. Typical photographs of these particles are shown in Figure 11. The 295 HP ball powder and the glass beads appeared to be nearly spherical in shape while the military powder had a more ellipsoidal shape. A table of the particles' characteristics appears below.

TABLE II
PARTICLE CHARACTERISTICS

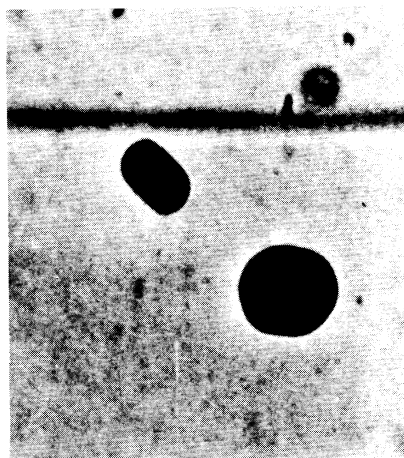
	Density (gms/c. c.)	Approximate Size Range (microns)
Glass Beads	2.50	100 μ - 200 μ
Military Ball Powder-Type C	1.49	200 μ - 250 μ
W. and W. 295 HP Ball Powder	1.67	150 μ - 225 μ

The densities in the above table were obtained experimentally.

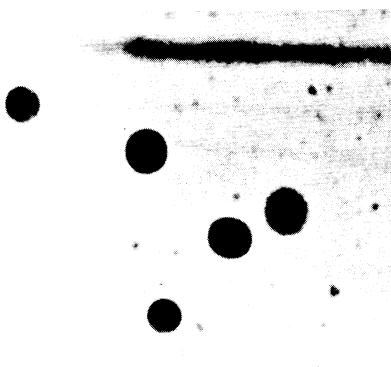
The particles described above together with the range of convective flow velocities obtained in the present experiment gave data for Reynolds numbers varying from 263 to 1610.



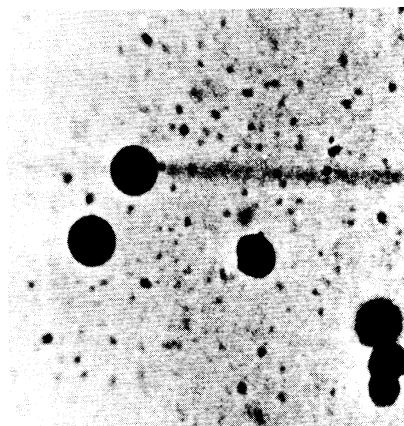
Glass Beads
Mag. 16



Military Ball Powder - type C
Mag. 20



Non-burning 295 HP powder
Mag. 18



Burning 295 HP powder
Mag. 20

Figure 11. Samples of Particles Used in Experiment.

4.2 Data Reduction Equations

In Section II, the general equation for particle dynamics of reacting particles was presented. The equation expressing the drag coefficient in terms of the particle acceleration, applied body force, and mass flux from the surface was

$$C_D \frac{\rho}{2} |\vec{u}| \vec{u} \mathcal{V} = m (\vec{\alpha} - \vec{f}) + \int_S (\rho u^2) \vec{n} dA \quad (2.6)$$

In the present analysis the body force term is the gravitational force on the body and has the same direction but opposite sense of the velocity vector. The acceleration vector has the same direction and sense as the velocity vector. Applying these specializations, the above equation becomes

$$C_D \frac{\rho U^2}{2} \mathcal{V} = m(\alpha + g) + \frac{\vec{u}}{U} \cdot \int_S (\rho u^2) \vec{n} dA \quad (4.1)$$

where $U = |\vec{u}|$

$\alpha = |\vec{\alpha}|$

Obviously, for non-burning particles, the equation to be used in data reduction is

$$C_D = \frac{2m}{\rho U^2} \frac{\alpha + g}{\mathcal{V}} \quad (4.2)$$

For the burning particle some estimate must be made for the final integral in Equation (4.1).

An indication of the order of magnitude of the integral in question was made by assuming a simple model for a burning particle, namely; a flat disc normal to the flow. Assume, in addition, that:

- 1) Stagnation pressure exists over whole forward face
- 2) Pressure coefficient in the wake is -0.4^*
- 3) Burning rate is proportional to pressure ($r = kp$)
- 4) At atmospheric pressure the burning rate is 0.2 inches per second which conforms with experimental evidence presented later.

The model chosen and assumptions made give a conservative estimate of the integral's value. Applying these assumptions the integral evaluates to

$$\frac{\vec{u}}{U} \cdot \int_S (\rho u^2) \vec{n} dA = -\frac{2\pi r_o^2}{S_s} \rho_p^2 [1.4 k q_o]^2 \quad (4.3)$$

where r_o = radius of disc

ρ_p = particle density

ρ_g = gas density at surface

q_o = dynamic pressure

If the characteristic area chosen was the area of the disc normal to the flow, then the contribution to the drag coefficient by the above integral was

$$\Delta C_D = -1.96 \frac{\rho_p^2}{S_s} k^2 q_o \quad (4.4)$$

However for the present experiment the terms in Equation (4.4) had the following orders of magnitude:

$$k \ll 10^{-5} \text{ ft}^3/\#-\text{sec}$$

$$\rho_p < 10^2 \text{ \#/ft}^3$$

$$S_s > 10^{-2} \text{ \#/ft}^3$$

$$q_o < 3 \times 10^2 \text{ \#/ft}^2$$

* The experimental verification of this for a sphere is discussed in Section V.

Thus

$$|\Delta C_D| < \frac{(1.96 \times 10^4 \times 10^{-10} \times 3 \times 10^2)}{10^{-2} g} < 0.2 \times 10^{-2} \quad (4.5)$$

As will be seen later in this section, the contribution of the $m\alpha$ term to the drag coefficient was the order of 0.5. Consequently the mass flux integral was neglected in the calculations for drag coefficient since the error introduced would have been less than one percent. Furthermore, since $\alpha \gg g$ the mg term was also neglected. Thus, the equation used for both the burning and non-burning particles was

$$C_D = \frac{2m}{\rho U^2} \frac{\alpha}{r} \quad (4.2')$$

As Equation (4.2) indicated the data necessary to determine the drag coefficient was:

- 1) particle mass
- 2) particle acceleration
- 3) free stream density
- 4) relative velocity between particle and stream
- 5) particle's characteristic area.

Measurements on the movie film were made by projecting the image of the film on a white background and measuring distances with a scale. The resulting magnification was the product of the camera lens magnification and that due to projection. This was equal to 73 for the particular system used.

The asphericity of the glass beads and 295 HP powder could not be detected by the accuracy of the measurements performed on the film. Consequently, little error would have resulted if these particles were considered spherical for purposes of data reduction.

Assuming a spherical particle of uniform density and the projected area normal to the flow direction as the characteristic area, Equation (4.2) simplified to

$$C_D = \frac{4}{3} \frac{\rho_p}{\rho_g} \frac{d\alpha}{U^2} \quad (4.6)$$

where ρ_g = density of the free stream gas

d = particle diameter

U = relative velocity between particle and stream.

Thus the drag coefficient for a spherical particle depended on the density ratio between particle and stream and the acceleration modulus.

Two pieces of information were obtained from the photographs, namely; variation of particle size and position with time. The experimentally observed wave speeds together with the atmospheric pressure and temperature yielded the gas velocity and density.

4.3 Typical Example of Data Reduction

Figure 12 indicates a sequence of photographs for small glass beads being accelerated upwards by the convective flow behind a shock wave. The measurements indicated on the figure were those actually measured on the projection of the film. The magnification was 73 and the film speed was 6,720 frames per second.

The acceleration was found as a result of plotting the change in distance for each frame versus the number of frames. The graph corresponding to the particular case in question is shown in Figure 13. The slope of this curve was then equated to the acceleration by

$$\alpha = \frac{d \text{ (change in distance per frame)}}{d(\text{frame})} \times \frac{(\text{framing rate})^2}{(12)(73)} \left(\frac{\text{ft}}{\text{sec}^2} \right)$$

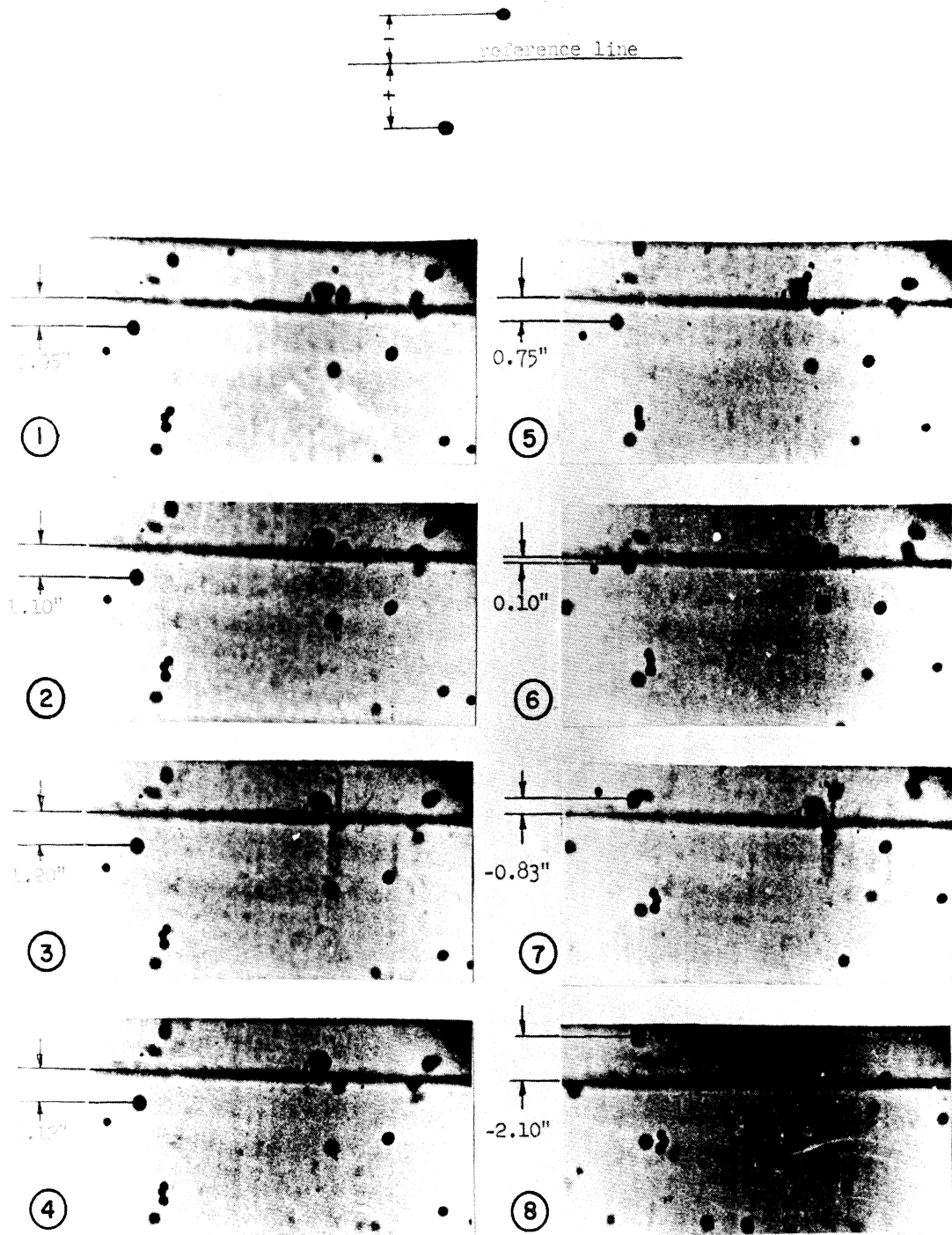


Figure 12. Typical Example of Measurements to Determine Particle Acceleration.

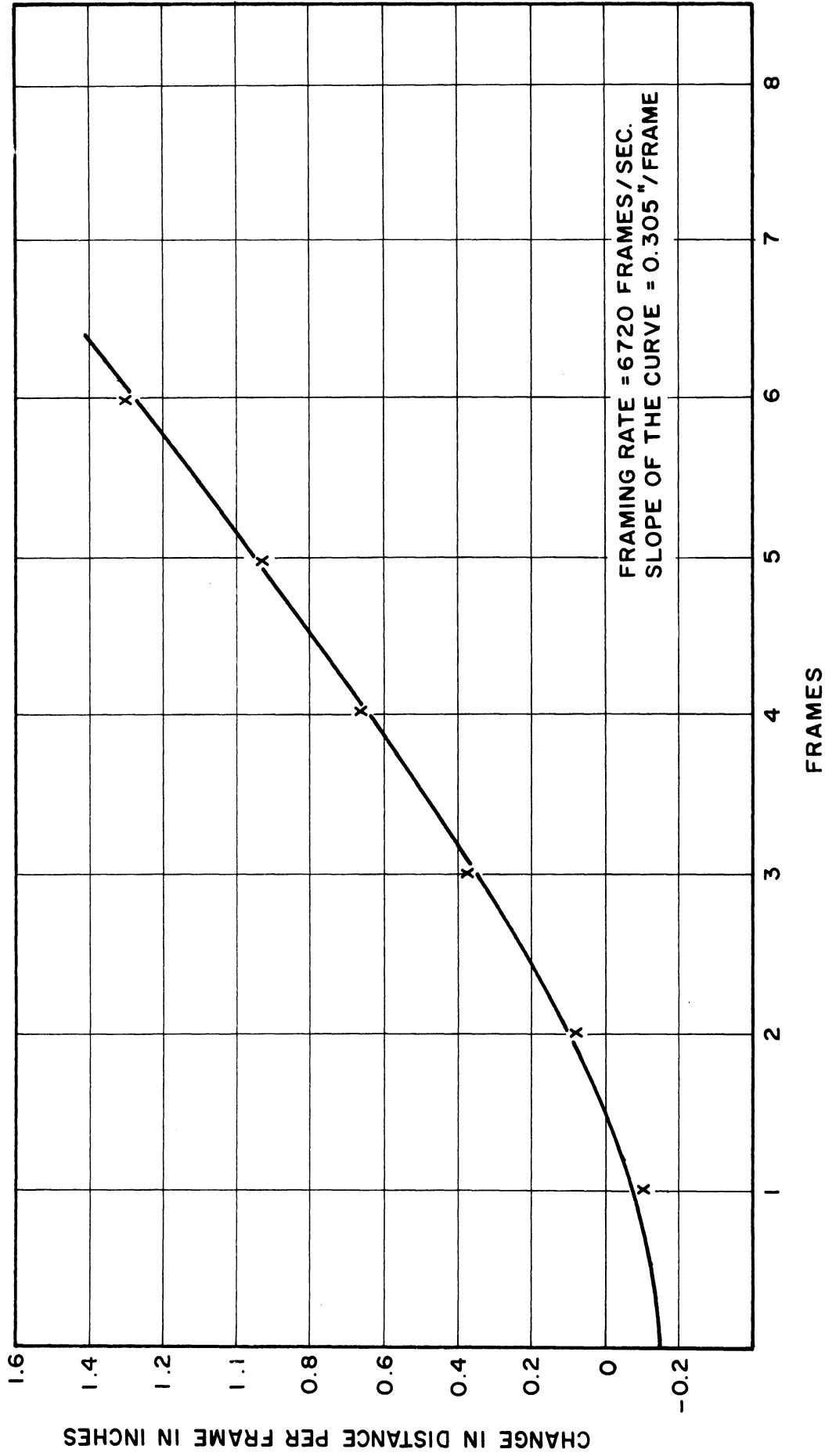


Figure 13. Sample Data Reduction Acceleration Curve.

or

$$\alpha = \frac{(0.305)(6720)^2}{(12)(73)} = 15,730 \text{ ft/sec}^2$$

The average velocity of the particle, over the interval in which the particle appeared to have a constant acceleration, was 5 feet per second.

The size of the particle was also measured on each frame and the average value was used in the calculations. These measurements varied, at most, by five percent and were due to the difficulty in locating the exact edge of the particle. For the case under consideration here the diameter of the particle was 6.40×10^{-4} feet.

The speed of the shock wave in this instance was 1254 feet per second. The temperature was 81°F and the atmospheric pressure was 29.13 inches of mercury.

Since many trial runs had been performed prior to the experiment to check the operation of the electronic equipment it appeared reasonable to assume the temperature within the tube was atmospheric. Thus, the speed of sound and density which were to be used in the shock tube relationships were 1141 feet per second and 0.0714 pounds per cubic foot respectively.

Using the equations for shock tubes given in Reference 21, the convective flow velocity and density behind the wave were calculated to be

$$U_c = 179 \text{ ft/sec}$$

$$\rho_g = 0.0830 \text{ lb./ft.}^3$$

The average relative velocity between the particle and the stream was

$$U = 174 \text{ ft/sec}$$

Using the above values in Equation (4.6) yielded the result

$$C_D = 0.835$$

The Reynolds number calculated using the viscosity corresponding to the atmospheric temperature was

$$Re = 337$$

Equation (4.6) could not be used for the military ball powder since its asphericity was most apparent. It appeared to be ellipsoidal in shape and this assumption was used in the data reduction calculations. Also by observing the orientation of the particles an estimate of the projected area normal to the stream was obtained. For the characteristic length in the formulation of Reynolds numbers, the diameter of a sphere of equivalent surface area was employed.

Table III summarizes the results for burning and non-burning particles. In addition, the experimental results are plotted in Figures 14 and 15.

The most disappointing feature of the whole experiment was the difficulty in measuring burning rates. Due to the short times available to trace single particles and the relatively slow burning rate of gun powder, the particle size did not decrease sufficiently to obtain an accurate measurement. However, in some instances, it was possible to identify a particle after it had fallen below the field of view and re-appeared due to the convective flow. In these cases sufficient time had elapsed to measure burning rates. The few measurements which were possible indicated the military ball powder had a burning rate ranging from 0.13 to 0.16 inches per second while the 295 HP powder ranged from 0.06 to 0.08 inches per second.

Equation (4.6) indicates that the acceleration modulus $\left(\frac{\alpha d}{U^2}\right)$ for the Reynolds number range considered in this report was

$$\frac{\alpha d}{U^2} = O\left(\frac{\rho_g}{\rho_p}\right) = O(10^{-3})$$

TABLE III

DATA SUMMARY

Acceleration ft/sec ²	Relative Velocity ft/sec.	Diameter ft.	Gas Density lb./ft ³	C _D	Re
Glass Beads					
15,730	174	6.40x10 ⁻⁴	0.0830	0.835	337
20,650	173	4.91	0.0830	0.850	263
17,550	173	5.60	0.0830	0.824	300
19,700	182	5.02	0.0836	0.743	278
15,900	185	6.16	0.0836	0.713	347
17,000	185	5.82	0.0836	0.720	328
15,200	185	6.70	0.0836	0.740	377
64,600	395	6.71	0.1030	0.561	1007
64,600	395	5.28	0.1030	0.442	795
57,300	395	5.59	0.1030	0.494	830
63,800	408	5.93	0.1030	0.459	907
71,500	408	6.27	0.1030	0.544	958
29,500	240	7.06	0.0892	0.845	552
37,500	240	5.70	0.0892	0.865	460
36,700	305	7.02	0.0949	0.605	742
39,800	300	5.81	0.0949	0.563	595
41,000	300	4.90	0.0949	0.489	510
Non-Burning 295 HP Powder					
29,350	313	9.69x10 ⁻⁴	0.0949	0.435	1040
28,800	254	10.41	0.0980	0.663	942
25,100	254	9.00	0.0980	0.500	815
30,400	253	8.50	0.0980	0.579	840
28,600	251	9.40	0.0980	0.609	840
11,070	156	9.24x10 ⁻⁴	0.0836	0.701	440
12,720	151	9.35	0.0836	0.817	450
10,500	156	8.44	0.0836	0.609	402
Non-Burning Military Ball Powder					
18,800	270	1.623x10 ⁻³	0.0911	0.510	1460
23,200	270	1.790	0.0911	0.685	1610
24,500	268	1.412	0.0911	0.486	1260
12,100	265	1.657	0.0911	0.505	1460

TABLE III (CONT'D)

Acceleration ft/sec ²	Relative Velocity ft/sec.	Diameter ft.	Gas Density lb./ft ³	C _D	Re
Burning 295 HP Powder					
22,450	233	9.00x10 ⁻⁴	0.0886	0.640	640
17,520	222	8.78	0.0886	0.525	610
23,700	222	9.30	0.0886	0.775	630
15,900	173	9.01	0.0836	0.800	475
14,800	173	8.66	0.0836	0.717	457
16,450	161	7.98	0.0836	0.843	392
13,170	155	9.66	0.0836	0.884	456
Burning Military Ball Powder					
32,600	254	1.110x10 ⁻³	0.0905	0.670	930
23,700	254	1.603	0.0905	0.506	1310
17,800	242	1.488	0.0905	0.510	1190
4,092	114	1.407	0.0793	0.606	406
4,322	106	1.402	0.0793	0.766	431
3,842	111	1.778	0.0793	0.779	571
4,277	135	1.903	0.0819	0.680	565
7,690	165	2.170	0.0862	0.651	850
Balloon Experiment					
413	23	0.35	0.0723	0.365	20,800

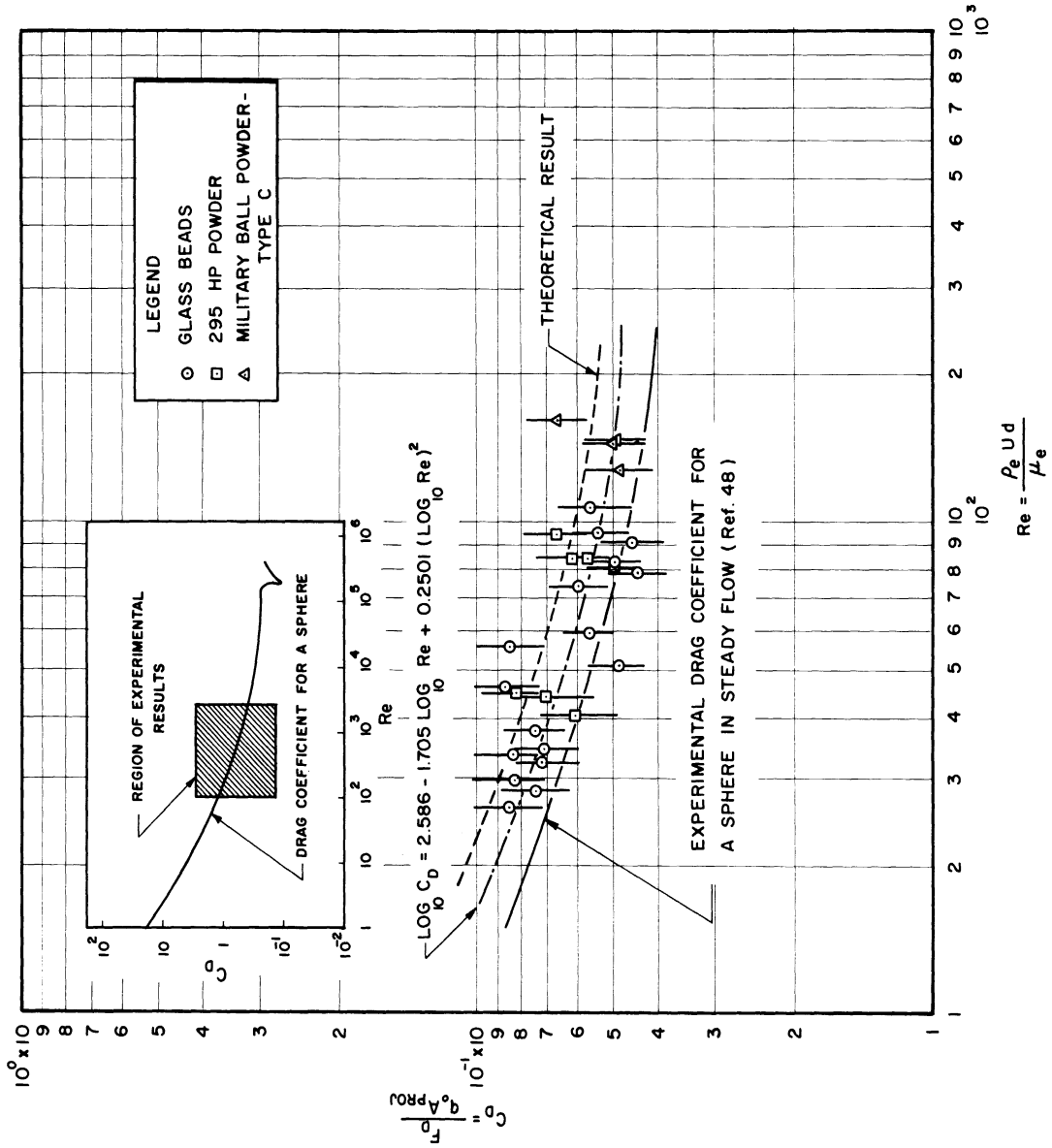


Figure 14. Drag Coefficient Versus Reynolds Number Non-Burning Particles.

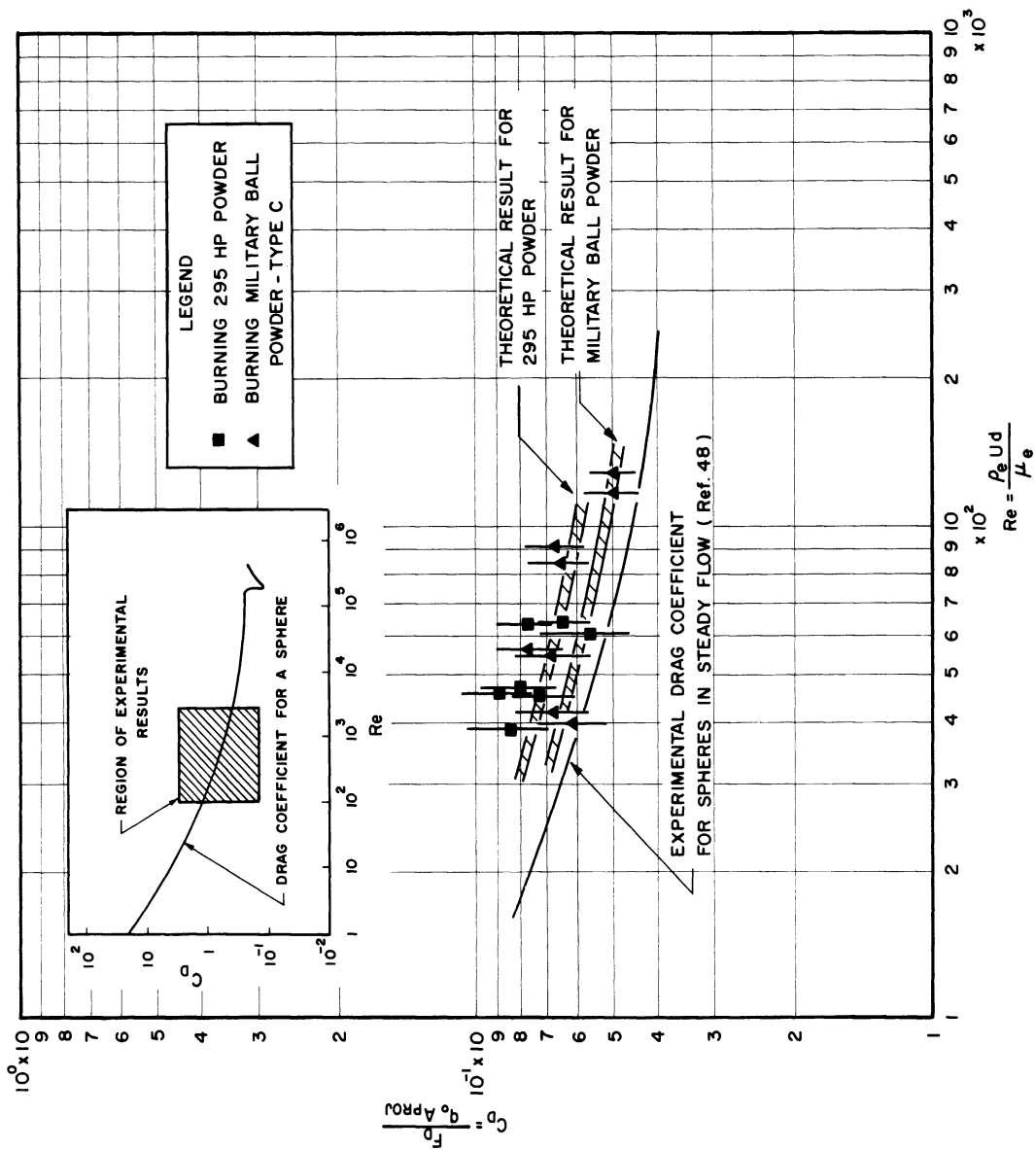


Figure 15. Drag Coefficient Versus Reynolds Number - Burning Particles.

In order to investigate the effect of acceleration moduli which were the order of one a very simple but effective experiment was suggested. Balloons were released in a low speed wind tunnel and their ensuing motion recorded by a movie camera. The major difficulty was supplying sufficient light inside the tunnel for the high speed photography. Although the photographs were most difficult to read, indicative results were obtained and appear in Table III. The drag coefficient obtained was discernibly less than the corresponding value for a sphere in steady flow.

Another characteristic of the experimental data which should be mentioned was the difficulty in distinguishing burning and non-burning particles in the photographs (Figure 10). This was probably the result of the surface reaction zone being small. In the photographs of the small burning droplets reported by Rabin⁽¹²⁾ burning regions were also nondetectable.

4.4 Error Analysis

The equation used for the majority of the data reduction was

$$C_D = \frac{4}{3} \frac{\rho_p}{\rho_g} \frac{\alpha d}{U^2} \quad (4.6)$$

As illustrated above, the relative velocity was essentially the convective flow velocity behind the wave, so for purposes of error analysis, the above equation was written

$$C_D = \frac{4}{3} \frac{\rho_p}{\rho_g} \frac{\alpha d}{U_c^2} \quad (4.6)$$

However, ρ_g was a function of U_c and a_o (speed of sound in the undisturbed gas) and for weak shock waves the following relation was valid

$$C_D = \frac{4}{3} \frac{\rho_p}{\rho_o} \frac{1}{(1 + \frac{U_c}{a_o})} \frac{\alpha d}{U_c^2} \quad (4.7)$$

Since all the quantities in this expression were independently observed values, the probable error of C_D , ΔC_D , was written in terms of the probable errors of each quantity as⁽²²⁾

$$\frac{\Delta C_D}{C_D} = \left\{ \left(\frac{\Delta \alpha}{\alpha} \right)^2 + \left(\frac{\Delta \rho_p}{\rho_p} \right)^2 + \left(\frac{\Delta d}{d} \right)^2 + \left[4 + \left(\frac{U_c}{a_o} \right)^2 \right] \left(\frac{\Delta U_c}{U_c} \right)^2 \right\} \quad (4.8)$$

where the probable error in determining the atmospheric density was neglected.

Also in the present experiment

$$\left(\frac{\frac{U_c}{a_o}}{1 + \frac{U_c}{a_o}} \right)^2 = O \left(\frac{1}{25} \right) \quad (4.9)$$

and this term could be neglected compared to 4. The expression for the probable error reduced to

$$\frac{\Delta C_D}{C_D} = \left\{ \left(\frac{\Delta \alpha}{\alpha} \right)^2 + \left(\frac{\Delta \rho_p}{\rho_p} \right)^2 + \left(\frac{\Delta d}{d} \right)^2 + 4 \left(\frac{\Delta U_c}{U_c} \right)^2 \right\} \quad (4.10)$$

The wave speed being the experimentally observed quantity, it was most convenient to express the probable error of the convective flow velocity in terms of the wave speed error, or

$$\frac{\Delta U_c}{U_c} = \frac{1}{M-1} \frac{\Delta c_s}{c_s}$$

where the assumption of weak shock waves had once more been applied.

The probable error in the determination of the acceleration was a result of two effects; incorrect distance measurements and framing rate data. The probable error in measurements was estimated by taking a typical

example, finding the slopes which exist between all possible pairs of experimental points on the change in velocity versus frame curve, averaging the results, and using the deviations from the average to calculate a probable error. To find the framing rate it was necessary to count frames between timing marks. A reasonable error would be one frame out of fifty or 2%. Combining both effects a probable error of 4.5% was obtained.

The particle density was calculated by immersing a known mass of powder in water and noting the change in volume. A reasonable probable error for this operation was estimated at 3%.

Errors resulted in measuring the diameter by being unable to precisely locate the particle's edge. A typical probable error for such measurements was found to be 4%.

It is imperative at this point to say errors in the magnification factor could have resulted from the particle not being exactly at the test section center. However, only those particles in sharpest focus were measured and the error in magnification would be small but inestimable by present knowledge.

The wave speed was calculated by dividing the distance between the transducers by the time interval recorded and correcting this value for attenuation with the relation

$$c_s = \bar{K}c_{s_0}$$

where c_s = wave speed in test section

c_{s_0} = wave speed at position of measurements

\bar{K} = attenuation factor.

In order to determine \bar{K} a series of experiments were performed with the

transducers across the test section and another series were performed with them below the test section in the position used to record the experimental wave speeds. The probable error in the evaluation of the speed at the test section was written independently of \bar{K} in the form

$$\frac{\Delta c_s}{c_s} = \left[\left(\frac{\Delta c_{s,T}}{c_{s,T}} \right)^2 + \left(\frac{\Delta c_{s_o,T}}{c_{s_o,T}} \right)^2 \right]^{1/2}$$

where $\Delta c_{s,T}$ and $\Delta c_{s_o,T}$ were the probable errors found for the series of tests employed to determine \bar{K} .

Errors could also have occurred in the wave speed measurement by an incorrect time measurement or inaccurate distance measurement between the transducers. The probable error due to the timer would have been the order of 1/10 of a percent and was neglected. The error due to distance measurement was estimated at 0.25 percent. Combining this value with those obtained for attenuation effects resulted in the following table.

TABLE IV

WAVE SPEED PROBABLE ERRORS

<u>Material</u>	<u>$\Delta c_s / c_s$</u>
Tissue paper	1.30%
Scratch paper	0.77%
Bond paper	1.08%

It must be noted here that the effect of the hot gas in the chamber and attenuation of the wave due to the particles had been omitted since they were classified as systematic errors.

Substituting the values obtained above into Equation (4.10)

results in

$$\frac{\Delta C_D}{C_D} = \left[0.00454 + \frac{4}{(M-1)^2} \left(\frac{\Delta C_s}{C_s} \right)^2 \right]^{\frac{1}{2}}$$

This equation is then used to calculate the probable errors and they appear as vertical lines on Figures 14 and 15.

V. THEORETICAL ANALYSIS

5.1 Scope of the Analysis

In this section a theoretical analysis is presented in an effort to describe the fluid dynamic aspects of both liquid drops and solid particles in convective flow fields. The analysis will be limited to the regime of continuum gas dynamics and to flows in which the boundary layer formed on the particle is much smaller in size than the particle diameter.

The particular problems to be considered may be summarized as follows:

- a) Evaporation rate of liquid drops
- b) Effect of evaporation on drag coefficient
- c) Effect of particle acceleration on drag coefficient
- d) Effect of burning on drag coefficient.

These problems will be treated by rewriting the governing equations in integral form and solving the resulting equations to conform with the appropriate boundary conditions. This technique fails to give a detailed description of the flow field but serves to indicate the significant parameters involved and the importance of each.

5.2 Basic Equations

The two fundamental equations which will be used in the following analysis are the continuity equation and momentum equation for fluid flow.

The continuity equation for species k may be written, using index notation, in the following form⁽²³⁾

$$\frac{\partial}{\partial t} (\rho c_k) + \frac{\partial}{\partial x_\alpha} (\rho u_{\alpha,k} c_k) = \dot{w}_k \quad * \quad (5.1)$$

where ρ = density

c_k = mass fraction of species k

$u_{i,k}$ = averaged flow velocity of species k in "c" direction

\dot{w}_k = net mass rate of production of species k per unit volume by chemical reaction.

Summing Equation (5.1) over all species, the overall continuity equation is obtained in the form

$$\frac{\partial \rho}{\partial t} + \frac{\partial}{\partial x_\alpha} (\rho u_\alpha) = 0 \quad (5.2)$$

taking u_i as the mass averaged velocity, or

$$u_i = \sum_{k=1}^n c_k u_{i,k} \quad (5.3)$$

The equation expressing the balance between the inertial and applied forces on a fluid element has the form

$$\rho \frac{\partial V_i}{\partial t} + \frac{\partial}{\partial t} (\rho u_i) + \frac{\partial}{\partial x_\alpha} (\rho u_i u_\alpha) = - \frac{\partial p}{\partial x_i} + \frac{\partial}{\partial x_\alpha} (\tau_{i\alpha}^V + \tau_{i\alpha}^D) \quad (5.4)$$

where p = pressure

τ^V = stress tensor due to viscous forces

τ^D = stress tensor arising from diffusion velocities

V_i = velocity of coordinate system with respect to an inertial reference system.

* Greek letters shall be used for the summation indicies.

This equation neglects any body forces which may exist. In addition, it is restricted to a coordinate system which undergoes translation but no rotation with respect to inertial space.

In Appendix B the above set of equations are rewritten employing non-dimensional variables and specialized to a spherical coordinate system. An order of magnitude analysis is performed assuming the non-dimensional boundary layer thickness is small ($\bar{\delta} \ll 1$) and retention of the significant terms leads to the conventional boundary layer equations. As found in Appendix B, the governing equations are

$$\begin{aligned} \frac{1}{r^2} \frac{\partial}{\partial r} (\rho r^2 u_r c_k) + \frac{1}{r \sin \theta} \frac{\partial}{\partial \theta} (\rho u_\theta \sin \theta c_k) + \frac{\partial}{\partial t} (\rho c_k) \\ = \frac{1}{r^2} \frac{\partial}{\partial r} (\rho D r^2 \frac{\partial c_k}{\partial r}) \end{aligned} \quad (5.5)$$

$$\frac{1}{r^2} \frac{\partial}{\partial r} (\rho r^2 u_r) + \frac{1}{r \sin \theta} \frac{\partial}{\partial \theta} (\rho u_\theta \sin \theta) = -\frac{\partial \rho}{\partial t} \quad (5.6)$$

$$\begin{aligned} \rho \frac{\partial v_\theta}{\partial t} + \frac{1}{r^2} \frac{\partial}{\partial r} (\rho u_r r^2 u_\theta) + \frac{1}{r \sin \theta} \frac{\partial}{\partial \theta} (\rho u_\theta^2 \sin \theta) \\ + \frac{\partial}{\partial t} (\rho u_\theta) = -\frac{1}{r} \frac{\partial p}{\partial \theta} + \frac{1}{r^2} (r^2 \mu \frac{\partial u_\theta}{\partial r}) \end{aligned} \quad (5.7)$$

$$\frac{\partial p}{\partial r} = O\left(\frac{\rho U^2}{L}\right) \quad (5.8)$$

In Equation (5.5) the restriction of no chemical reaction occurring in the boundary layer was applied. This does not, however, preclude reactions such as burning occurring on the particle's surface.

The particles found in rocket motor exhausts may possibly have various irregular shapes. However, for purposes of analysis, a spherical shape will be assumed. This assumption is probably not too severe as it seems probable that a burning particle will tend to approach a spherical shape as burning progresses.

Integrating the continuity Equation (5.6) over "r" from the particle surface ($r = a$) to some arbitrary distance ($r = r_e$) gives

$$\rho r^2 u_r \Big|_a^{r_e} + \frac{1}{\sin \theta} \int_a^{r_e} \frac{\partial}{\partial \theta} (\sin \theta r \rho u_\theta) dr = - \int_a^{r_e} r^2 \frac{\partial \rho}{\partial t} dr \quad (5.9)$$

or

$$(\rho r^2 u_r) \Big|_{r_e} = a^2 (\rho u_r)_s - \frac{1}{\sin \theta} \int_a^{r_e} \frac{\partial}{\partial \theta} (\sin \theta r \rho u_\theta) dr - \int_a^{r_e} r^2 \frac{\partial \rho}{\partial t} dr \quad (5.10)$$

where the subscript "s" refers to the surface. Integration of (5.5) between the surface and edge of the diffusion boundary layer ($r = a + \delta_D$) leads to

$$\begin{aligned} (\rho r^2 u_r c_k) \Big|_{a+\delta_D} &= a^2 (\rho u_r)_s c_{ks} - \frac{1}{\sin \theta} \int_a^{a+\delta_D} \frac{\partial}{\partial \theta} (\sin \theta r \rho u_\theta c_k) dr \\ &- \int_a^{a+\delta_D} r^2 \frac{\partial}{\partial t} (\rho c_k) dr - a^2 \left(\rho D \frac{\partial c_k}{\partial r} \right)_s \end{aligned} \quad (5.11)$$

By definition, $\frac{\partial c_k}{\partial r} = 0$ at the edge of the diffusion boundary layer.

In accordance with Nusselt's early work in evaporation problems⁽²⁴⁾ it is reasonable to require that the surrounding gas cannot penetrate the particle surface. If c_s represents the mass fraction of the surrounding gas, this restriction amounts to

$$-(\rho u_r)_s c_{s_s} + \rho D \frac{\partial c_e}{\partial r} \Big|_s = 0 \quad (5.12)$$

If the problem is simplified to a binary mixture, i.e., the surrounding gas and the particle's vapor, the mass flux from the surface can be written as

$$(\rho u_r)_s = \frac{\rho D}{(c_s - 1)} \frac{\partial c}{\partial r} \Big|_s \quad (5.13)$$

where c = mass concentration of particle vapor.

c_s = mass concentration of particle vapor at the surface.

Substituting Equations (5.10) and (5.13) into Equation (5.11) yields the integrodifferential equation for the vapor concentration in the diffusion boundary layer

$$\begin{aligned} & \frac{1}{\sin \theta} \int_a^{a+\delta_0} \frac{\partial}{\partial \theta} [\sin \theta r \rho u_\theta (c_e - c)] dr + \int_a^{a+\delta_0} r^2 \frac{\partial}{\partial t} (\rho c_e - \rho c) dr \\ & = a^2 (\rho u_r)_s (c_e - 1) \end{aligned} \quad (5.14)$$

where c_e = vapor concentration at edge of the diffusion boundary layer.

Implicit in the derivation of the above equation are the following assumptions

$$\frac{\partial c_e}{\partial \theta} = \frac{\partial c_e}{\partial t} = 0$$

Since the integrands are identically zero at the upper limit Equation (5.14)

can further be simplified to

$$\frac{1}{\sin \theta} \frac{\partial}{\partial \theta} \sin \theta \int_a^{a+\delta_D} r \rho u_\theta (c_e - c) dr + \frac{\partial}{\partial t} \int_a^{a+\delta_D} r^2 \rho (c_e - c) dr = a^2 (\rho u_r)_s (c_e - 1) \quad (5.15)$$

A change of integration variable of the first integral on the left to $r = a + g$ results in

$$\int_a^{a+\delta_D} r \rho u_\theta (c_e - c) dr = a \int_0^{\delta_D} \rho u_\theta (c_e - c) dg + \int_0^{\delta_D} g \rho u_\theta (c_e - c) dg \quad (5.16)$$

However

$$\int_0^{\delta_D} g \rho u_\theta (c_e - c) dg \leq \delta_D \int_0^{\delta_D} \rho u_\theta (c_e - c) dg \quad (\text{ref. 25})$$

To be consistent with the fundamental assumption used to obtain the governing equations, namely $\delta_D/d \ll 1$, the second integral on the right in Equation (5.16) may be neglected in comparison with the first. Applying the same reasoning to the second integral of Equation (5.15) further simplifies the expression to

$$\frac{a}{\sin \theta} \frac{\partial}{\partial \theta} \sin \theta \int_0^{\delta_D} \rho u_\theta (c_e - c) dg + a^2 \frac{\partial}{\partial t} \int_0^{\delta_D} \rho (c_e - c) dg = a^2 (\rho u_r)_s (c_e - 1) \quad (5.17)$$

The corresponding integral relationship for the momentum equation is obtained using the same scheme as above. Integration of Equation (5.7) with respect to "r" from the particle surface to the edge of the velocity boundary layer ($r = a + \delta_v$) yields

$$\int_a^{a+\delta_v} r^2 \rho \frac{\partial v_\theta}{\partial t} dr + \int_a^{a+\delta_v} r^2 \frac{\partial}{\partial t} (\rho u_\theta) dr + (r^2 \rho u_r)_{a+\delta_v} U_e + \frac{1}{\sin \theta} \int_a^{a+\delta_v} r \frac{\partial}{\partial \theta} (\sin \theta \rho u_\theta) dr = - \int_a^{a+\delta_v} r \frac{\partial p}{\partial \theta} dr - a^2 \tau_s \quad (5.18)$$

where τ_s = shearing stress at the surface

U_e = tangential velocity at the edge of the boundary layer.

Integration of Equation (5.8) over 'r' introduces the useful result

$$\frac{\Delta p}{\rho} = O\left(\frac{\delta v}{a}\right) \quad (5.19)$$

or, in other words, $\frac{P_e}{P_s} \approx 1$ since $\frac{\delta v}{a} \ll 1$. Thus it is permissible to express the pressure integral in (5.18) as

$$\int_a^{a+\delta v} r \frac{\partial p}{\partial \theta} dr = \int_a^{a+\delta v} r \frac{\partial p_e}{\partial \theta} dr \quad (5.20)$$

The variation in pressure with θ outside the boundary layer is directly obtainable from Equation (5.7) since, by definition,

$$\frac{\partial}{\partial r} (\)_e = 0. \quad \text{Thus}$$

$$-\frac{\partial p_e}{\partial \theta} = r \frac{\partial}{\partial t} (\rho_e U_e) + r \rho_e \frac{\partial V_\theta}{\partial t} + \frac{1}{\sin \theta} \frac{\partial}{\partial \theta} (\rho_e U_e^2 \sin \theta) \quad (5.21)$$

After substitution of (5.21) into Equation (5.20) and some further manipulations, the following equation is produced

$$\begin{aligned} & \frac{\partial V_\theta}{\partial t} \int_a^{a+\delta v} r^2 (\rho - \rho_e) dr + \frac{\partial}{\partial t} \int_a^{a+\delta v} r^2 (\rho_e U_e - \rho u_\theta) dr \\ & + U_e \frac{\partial}{\partial t} \int_a^{a+\delta v} r^2 (\rho - \rho_e) dr + \frac{\partial U_e}{\partial \theta} \int_a^{a+\delta v} r (\rho_e U_e - \rho u_\theta) dr \\ & + \frac{1}{\sin \theta} \frac{\partial \sin \theta}{\partial \theta} \int_a^{a+\delta v} r \rho u_\theta (U_e - u_\theta) dr - \frac{(\rho U_r)_s}{(\rho U)_e} \rho_e U_e^2 = \tau_s a^2 \end{aligned} \quad (5.22)$$

Changing the variable of integration to "g" in the above integrals and neglecting the smaller terms, the momentum equation becomes

$$\begin{aligned}
 & - \left(\frac{\partial V_\theta}{\partial t} + U_e \frac{\partial}{\partial t} \right) \rho_e \int_0^{\delta_v} \left(1 - \frac{\rho}{\rho_e} \right) dq + \left(\frac{\partial}{\partial t} + \frac{1}{a} \frac{\partial U_e}{\partial \theta} \right) \rho_e U_e \int_0^{\delta_v} \left(1 - \frac{\rho u_\theta}{\rho_e U_e} \right) dq \\
 & + \frac{1}{a \sin \theta} \frac{\partial}{\partial \theta} \sin \theta \rho_e U_e^2 \int_0^{\delta_v} \frac{\rho u_\theta}{\rho_e U_e} \left(1 - \frac{u_\theta}{U_e} \right) dq - \frac{(\rho u_r)_s}{(\rho_e U_e)} \rho_e U_e^2 \quad (5.23) \\
 & = \tau_s
 \end{aligned}$$

The two integrals expressing the conventional displacement and momentum thickness are at once recognizable. The third integral

$$\int_0^{\delta_v} \left(1 - \frac{\rho}{\rho_e} \right) dq$$

could be called a "density" thickness and will only appear when the density distribution in the boundary layer changes with time or the coordinate system is undergoing acceleration with respect to inertial space.

5.3 Evaluation of Integrals

The next step is to evaluate the integrals so as to reduce the equations to differential equations once more. The scheme to be used here is that reported by Covert⁽²⁶⁾ and is based on changing the variable of integration to the velocity distribution using the relationship

$$dq = \frac{\mu}{\tau} du_\theta \quad (5.24)$$

Applying this to the momentum integral in Equation (5.23) results in

$$\int_0^{\delta_v} \frac{\rho u_\theta}{\rho_e U_e} \left(1 - \frac{u_\theta}{U_e} \right) dq = \frac{\mu_e U_e}{\tau_s} \int_0^1 \frac{\rho \mu}{\rho_e \mu_e} \frac{\tau_s}{\tau} \eta (1-\eta) d\eta \quad (5.25)$$

where $\eta = \frac{u_\theta}{U_e}$. If the assumption is made that

$$\frac{\rho \mu}{\rho_e \mu_e} \cdot \frac{\tau_s}{\tau} = f(\eta) \quad \text{only} \quad (5.26)$$

the momentum integral further reduces to

$$\int_0^{\delta_v} \frac{\rho u_\theta}{\rho_e U_e} \left(1 - \frac{u_\theta}{U_e}\right) dq = \frac{\mu_e U_e}{\tau_s} A \quad (5.27)$$

where

$$A = \int_0^1 f(\eta) \eta (1-\eta) d\eta$$

Similarly, should $\frac{\rho}{\rho_e} = f(\eta)$ then the displacement integral be-

comes

$$\int_0^{\delta_v} \left(1 - \frac{\rho u_\theta}{\rho_e U_e}\right) dq = \frac{\mu_e U_e}{\tau_s} \int_0^1 \frac{\rho \mu}{\rho_e \mu_e} \frac{\tau_s}{r} \left(\frac{\rho_e}{\rho} - \eta\right) d\eta = \frac{\mu_e U_e}{\tau_s} B \quad (5.28)$$

and the density integral reduces to

$$\int_0^{\delta_v} \left(1 - \frac{\rho}{\rho_e}\right) dq = \frac{\mu_e U_e}{\tau_s} \int_0^1 \frac{\rho \mu}{\rho_e \mu_e} \frac{\tau_s}{r} \left(\frac{\rho_e}{\rho} - 1\right) d\eta = \frac{\mu_e U_e}{\tau_s} C \quad (5.29)$$

5.4 Steady State Drag Coefficient for a Sphere

In order to assess the usefulness of the integral technique, the simple case of steady flow over a sphere will be investigated. The analysis will serve to indicate the dependence of the result on the particular functional form chosen for Equation (5.26) and will serve as a starting point for many of the analyses to follow.

For steady flow, a stationary coordinate system, and no mass injection at the surface, the momentum Equation (5.23) reduces to

$$\tau_s = \frac{1}{a} \frac{dU_e}{d\theta} \rho_e U_e \int_0^{\delta_v} \left(1 - \frac{\rho u_\theta}{\rho_e U_e}\right) dq + \frac{1}{a \sin \theta} \frac{d \sin \theta}{d\theta} \rho_e U_e^2 \int_0^{\delta_v} \frac{\rho u_\theta}{\rho_e U_e} \left(1 - \frac{u_\theta}{U_e}\right) dq \quad (5.30)$$

Substituting the values of the integrals obtained above, this equation becomes

$$a \tau_s = B \frac{dU_e}{d\theta} \frac{\rho_e U_e^2}{\tau_s} + \frac{A}{\sin \theta} \frac{d \sin \theta}{d\theta} \frac{\rho_e \mu_e U_e^3}{\tau_s} \quad (5.31)$$

If $\frac{\partial \mu_e}{\partial \theta} = 0$ and the classical, incompressible, inviscid velocity distribution

$$U_e = \frac{3}{2} U \sin \theta \quad (5.32)$$

is chosen for the flow outside the boundary layer, the equation further simplifies to

$$\frac{d\zeta^2}{d\theta} + 2\left(1 + \frac{B}{A}\right) \frac{\cos \theta}{\sin \theta} \zeta^2 = \frac{3}{8} \frac{1}{A} \sin^3 \theta \quad (5.33)$$

where $\zeta = \frac{9}{4} \frac{\sin^3 \theta}{c_f \sqrt{Re}}$. In this instance the skin friction coefficient is defined as

$$C_f = \frac{\tau_s}{\frac{1}{2} \rho_e U^2} \quad (5.34)$$

Solving the differential equation gives the skin friction distribution as

$$C_f \sqrt{Re} = \frac{\left(\frac{3}{2}\right)^{3/2} 2\sqrt{A} \sin^{4+\frac{B}{A}} \theta}{\left[\int_0^\theta \sin^{5+\frac{2B}{A}} \lambda d\lambda\right]^{1/2}} \quad (5.35)$$

The solution now depends on the particular distribution of $\frac{\rho \mu}{\rho_e \mu_e} \frac{\tau_s}{\tau}$ to be chosen since this will determine the constants A and B. For an unheated particle in a low Mach number flow the variations of density and temperature will be small so a reasonable assumption would be

$$\frac{\rho \mu}{\rho_e \mu_e} = 1 \quad \& \quad \frac{\tau_s}{\tau} = 1$$

The solution will then depend on the shear distribution through the boundary layer. Covert⁽²⁵⁾ suggests the following distributions:

	τ/τ_s	A	B
Case I	1	1/6	1/2
Case II	$\sqrt{1-\eta^2}$	0.215	0.571
Case III	1- η	1/2	1

The particular velocity distributions corresponding to each case are shown in Figure 16. For reference the Blasius solution for a flat plate has been included and is seen to match very closely with Case II.

Figure 17 indicates the results of evaluating Equation (5.35) for the three cases of shear distribution described above. On the same diagram the results of Tomotika⁽²⁷⁾ are shown. Tomotika assumed the velocity distribution through the boundary layer could be expressed by a fourth power polynomial. This distribution is more flexible than those used in the present analysis and should give a more reliable result although the effort required is considerably greater. In the region of the stagnation point Case III matches Tomotika's results very well but tends to exceed his values for the larger angles. In the region of the separation point the present analysis fails due to the invariance of the shear distribution. However, this will not be a serious shortcoming since the major contribution of the skin friction to the drag coefficient occurs on the forward portion of the sphere.

To obtain the complete drag coefficient it is necessary to add the contributions due to skin friction and pressure forces. The above analysis can be used to obtain the drag coefficient due to shear forces by performing the integration

$$\sqrt{Re} C_{Df} = 2 \int_0^{\theta_s} C_f \sqrt{Re} \sin^2 \theta d\theta \quad (5.36)$$

where θ_s = angle of flow separation. This drag coefficient is based on the frontal area of the sphere. If the classical pressure coefficient

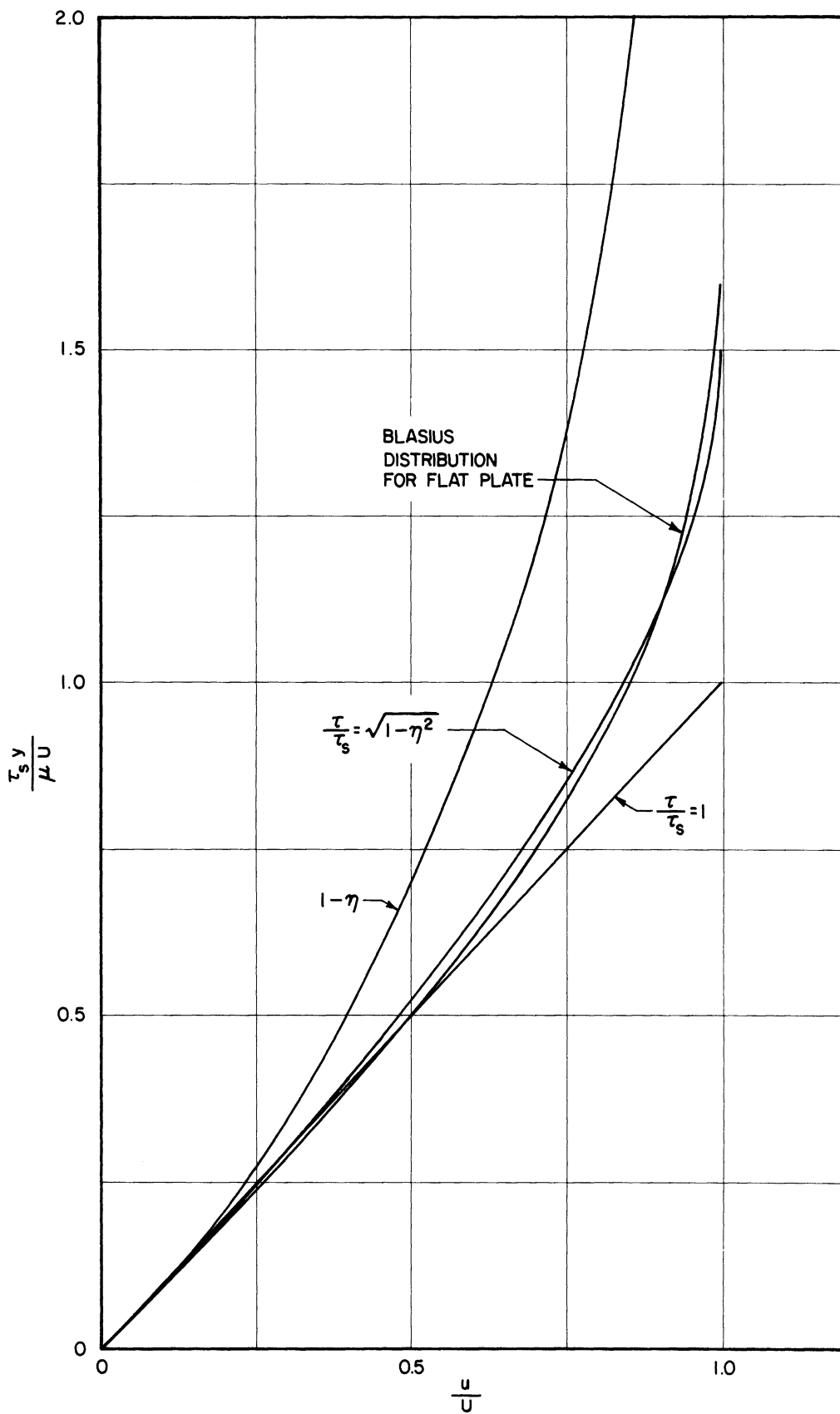


Figure 16. Velocity Distribution Corresponding to the Three Shear Distributions.

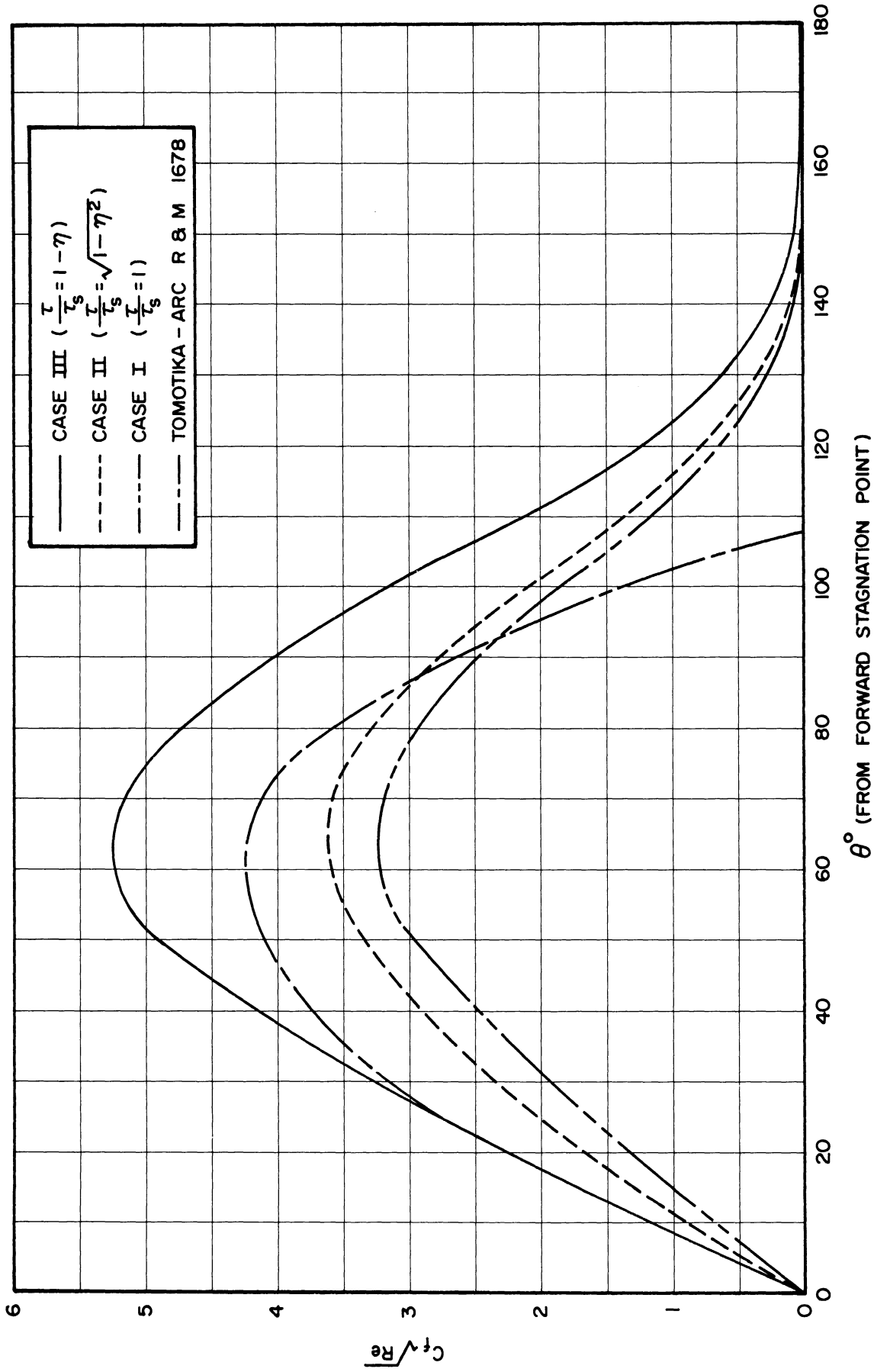


Figure 17. Variation of Skin Friction over Sphere Surface.

for a sphere in steady flow is assumed to be valid up to the separation angle and a constant pressure coefficient in the wake (C_{p_w}) is assumed, the pressure drag coefficient can be expressed as

$$C_{D_p} = \sin^2 \Theta_s \left[(1 - C_{p_w}) - \frac{9}{8} \sin^2 \Theta_s \right] \quad (5.37)$$

The pressure coefficient in the wake and the separation angle will be obtained from existing experimental data.

Taneda⁽²⁸⁾ of Kyushu University in Japan, experimenting with a sphere moving in a water tank, was able to measure photographically the position of separation. For Reynolds numbers in excess of 80 the angle of separation, as measured from the rear stagnation point, varied linearly with the logarithm of the Reynolds number. The data can be represented by the following empirical formula

$$\Theta_s = 180^\circ - 35 \log_{10} \frac{Re}{3.26} \quad (5.38)$$

Taneda's data, however, extend only to a Reynolds number of 300.

Garner et al.⁽²⁹⁾ report that the separation angle reaches a maximum value of 104° at a Reynolds number of approximately 450 and remains at this position for Reynolds numbers well above 1000. Assuming the empirical formula describing Taneda's experimental results is valid for Reynolds numbers above 300, a separation angle of 104° is obtained when $Re \approx 490$. This value is reasonably near that reported by Garner et al. so the following relationships will be used for the variation of the separation angle with Reynolds number

$$\begin{aligned} \Theta_s^\circ &= 180 - 35 \log_{10} \frac{Re}{3.26} & 80 < Re \leq 490 & \quad (5.39) \\ \Theta_s^\circ &= 104^\circ & Re > 490 & \end{aligned}$$

The experimental work reported by Ermisch⁽³⁰⁾ indicates the average pressure coefficient in the wake region of a sphere is approximately -0.4. Ermisch's results extend to Reynolds numbers as low as 750.

Substituting $C_{pw} = -0.4$ and separation angle variations given above into Equations (5.36) and (5.37) and summing the results gives the drag coefficient versus Reynolds number for a sphere. The results for the three shear distributions are plotted in Figure 18. In addition, the standard drag coefficient curve for a sphere, as found by numerous experiments, is shown for reference. Cases I and II fit the standard curve quite well for the regime of interest. However, Case III gives a better, although slightly higher, representation of the experimental results found in the present study.

The shear distribution corresponding to Case III will be used in the analyses to follow for two reasons:

- 1) best agreement with more accurate analysis near stagnation point, as found above, for the skin friction coefficient.
- 2) turbulence intensities of 5% can occur near the rocket nozzle⁽³¹⁾ which would tend to make a fuller velocity profile more likely.

5.5 Rate of Evaporation of a Spherical Drop in Steady Flow

For steady flow, Equation (5.17) reduces to

$$\frac{1}{\sin \theta} \frac{\partial}{\partial \theta} \sin \theta \int_0^{S_p} \rho u_{\theta} (c_e - c) dq = a (\rho u_r)_s (c_e - 1) \quad (5.40)$$

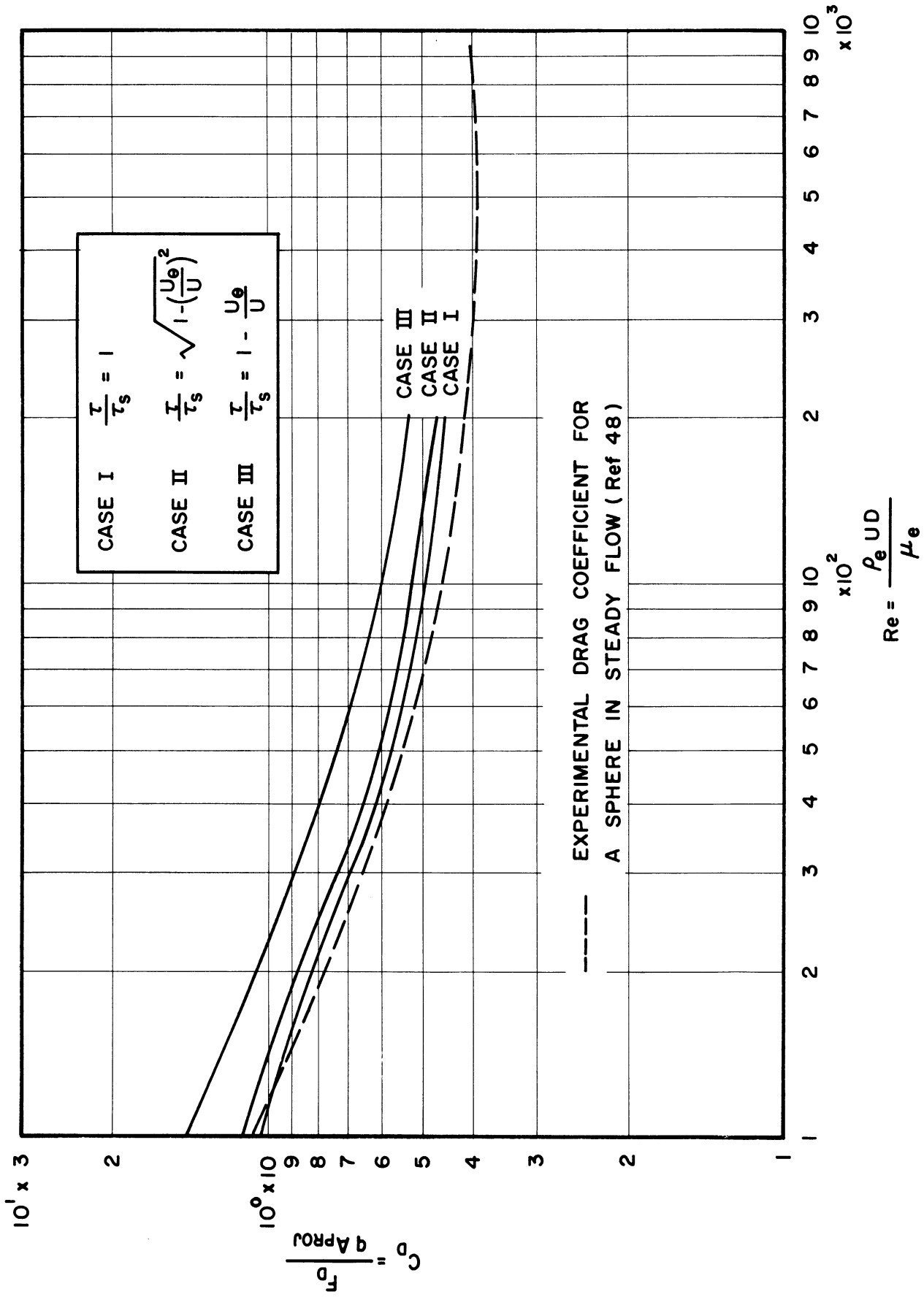


Figure 18. Drag Coefficients vs. Reynolds Number for Three Assumptions of Shear Distributions.

where, for convenience, the subscripts have been dropped on the c's since they now represent the mass fraction of the particle's vapor.

In accordance with Covert's technique⁽²⁵⁾, assume that the velocity and concentration profiles vary linearly with the radial distance from the surface.

$$u_{\theta} = h q \quad (5.41a)$$

$$c = c_s + l q \quad (5.41b)$$

The constants, h and l, are then chosen to satisfy the conditions at the edge of the boundary layers, or

$$h = \frac{U_e}{\delta_v} \quad l = \frac{c_e - c_s}{\delta_D} \quad (5.42)$$

However, the assumption of linear profiles necessitates

$$\frac{\partial u}{\partial q} = \frac{U_e}{\delta_v} = \frac{\tau_s}{\mu_s} \quad (5.43)$$

$$\frac{\partial (c - c_s)}{\partial q} = \frac{\partial c}{\partial r} \Big|_s = \frac{c_e - c_s}{\delta_D} \quad (5.44)$$

Equations (5.41) become

$$\begin{aligned} u_{\theta} &= \frac{\tau_s}{\mu_s} q \\ c - c_s &= \frac{\partial c}{\partial r} \Big|_s q \end{aligned} \quad (5.45)$$

Employing Equations (5.13) and (5.45), the mass fraction "c-c_s" is expressible as

$$c - c_s = \frac{(\rho u_r)_s}{\rho_s D_s} (c_s - 1) \frac{\mu_s}{\tau_s} u_{\theta} \quad (5.46)$$

and rearranging for u_θ yields

$$u_\theta = \frac{(c-c_s)}{(\rho u_r)_s} \frac{\gamma_s}{Sc_s} \frac{1}{(c_s-1)} \quad (5.47)$$

where $Sc_s =$ Schmidt number at the surface ($Sc_s = \frac{\mu_s}{\rho_s D_s}$). This expression is only valid for $\delta_D \leq \delta_V$. If $\delta_D > \delta_V$, the above expression is only valid up to the edge of the velocity boundary layer and beyond this point $u_\theta = U_e$ must be used. The present study, however, will only consider the former case and is consequently restricted to problems in which the Schmidt number is the order of one or greater.

Upon substitution of Equations (5.42) and (5.43) into the integral of Equation (5.40), it becomes

$$\int_0^{\delta_D} \rho u_\theta (c_e - c) dq = \frac{\gamma_s \rho_s \mu_s (\Delta c)^3}{Sc_s^2 (\rho u_r)_s^2 (1-c_s)} \int_0^1 \left(\frac{\rho}{\rho_s}\right) \gamma (1-\gamma) d\gamma \quad (5.48)$$

where $\gamma = \frac{c-c_s}{c_e-c_s}$

$\Delta c = c_e - c_s$

In the case of evaporation at room temperature of liquids such as most hydrocarbon fuels the vapor concentration at the surface is small and consequently less in the diffusion boundary layer. Therefore it is reasonable to assume that the density of the mixture is that of the environmental medium. Equation (5.40) then simplifies to

$$\frac{d}{d\theta} \frac{\sin \theta}{6} \frac{\gamma_s \rho_s \mu_s (\Delta c)^3}{Sc_s^2 (\rho u_r)_s^2 (1-c_s)^2} = a (\rho u_r)_s (c_e - 1) \sin \theta \quad (5.49)$$

Integrating this expression and non-dimensionalizing the mass flux at the surface by dividing by the mass flux in the free steam gives

$$\frac{(\rho u_r)_s}{\rho_e U} = \left(\frac{1}{\gamma}\right)^{1/3} \frac{1}{\sqrt{Re}} \frac{1}{Sc_s^{2/3}} \frac{\Delta c}{(1-c_s)^{2/3} (c_e-1)^{1/3}} \frac{\sin^{1/2} \theta [C_F \sqrt{Re}(\theta)]^{1/2}}{\left\{ \int_0^\theta \sin^{3/2} \phi [C_F \sqrt{Re}(\phi)]^{1/2} d\phi \right\}^{1/3}} \quad (5.50)$$

The non-dimensional Sherwood number, sometimes known as the Nusselt diffusion number, is defined as⁽³²⁾

$$Sh = \frac{L \dot{m}}{\rho D S (c_e - c_s)} \quad (5.51)$$

where \dot{m} = mass flow at surface

S = reference area

L = reference length

However

$$\frac{\dot{m}}{S} = -(\rho u_r)_s$$

and the evaporation rate expressed in terms of the Sherwood number is

$$Sh = \left(\frac{1}{9}\right)^{1/3} \frac{\sqrt{Re} Sc^{1/3}}{(1-c_s)^{2/3} (1-c_e)^{1/3}} \frac{\sin^{1/2} \theta [C_f \sqrt{Re}(\theta)]^{1/2}}{\left\{ \int_0^\theta \sin^{3/2} \phi [C_f \sqrt{Re}(\phi)]^{1/2} d\phi \right\}^{1/3}} \quad (5.52)$$

Frössling⁽³³⁾ in 1938 conducted a series of experiments to determine the evaporation characteristics of particles in convective flow fields. A portion of his experimental work involved finding the variation in evaporation rate over the surface of a naphthalene sphere at various Reynolds numbers from 48 to 1060. Under the conditions at which Frössling performed his experiments, namely atmospheric pressure and a temperature of 20°C., the concentration of naphthalene vapor at the surface is very small ($c_s < 0.001$) and the above equation simplifies to

$$\frac{Sh}{Re^{1/2} Sc^{1/3}} = \left(\frac{1}{9}\right)^{1/3} \frac{\sin^{1/2} \theta [C_f \sqrt{Re}(\theta)]^{1/2}}{\left\{ \int_0^\theta \sin^{3/2} \phi [C_f \sqrt{Re}(\phi)] d\phi \right\}^{1/3}} \quad (5.53)$$

Figure 19 shows both the experimental results of Reference 33 and the results of Equation (5.53) evaluated using the skin friction distribution corresponding to Case III. As can be seen, the agreement is good near the region of the stagnation point but exceeds the experimental values up to the separation point. This may be attributed to the relatively large skin friction as dictated by the particular shear distribution chosen. The evaporation increase beyond the separation point is due to the reverse flow created by the fixed vortex ring in the wake of the sphere.

The overall evaporation rate is obtained by integrating the local evaporation rate over the surface of the sphere. As can be seen from Figure 19, the major portion of the evaporation occurs over the forward hemisphere and is roughly ten times greater than that which occurs in the wake region. Though the theory is not valid in the wake region, the integration may be extended to $\theta = 180^\circ$ since the error introduced will be small. Thus, for the whole particle

$$\begin{aligned}
 Sh &= \frac{Re Sc_s}{2(\Delta c)} \int_0^\pi \frac{(\rho u_r)_s}{(\rho U)_e} \sin \theta d\theta \\
 &= \frac{3}{4} \left(\frac{1}{9}\right)^{1/3} \frac{Re^{1/2} Sc_s^{1/3}}{(1-c_s)^{2/3} (1-c_e)^{1/3}} \left\{ \int_0^\pi \sin^{3/2} \phi [C_f \sqrt{Re}(\phi)] d\phi \right\}^{2/3} \quad (5.54)
 \end{aligned}$$

Using the skin friction distribution corresponding to Case III, this equation reduces to

$$Sh = 0.728 \frac{Re^{1/2} Sc_s^{1/3}}{(1-c_s)^{2/3} (1-c_e)^{1/3}} \quad (5.55)$$

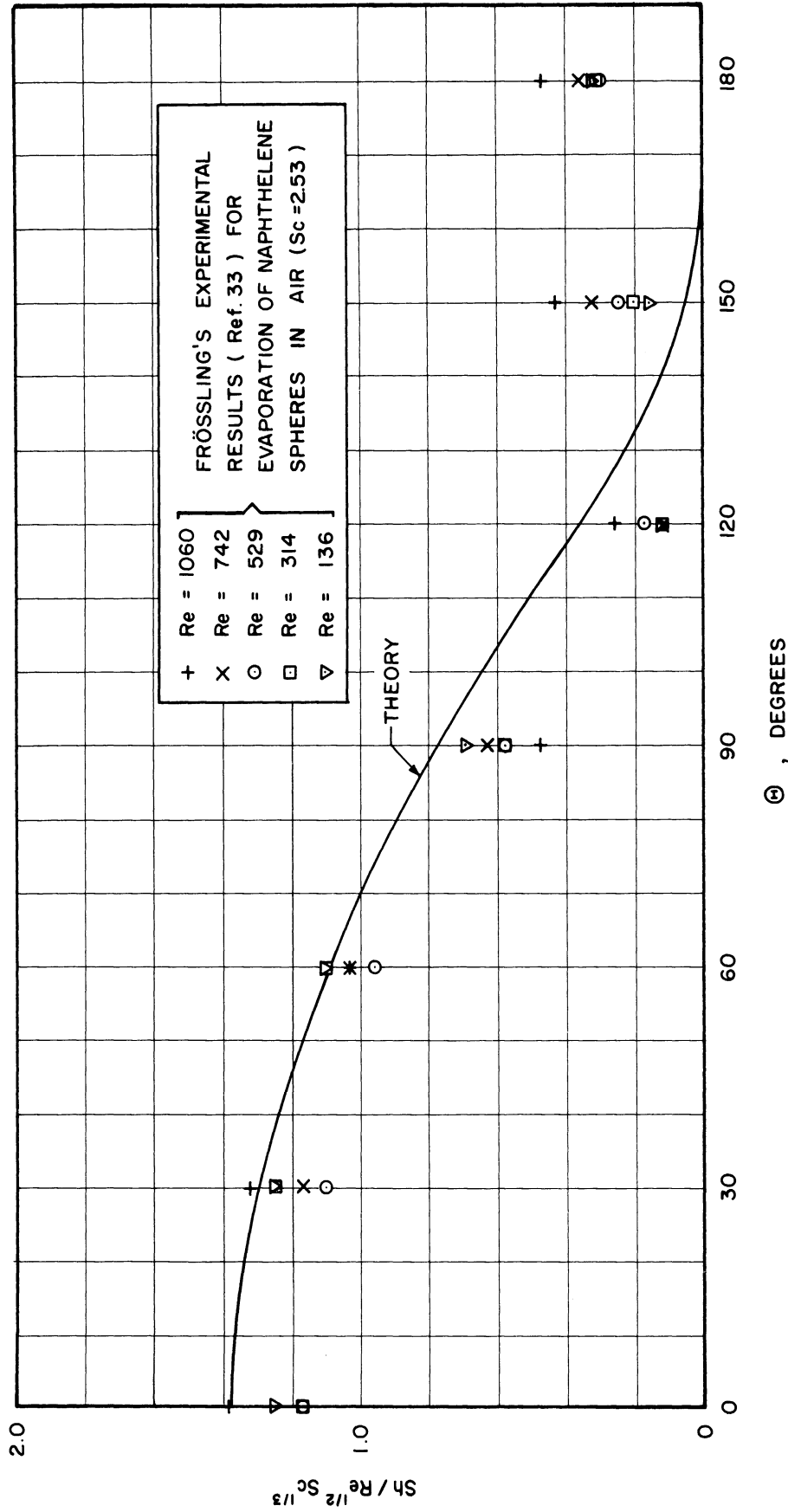


Figure 19. Variation of Evaporation Rate on Surface of Liquid Sphere.

If c_s and c_e are small compared to one, the expression further reduces to

$$Sh = 0.728 Re^{1/2} Sc^{1/3} \quad (5.56)$$

Frössling⁽³³⁾ found experimentally a value of 0.552 for the coefficient in the above equation. However, other experimenters have found that the coefficient may be as large as 0.95⁽²⁹⁾ so the theoretical value found above seems most reasonable. The spread in coefficients found experimentally is most probably due to turbulence effects.

5.6 Effect of Evaporation on Drag Coefficient

The effect of evaporation appears in the momentum Equation (5.23) by the inclusion of the radial mass flux term at the surface. Evaluating the integrals by the method of Section 5.3 and substituting into the momentum equation gives

$$B \frac{\rho_e \mu_e U_e^2}{\gamma_s} \frac{dU_e}{d\theta} + \frac{A}{\sin \theta} \frac{d \sin \theta}{d\theta} \frac{\rho_e \mu_e U_e^3}{\gamma_s} - a \frac{(\rho u_r)_s}{(\rho U)_e} \rho_e U_e^2 = a \gamma_s \quad (5.57)$$

Rewriting this equation assuming the classical free stream velocity distribution yields

$$\frac{d\zeta^2}{d\theta} + 2 \left(1 + \frac{B}{A}\right) \frac{\cos \theta}{\sin \theta} \zeta^2 - \frac{(\rho u_r)_s \sqrt{Re}}{(\rho U)_e} \frac{\sin \theta}{2A} \zeta = \frac{3 \sin^3 \theta}{8A} \quad (5.58)$$

where

$$\zeta = \frac{9}{4} \frac{\sin^3 \theta}{C_f \sqrt{Re}}$$

The equation may now be identified as an ordinary non-linear differential equation.

Substituting the results of the previous section for the mass flux at the surface into Equation (5.58) results in the rather complex integrodifferential equation

$$\frac{d\bar{z}^2}{d\theta} + 2\left(1 + \frac{B}{A}\right) \frac{\cos\theta}{\sin\theta} \bar{z}^2 - \frac{\left(\frac{3}{2}\right)^{2/3} \sin^3\theta \bar{z}^{1/2} \Lambda}{2A \left[\int_0^\theta \frac{\sin^3\lambda}{\bar{z}^{1/2}} d\lambda \right]^{1/3}} = \frac{3}{8A} \sin^3\theta \quad (5.59)$$

where

$$\Lambda = \left(\frac{1}{9}\right)^{1/3} \frac{\Delta C}{(1-c_s)^{2/3} (1-c_e)^{1/3} S c_s^{2/3}}$$

Since no closed form solution is immediately evident for this particular equation a perturbation solution is attempted. Assume

$$\bar{z} = \bar{z}_0 (1 + \epsilon) \quad (\epsilon \ll 1) \quad (5.60)$$

where \bar{z}_0 is solution of the equation for no mass flux at the surface. Substituting this expression for \bar{z} in Equation (5.59) and canceling the portion of the equation which \bar{z}_0 satisfies gives

$$\begin{aligned} \frac{d\bar{z}_0^2 (2\epsilon + \epsilon^2)}{d\theta} + 2\left(1 + \frac{B}{A}\right) \frac{\cos\theta}{\sin\theta} \bar{z}_0^2 (2\epsilon + \epsilon^2) \\ = \frac{\left(\frac{3}{2}\right)^{2/3} \sin^3\theta \bar{z}_0^{1/2} \left[1 + \frac{\epsilon}{2} \dots\right]}{2A \left[\int_0^\theta \frac{\sin^3\lambda}{\bar{z}_0^2} \left[1 - \frac{\epsilon}{2} \dots\right] d\lambda \right]^{1/3}} \end{aligned} \quad (5.61')$$

However

$$\int_0^\theta \frac{\sin^3\lambda}{\bar{z}_0^{1/2}} \epsilon d\lambda \leq \epsilon_m(\theta) \int_0^\theta \frac{\sin^3\lambda}{\bar{z}_0^2} d\lambda$$

where $\epsilon_m(\theta)$ is the largest value of ϵ in the range of integration. Thus:

$$\int_0^\theta \frac{\sin^3\lambda}{\bar{z}_0^2} d\lambda = [1 + O(\epsilon)] \int_0^\theta \frac{\sin^3\lambda}{\bar{z}_0^2} d\lambda$$

Exploiting the assumption that $\epsilon \ll 1$ Equation (5.61') may be written

$$\begin{aligned} \frac{d}{d\theta} [\bar{z}_0^2 (2\epsilon + \epsilon^2)] + 2 \left(1 + \frac{B}{A}\right) \frac{\cos \theta}{\sin \theta} \bar{z}_0^2 (2\epsilon + \epsilon^2) \\ = \frac{\left(\frac{3}{2}\right)^{2/3} \sin^3 \theta \bar{z}_0^{1/2} [1 + o(\epsilon)]}{2A \left[\int_0^\theta \frac{\sin^3 \lambda}{\bar{z}_0^{1/2}} d\lambda \right]^{1/3}} \end{aligned}$$

Neglecting the higher order term yields

$$\frac{d(\bar{z}_0^2 \epsilon)}{d\theta} + 2 \left(1 + \frac{B}{A}\right) \frac{\cos \theta}{\sin \theta} (\bar{z}_0^2 \epsilon) = \frac{9\Lambda}{16A} \frac{\sin^{9/2} \theta [C_F \sqrt{Re'}(\theta)]_0^{-1/2}}{\left\{ \int_0^\theta \sin^{3/2} \phi [C_F \sqrt{Re'}(\phi)]_0^{1/2} d\phi \right\}^{1/3}} \quad (5.61)$$

Using the values of A and B corresponding to Case III results in the expression

$$\frac{d(\bar{z}_0^2 \epsilon)}{d\theta} + 6 \frac{\cos \theta}{\sin \theta} (\bar{z}_0^2 \epsilon) = \frac{9}{8} \Lambda Q(\theta) \quad (5.62)$$

where

$$Q(\theta) = \frac{\sin^{9/2} \theta [C_F \sqrt{Re'}(\theta)]_0^{-1/2}}{\left\{ \int_0^\theta \sin^{3/2} \phi [C_F \sqrt{Re'}(\phi)]_0^{1/2} d\phi \right\}^{1/3}}$$

Solving Equation (5.62) for $\bar{z}_0^2 \epsilon$ yields

$$\bar{z}_0^2 \epsilon = \frac{9}{8} \frac{\Lambda}{\sin^6 \theta} \int_0^\theta \sin^6 \phi Q(\phi) d\phi \quad (5.63)$$

However, referring back to Equation (5.35), the \bar{z}_0 for this particular case can be written

$$\bar{z}_0 = \frac{\left(\frac{3}{2}\right)^{1/2}}{\sqrt{2} \sin^3 \theta} \left[\int_0^\theta \sin^9 \phi d\phi \right]^{1/2}$$

and dividing Equation (6.63) by the square of \bar{f} , gives

$$\epsilon = \frac{3}{2} \Lambda \frac{\int_0^\theta \sin^6 \phi Q(\phi) d\phi}{\int_0^\theta \sin^7 \phi d\phi} \quad (5.64)$$

The results of evaluating the above equation appear in Figure 20 as

$\frac{\epsilon (1-c_s)^{2/3} (c_e-1)^{1/3} Sc_s^{2/3}}{\Delta c}$ versus the angle measured from the forward stagnation point. The values increase monotonically with θ and reach a maximum value of 0.282. At the separation point for Reynolds numbers greater than 450 ($\theta_s = 104^\circ$), the abscissa is approximately 0.28. Thus, it is possible to write

$$\epsilon < \frac{0.28 \Delta c}{Sc_s^{2/3} (1-c_s)^{2/3} (c_e-1)^{1/3}}$$

or

$$\frac{C_{f0}}{C_f} < \frac{1 + 0.28 \Delta c}{Sc_s^{2/3} (1-c_s)^{2/3} (c_e-1)^{1/3}} \quad (Sc \geq 1) \quad (5.65)$$

In order to appreciate the magnitude of the correction factor, consider the case of an evaporating ethanol droplet in air at 20°C. and atmospheric pressure. Assume the mass fraction of ethanol vapor in the free stream is zero ($c_e = 0$). Under these ambient conditions the Schmidt number for ethanol vapor in air is 1.36 (34). The mass fraction of vapor at the surface can be found using the expression

$$c_s = \frac{1}{1 + \frac{P}{P_v} \frac{\bar{M}_a}{\bar{M}_v} \left(1 + \frac{P_v}{P}\right)} \quad (5.66)$$

* Assuming equilibrium conditions at the surface.

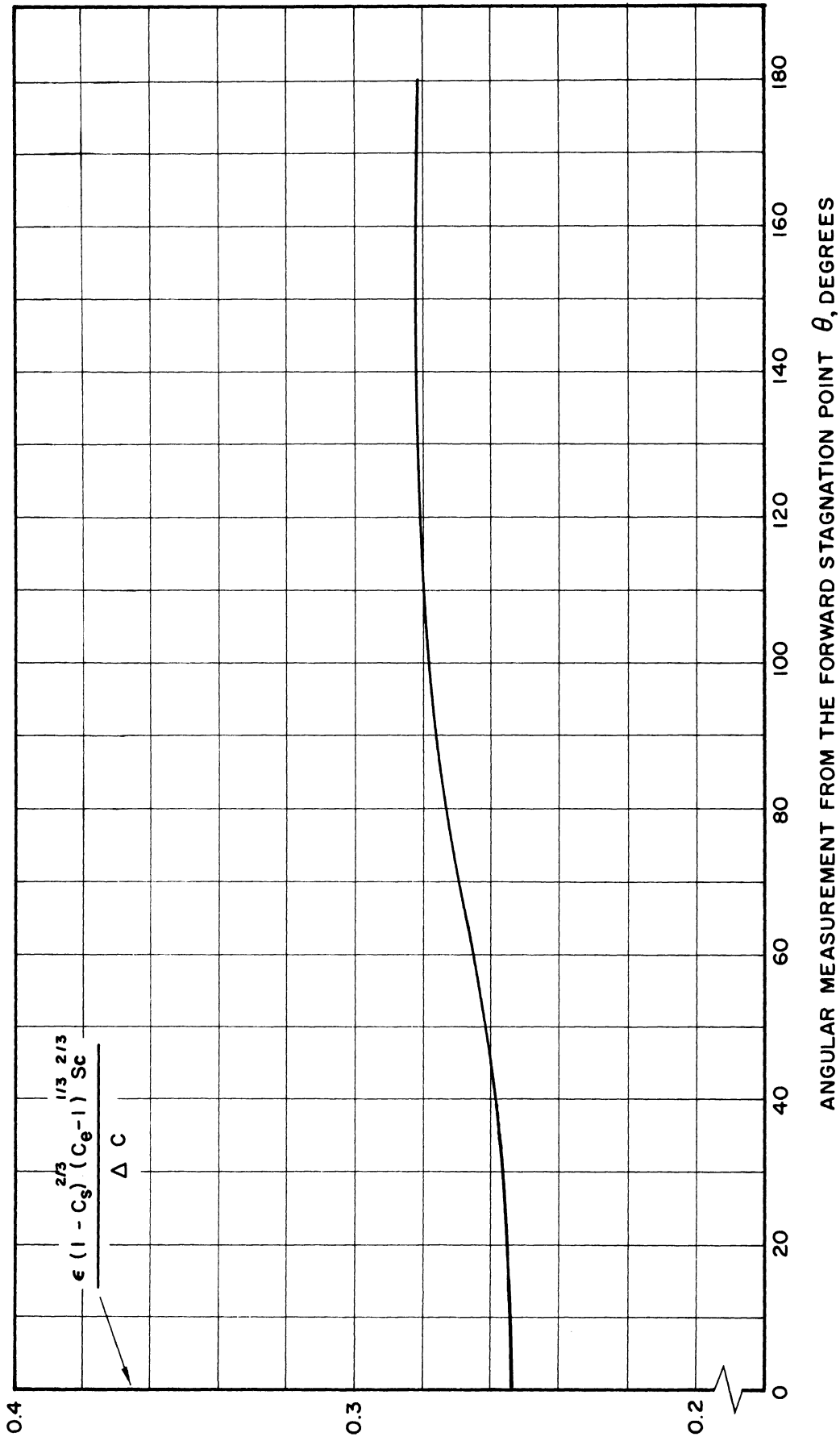


Figure 20. Correction Factor for the Skin Friction Coefficient of an Evaporating Drop.

where \bar{M}_a and \bar{M}_v are the molecular weights of the air and vapor respectively while p_v is the partial pressure of the vapor. For ethanol at 20°C and atmospheric pressure, $\frac{p_v}{p} \ll 1$ and it is possible to write

$$C_s = \frac{p_v}{p} \frac{\bar{M}_v}{\bar{M}_a} = 0.092$$

using the values found in Reference 35. Substituting the above values into Equation (5.65) results in

$$\frac{C_{f_0}}{C_f} < 1 + 0.0222$$

Thus, the skin friction will be decreased by less than 2.22 percent.

In the conventional evaporation problem the vapor concentration at the surface is small and thus for the large majority of cases Equation (5.65) simplifies to

$$\frac{C_{f_0}}{C_f} < 1 + \frac{0.28 C_s}{Sc^{2/3}} \quad (5.67)$$

and the change in skin friction due to evaporation is small.

The probable effect of evaporation in the wake region will be a decrease in base pressure on the sphere and a consequent increase in the pressure drag coefficient. A very crude analysis can be made if the following assumptions are applied:

- 1) pressure in the wake negligibly effected by evaporation
- 2) radial component of momentum is zero a short distance from the surface.

Using the difference equation formulation of the one dimensional momentum equation and applying it in the radial direction between the surface and where the radial component of momentum is zero gives

$$p_s - p_w = -(\rho u_r^2)_s \quad (5.68)$$

where p_s = pressure on the surface

p_w = pressure in the wake

In terms of pressure coefficients, Equation (5.68) becomes

$$C_{p_s} = \frac{p_s - p_e}{\rho_e U^2} = C_{p_w} - 2 \frac{\rho_e}{\rho_s} \left[\frac{(\rho u_r)_s}{\rho_e U} \right]^2 \quad (5.69)$$

where C_{p_s} is the pressure coefficient to be used in pressure drag calculations and C_{p_w} when there is no evaporation. Thus $\frac{2\rho_e}{\rho_s} \left[\frac{(\rho u_r)_s}{\rho_e U} \right]^2$ represents a correction factor to account for evaporation.

The ratio of mass flux from the surface to that in the free stream may be expressed in terms of non-dimensional numbers as follows

$$\frac{(\rho u_r)_s}{\rho_e U} = \frac{\Delta c}{Re} \frac{Sh}{Sc} \quad (5.70)$$

or

$$\frac{(\rho u_r)_s}{\rho_e U} = \frac{Sh}{Re^{1/2} Sc^{1/3}} \frac{\Delta c}{Re^{1/2} Sc^{2/3}} \quad (5.71)$$

From Frössling's data it appears that

$$\frac{Sh}{Re^{1/2} Sc^{1/3}} < 0.5 \quad (5.72)$$

so it is possible to write

$$\left[\frac{(\rho u_r)_s}{\rho_e U} \right]^2 < \frac{0.25 c_s^2}{Re Sc^{4/3}} \quad (5.73)$$

if the concentration of vapor in the free stream is zero and the mass ratio of the vapor at the surface is small.

Referring once more to example of the ethanol droplet, it is possible to assume $\rho_e/\rho_s \doteq 1$ and the correction factor becomes

$$2 \left[\frac{(\rho u_r)_s}{\rho_e U} \right]^2 < \frac{0.00138}{Re}$$

which is very small in magnitude compared to the pressure coefficient in the wake and can be neglected. Consequently by use of the assumptions stated above, the effect of evaporation on the pressure drag is negligible.

Since evaporation fails to influence either the pressure or skin friction drag appreciably, the overall drag coefficient will not be altered significantly. This conclusion should be valid for the conventional evaporation problems when the mass fraction of the vapor at the surface is small. The experimental evidence of Reference 10 indicates the above conclusion is valid.

5.7 The Effect of Burning on Drag Coefficient

Burning will reduce the skin friction coefficient in the same way as evaporation, that is; there will be a radial mass flux from the surface.

A model must be chosen to represent the burning particle. A spherical particle will be assumed with all burning taking place on the surface and no chemical reactions in the boundary layer. In addition, it will be assumed that the temperature ratio between the particle surface and free stream remains invariant with respect to time and surface coordinates. Figure 21 illustrates the model to be chosen and a representative temperature distribution. The model of the burning particle is essentially a spherical surface of fluid sources creating an outward mass flux. The effect of the decrease in size of the particle with time will be neglected.

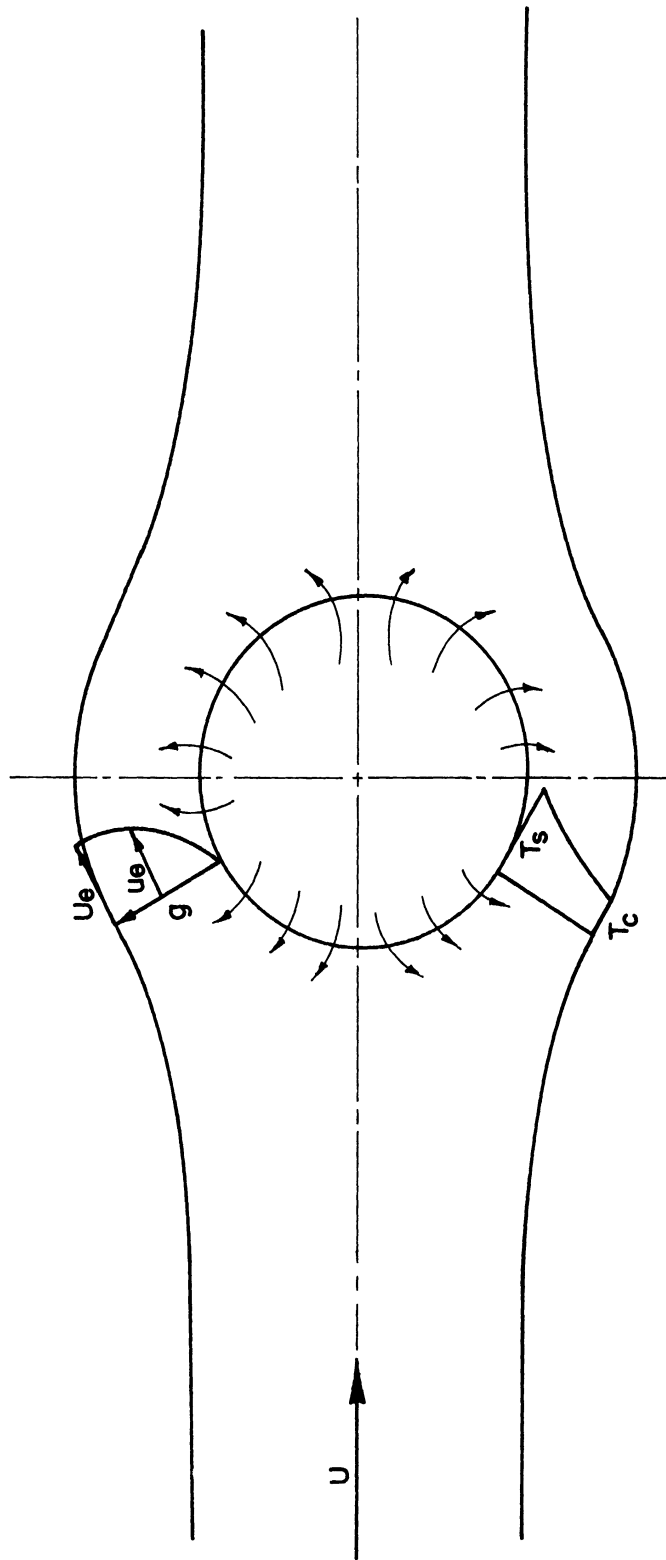


Figure 21. Schematic Diagram of a Burning Particle.

In addition it will be assumed that the burning rate is constant over the whole surface. This assumption is in accordance with the present experiment since for velocities less than 500 feet per second, the effects of erosive burning are negligible. (36)

The temperature variation through the boundary layer necessitates a recalculation of the displacement and momentum thicknesses. Assume the temperature and velocity distribution are the same, that is

$$\frac{T_s - T}{T_s - T_e} = \eta = \frac{u}{U_e} \quad (5.74)$$

where T_s = temperature at the surface

T_e = temperature in the free stream.

This relationship is exact for a flat plate at zero angle of attack in parallel flow at low velocities provided the Prandtl number is unity. Although these conditions are not identical with those of the present problem, the assumption made should serve as a reasonable approximation.

The gas in the boundary layer is composed of the environmental gas as well as the products of combustion. To simplify the analysis it will be assumed that the mixture of gases have a molecular weight and viscosity variation with temperature equivalent to that of air. As found in Kennard⁽³⁷⁾ the viscosity variation of air with temperature can best be approximated by

$$\frac{\mu}{\mu_e} = \left(\frac{T}{T_e}\right)^{0.79} \quad (5.75)$$

to temperatures of about 300° C. For the present analysis an exponent of 0.8 will be used.

The assumption of constant pressure through the boundary layer together with invariance of molecular weight makes it possible to write

$$\frac{p}{p_e} = \frac{T_e}{T} \quad (5.76a)$$

Thus,

$$\frac{\rho\mu}{\rho_e\mu_e} = \left(\frac{T_e}{T}\right)^{0.2} \quad (5.76b)$$

Rewriting Equation (5.74), the temperature variation as a function of η has the form

$$\frac{T}{T_e} = [\bar{T} - \eta(\bar{T} - 1)] \quad (5.77)$$

where $\bar{T} = T_s/T_e$. Using the shear distribution for Case III, namely

$$\frac{\tau}{\tau_s} = 1 - \eta$$

the particular constants A and B introduced in Section 5.3 become

$$A = \frac{\bar{T}^{1.8} - 1.8(\bar{T} - 1) - 1}{1.44(\bar{T} - 1)^2} \quad (5.78a)$$

$$B = \frac{\bar{T}^{1.8} - \bar{T}}{0.8(\bar{T} - 1)} \quad (5.78b)$$

The values of A and B are plotted in Figure 22 versus \bar{T} . It is observed that A is a relatively weak function of \bar{T} while B increases monotonically. Thus, the quotient B/A, which is most important in the momentum equation, can be expected to be quite different for the burning particle.

Reference 36 suggests a reasonable value for the surface temperature of a burning double base propellant is about 300°C. For an atmosphere at room temperature, such as the case of experimental study, the

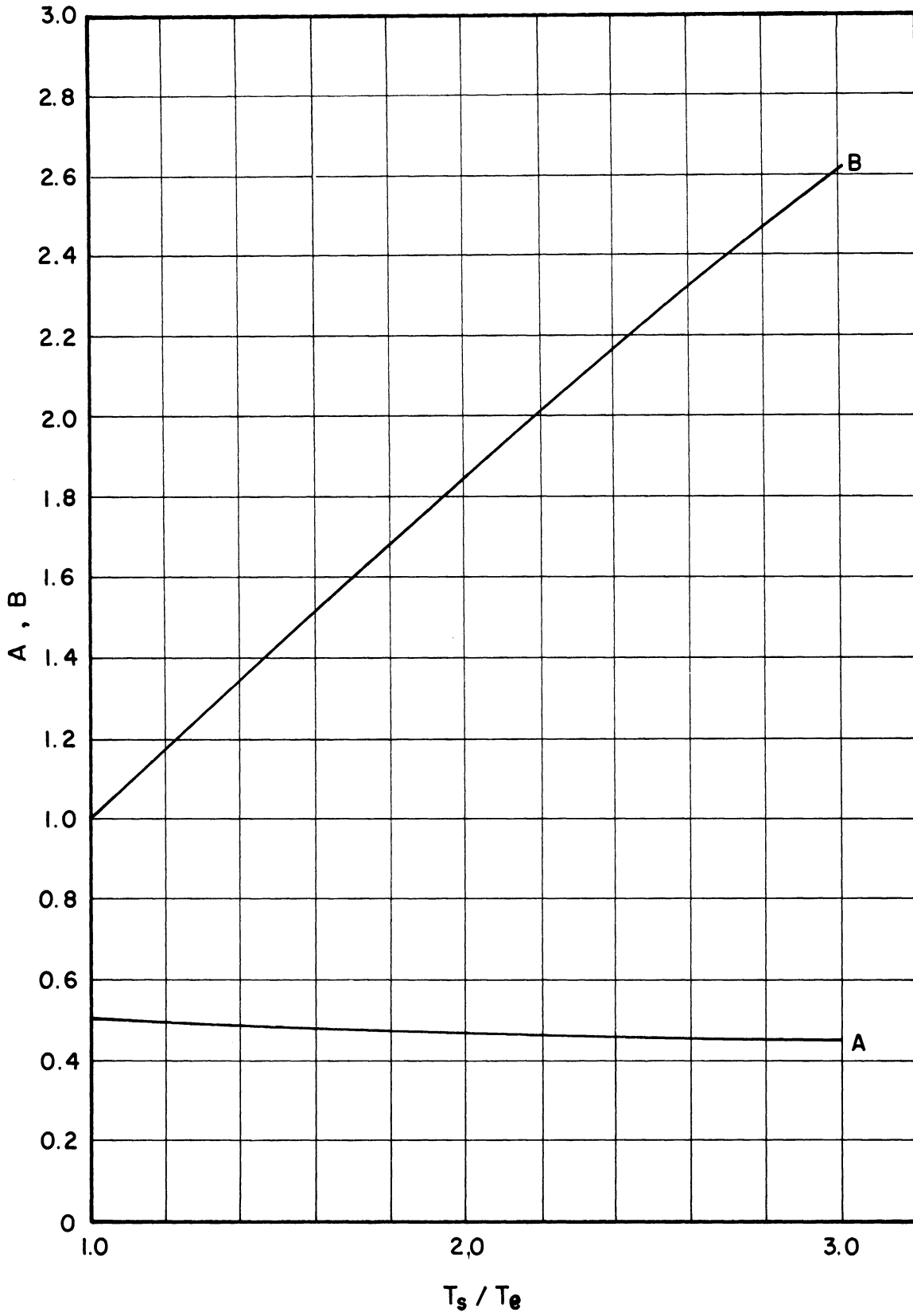


Figure 22. Variation of "A" and "B" with Temperature.

value of \bar{T} would be approximately two. Substituting this value into Equations(5.78a) and (5.78b) yields

$$A = 0.472$$

$$B = 1.85$$

and

$$\frac{B}{A} = 3.96$$

For simplification in evaluating the ensuing equations a value of 4 will be selected for B/A while the value of 0.5 will be retained for A.

For steady flow in a non-accelerating system, Equation (5.23) reduces to

$$\frac{B}{a} \frac{dU_e}{d\theta} \frac{\rho_e U_e \mu_e}{\tau_s} + \frac{A}{a \sin \theta} \frac{d \sin \theta}{d\theta} \frac{\rho_e U_e \mu_e}{\tau_s} - \frac{(\rho u_r)_s}{(\rho U)_e} \rho_e U_e^2 = \tau_s \quad (5.57)$$

Assuming once again the classical incompressible velocity distribution for the external flow and substituting the appropriate values for A and B gives the following non-linear ordinary differential equation

$$\frac{d\bar{z}^2}{d\theta} + 10 \frac{\cos \theta}{\sin \theta} \bar{z}^2 = f \sqrt{Re} \bar{z} \sin \theta + \frac{3}{4} \sin^3 \theta \quad (5.79)$$

where

$$\bar{z} = \frac{9}{4} \frac{\sin^3 \theta}{C_f \sqrt{Re}}$$

and
$$f = \frac{(\rho u_r)_s}{\rho_e U}$$

This equation may be rewritten as

$$\frac{d}{d\theta} \left(\frac{3}{4} \sin^4 \theta \right) = f \sqrt{Re} \sin^2 \theta + \frac{3}{4} \sin^3 \theta \quad (5.80)$$

Let

$$\beta = \frac{3}{4} \frac{\sin^4 \theta}{C_f \sqrt{Re}} = \frac{9}{4} \frac{\sin^4 \theta}{C_f \sqrt{Re}}$$

and substituting into the above equation gives

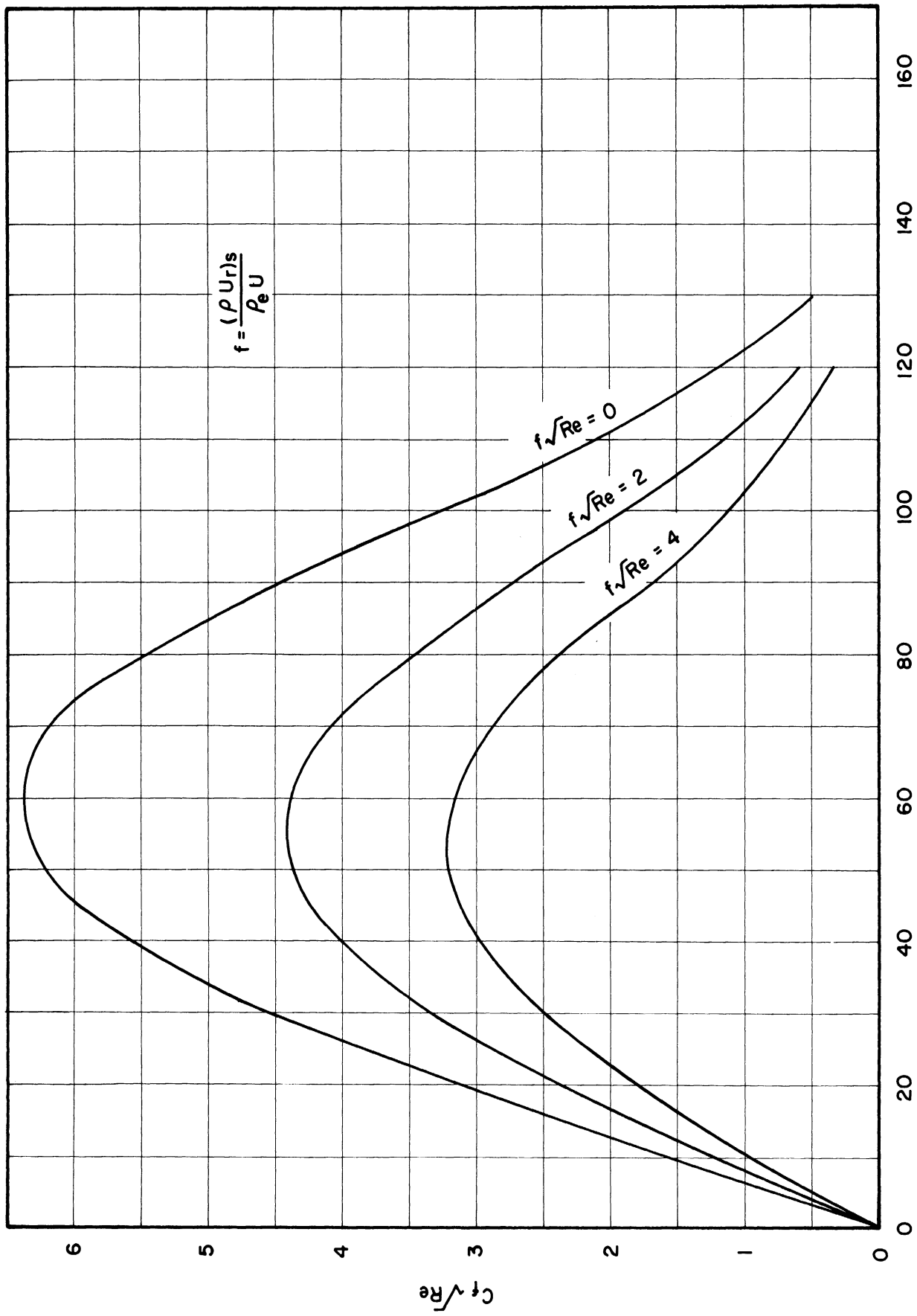
$$\sin \theta \frac{d\beta^2}{d\theta} + 14 \cos \theta \beta^2 = f \sqrt{Re} \beta + \frac{3}{4} \quad (5.81)$$

This equation is solved in two steps in Appendix C. For the region near the stagnation point a series expansion of the form:

$$\beta = \sum_{j=0}^{\infty} A_j \frac{\theta^j}{j!}$$

is assumed. The results of this solution then provide a starting point for the Adams method⁽³⁸⁾ of numerical integration. The solution to the equation for $C_f \sqrt{Re}$ is shown in Figure 23 for three values of $f \sqrt{Re}$; namely, 0, 2, and 4.

The effect of burning on the wake region is subject to discussion. If burning occurs in the wake region, the increase in pressure due to burning will tend to reduce the drag coefficient since the pressure coefficient in the wake will be increased. On the other hand, if the assumption is made that burning occurs on the particle surface only, the problem will reduce to that studied earlier for evaporation and the drag coefficient will be larger. To be consistent with the postulates made above as to the model of a burning particle, the latter case will be assumed. This appears to be consistent with experimental photographs in which burning



θ° , ANGULAR MEASUREMENT FROM FORWARD STAGNATION POINT

Figure 23. Skin Friction Distribution Over Surface of Burning Sphere.

could not be detected in the wake. Thus, from Equation (5.69) above, the pressure coefficient in the wake due to burning would be

$$C_{p_s} = C_{p_w} - 2 \frac{\rho_e}{\rho_s} \left[\frac{(\int u_r)_s}{\rho_e U} \right]^2 \quad (5.69)$$

Burning will also effect the separation angle and must be accounted for in order to determine the pressure drag. From the Karman-Polhausen integral technique⁽³⁹⁾ for boundary layers, in which a fourth degree polynomial is used to describe the velocity distribution, it is found that separation will occur when

$$\bar{\Lambda} = \frac{dP}{dx} \frac{\delta^2}{\mu_e U_e} = -12 \quad (5.82)$$

where $\bar{\Lambda}$ is sometimes called the "shape factor". Also it is possible to show, after applying boundary conditions to the assumed distribution, that

$$\frac{\delta^*}{\delta} = h(\bar{\Lambda}) \quad \frac{\Theta}{\delta} = \kappa(\bar{\Lambda}) \quad (5.83)$$

where δ^* and Θ are the displacement and momentum thicknesses respectively. Thus at separation:

$$\frac{\delta^*}{\delta} = N \quad \frac{\Theta}{\delta} = M \quad (5.84)$$

where N and M are some numerical constants. At separation

$$-\frac{dP}{dx} \frac{\delta^2 N M}{\mu_e U_e} = -\frac{1}{a} \frac{dP}{d\Theta} \frac{\delta^* \Theta}{\mu_e U_e} = Q \quad (5.85)$$

where Q is a new constant. Assuming once again the classical free stream velocity distribution and substituting the values for δ^* and Θ from Section 5.3 gives

$$Q' = \frac{AB \cos \theta \sin^2 \theta}{Re C_f^2} \quad (Q' = \text{new constant}) \quad (5.86)$$

at the separation point. Taking the square root, this expression becomes

$$Q'' = \sqrt{Q'} = \sqrt{AB} \frac{|\cos \theta|^{1/2} \sin \theta}{C_f \sqrt{Re}} \quad \theta \geq 90^\circ \quad (5.87)$$

since we have assumed A, B and Q are positive numbers. Since A is considered a constant in the burning and non-burning problem, the equation can further be reduced to

$$\frac{Q''}{\sqrt{A}} = \bar{Q} = \sqrt{B} \frac{|\cos \theta|^{1/2} \sin \theta}{C_f \sqrt{Re}} \quad (5.88)$$

In order to determine the constant \bar{Q} it is assumed that separation occurs at $\theta = 104^\circ$ for case III of the non-burning particle. Substituting the values corresponding to this point gives $\bar{Q} = 0.1725$. Figure 24 illustrates the solution of Equation (5.76) for the three values of $f\sqrt{Re}$ considered.

For Reynold's numbers less than 490 a line for θ_s of the same slope as in the non-burning case is assumed however translated to give the new value at $Re = 490$.

This analysis will not give accurate results but should serve to provide a trend in separation angles. A curve for the variation of the separation angle for the range of Reynolds numbers considered is shown in Figure 25.

The above determined separation angle and modified pressure coefficient together with the skin friction drag yield a drag coefficient for burning particles and is plotted on Figure 26 for values of f

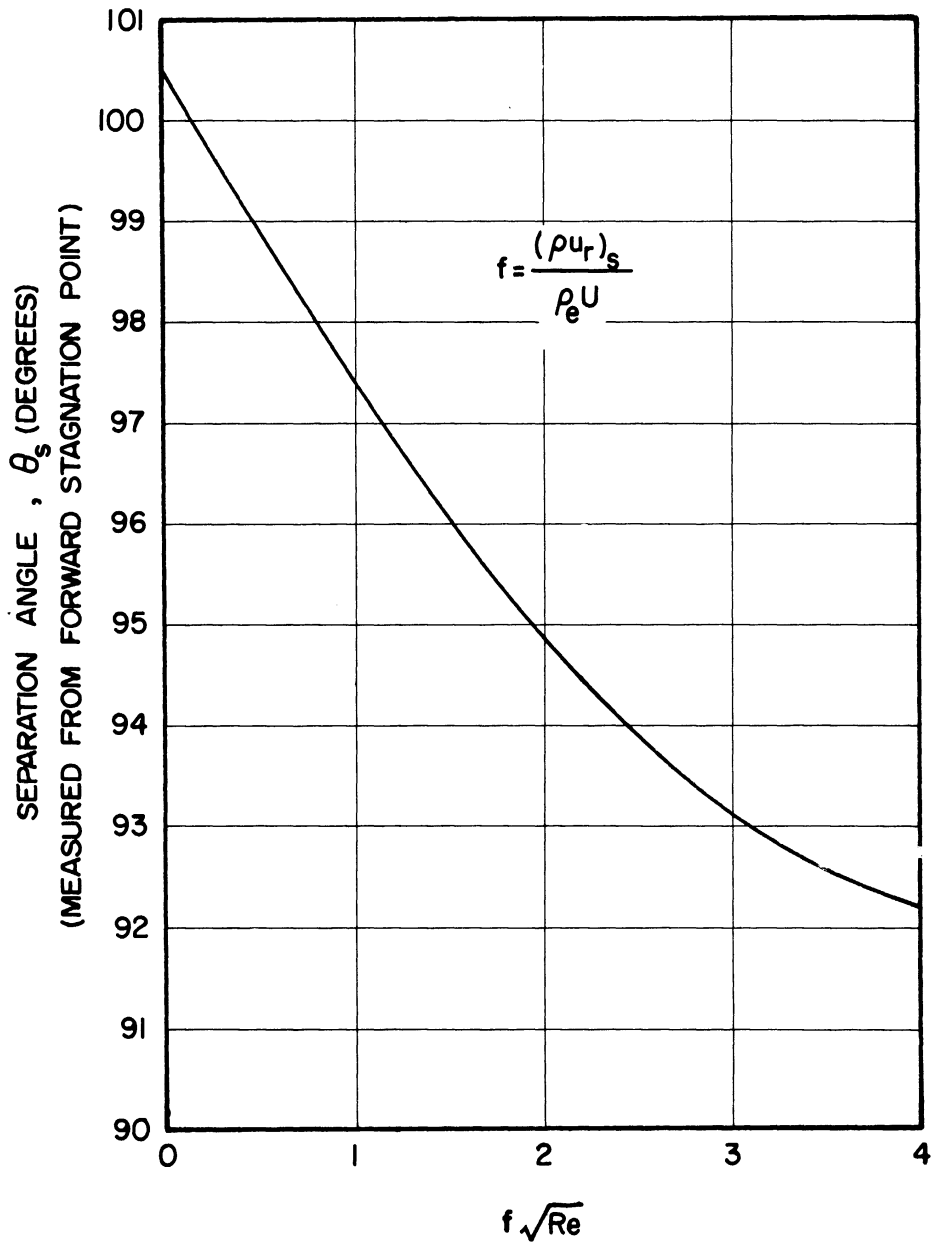


Figure 24. Variation of Separation Angle with Burning Rate for Reynolds Numbers Greater than 490.

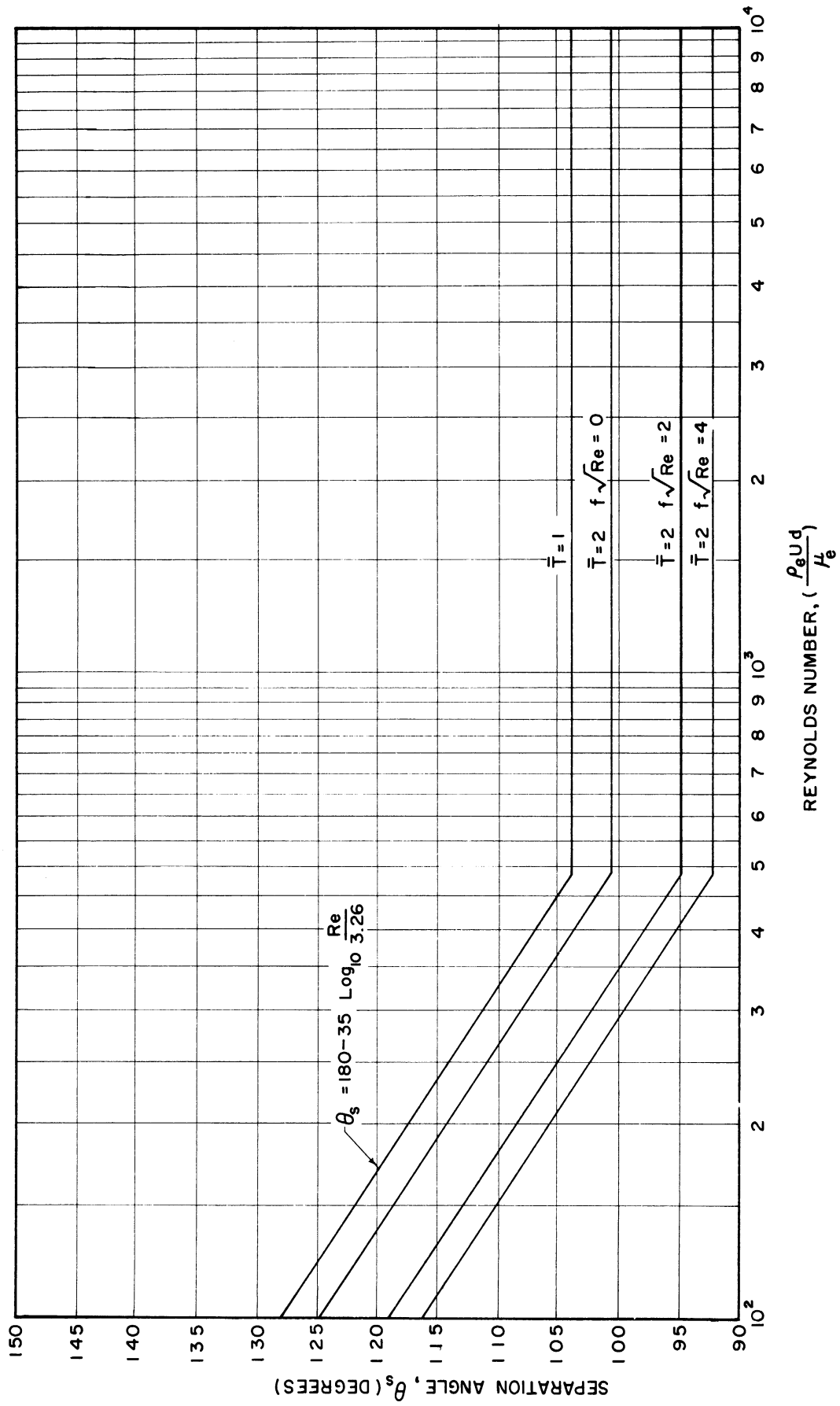


Figure 25. Separation Angle Versus Reynolds Number.

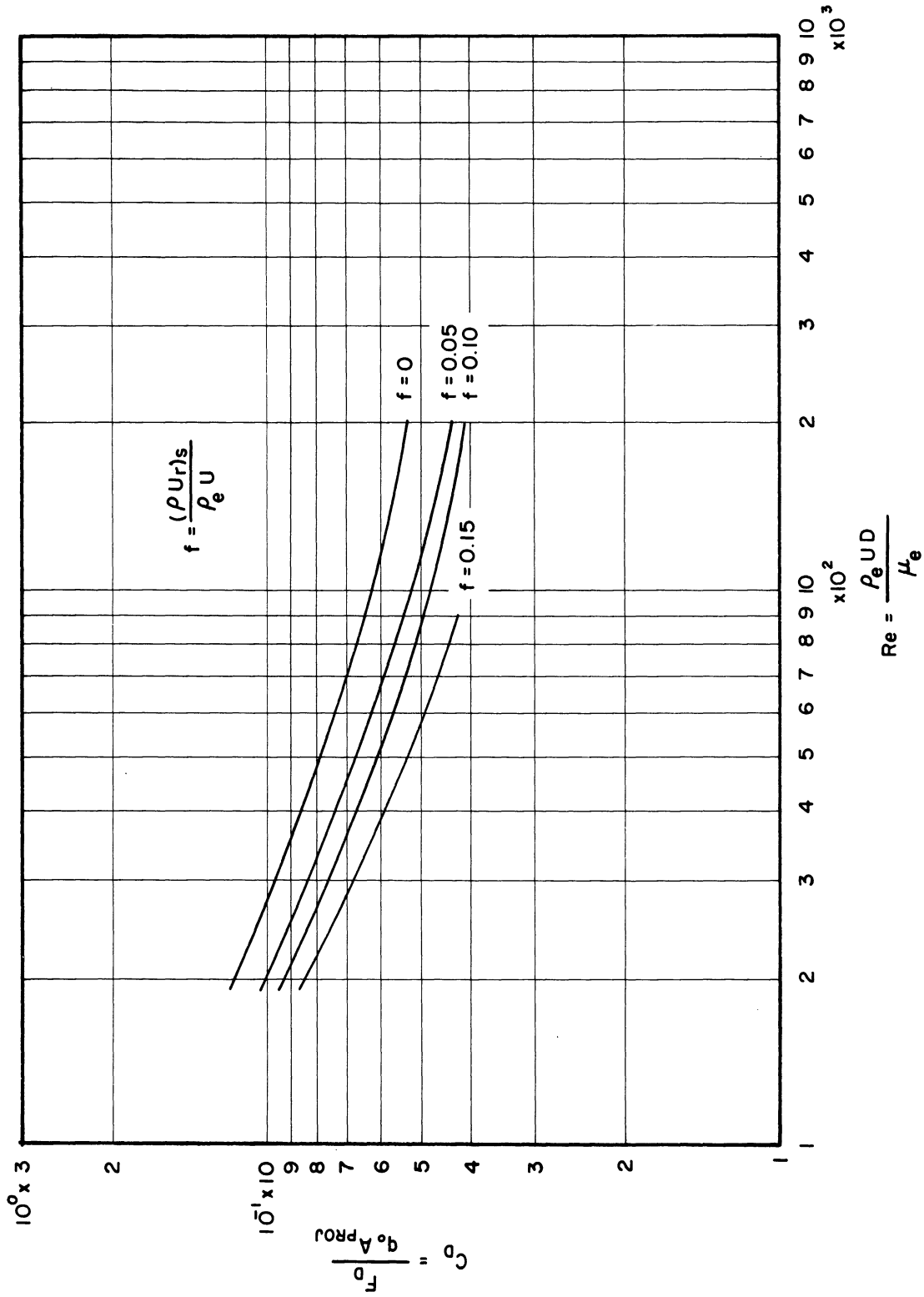


Figure 26. Theoretical Drag Coefficient vs. Reynolds Number for a Burning Particle.

ranging from 0 to 0.15. The value $f = 0$ corresponds to a hot particle which is not burning. The figure indicates an increase in burning rate tends to reduce the drag coefficient.

5.8 The Effect of Acceleration on Drag Coefficient

The fluid dynamics of an accelerating particle will be altered by the inertial forces introduced due to acceleration. For the present analysis the effect of mass flux from the surface will not be included. In addition, it is assumed that the particle undergoes a constant linear acceleration. Also, because of the incompressible flow assumption to be applied, it seems reasonable to assume the density integral remains invariant with time. Applying these restrictions to Equation (5.23) results in

$$\begin{aligned}
 & -\frac{\partial V_\theta}{\partial t} \rho_e \int_0^{\delta_v} \left(1 - \frac{p}{\rho_e}\right) dq + \left[\frac{\partial}{\partial t} + \frac{1}{a} \frac{\partial U_e}{\partial \theta} \right] \rho_e U_e \int_0^{\delta_v} \left(1 - \frac{p u_\theta}{\rho_e U_e}\right) dq \\
 & \frac{1}{a \sin \theta} \frac{\partial}{\partial \theta} \sin \theta \rho_e U_e^2 \int_0^{\delta_v} \frac{p u_\theta}{\rho_e U_e} \left(1 - \frac{u_\theta}{U_e}\right) dq = \tau_s
 \end{aligned} \tag{5.89}$$

Assuming once again the incompressible inviscid velocity distribution for the free stream and evaluating the integrals as done in Section 5.3 gives

$$\begin{aligned}
 & \frac{B}{A} \frac{a}{U_e} \frac{\partial \bar{z}^2}{\partial t} + \left[2 \left(1 + \frac{B}{A}\right) \frac{\cos \theta}{\sin \theta} - \frac{c}{A} \frac{\alpha d}{U^2} \frac{4}{9 \sin \theta} \right] \bar{z}^2 \\
 & + \frac{\partial \bar{z}^2}{\partial \theta} = \frac{3}{8A} \sin^3 \theta
 \end{aligned} \tag{5.90}$$

where

$$\begin{aligned}
 \bar{z} &= \frac{9}{4} \frac{\sin^3 \theta}{C_t \sqrt{Re}} \\
 \frac{\partial V_\theta}{\partial t} &= \omega \sin \theta
 \end{aligned}$$

Employing the same scheme as above for calculating the constants A and B for a temperature variation through the boundary layer yields

$$C = \frac{T^{0.8} - 1}{0.8} \quad (5.91)$$

For $\bar{T} = 2$, $C = 0.925$. However, for purposes of analysis, a value of $C = 1$ will be used. Substituting the values of A and B used in the previous section reduces Equation (5.90) to

$$\frac{4a}{U_e} \frac{\partial \bar{z}^2}{\partial \bar{t}} + \left[10 \frac{\cos \theta}{\sin \theta} - \frac{\theta}{9} \frac{\alpha d}{U^2 \sin \theta} \right] \bar{z}^2 + \frac{\partial \bar{z}^2}{\partial \theta} = \frac{3}{4} \sin^3 \theta \quad (5.92)$$

This equation is more complex than those obtained above, being a first order linear partial differential equation. It is possible to obtain a characteristic solution by solving two ordinary differential equations and this scheme will be used upon further simplifications.

For the experimental results reported in this paper the relative velocity between the particle and stream did not change over 10 per cent so it is reasonable to say that U_e is a constant with respect to time for the particular case in question. Introducing a characteristic time defined by

$$\tau_c = \frac{U}{\alpha} \quad (5.93)$$

Equation (5.92) can be rewritten as

$$\frac{4}{3} \frac{Ac}{\sin \theta} \frac{\partial \bar{z}^2}{\partial \bar{t}} + \left[10 \frac{\cos \theta}{\sin \theta} - \frac{\theta}{9} \frac{Ac}{\sin \theta} \right] \bar{z}^2 + \frac{\partial \bar{z}^2}{\partial \theta} = \frac{3}{4} \sin^3 \theta \quad (5.94)$$

where $\bar{t} = \frac{t}{\tau_c}$

and $\frac{\alpha d}{U^2} = Ac$ (acceleration modulus)

The above equation can also be written in the form

$$\frac{Ac}{\sin \theta} \frac{\partial \chi}{\partial t} + \frac{3}{4} \frac{\partial \chi}{\partial \theta} = \frac{9}{16} \sin^{13} \theta e^{-2/3 \bar{t}} \quad (5.95)$$

where $\chi = \bar{r}^2 \sin^{10} \theta e^{-2/3 \bar{t}}$

From the theory of first order linear partial differential equations, (for example; reference 40) the characteristic solution can be obtained by solving

$$\frac{\sin \theta d\bar{t}}{Ac} = \frac{4}{3} d\theta = \frac{16}{9} \frac{d\chi}{\sin^{13} \theta e^{-2/3 \bar{t}}} \quad (5.96)$$

Solving the first two members of the equality, one obtains

$$C e^{\frac{3\bar{t}}{4Ac}} = \tan \frac{\theta}{2} \quad (5.97)$$

Equating the second and last member results in

$$\frac{d\chi}{d\theta} = \frac{3}{4} \sin^{13} \theta e^{-2/3 \bar{t}} \quad (5.98)$$

Using Equation (5.97) one finds

$$e^{-2/3 \bar{t}} = C \frac{8Ac}{9} \tan^{-\frac{8Ac}{9}} \frac{\theta}{2} \quad (5.99)$$

Substituting Equation (5.99) into (5.98) and integrating yields

$$\bar{r}^2 \sin^{10} \theta e^{-2/3 \bar{t}} = \frac{3}{4} C \frac{8Ac}{9} \int_0^{\theta} \tan^{-\frac{8Ac}{9}} \frac{\theta}{2} \sin^{13} \theta d\theta \quad (5.100)$$

or

$$\bar{r}^2 = \frac{3}{4} \frac{\tan^{\frac{8Ac}{9}} \frac{\theta}{2}}{\sin^{10} \theta} \int_0^{\theta} \tan^{-\frac{8Ac}{9}} \frac{\theta}{2} \sin^{13} \theta d\theta \quad (5.101)$$

The drag coefficient depends largely on the contribution of the skin friction near $\theta = 90^\circ$ so the expression will be evaluated at this point.

Expanding $\tan \frac{-8Ac}{9} \frac{\theta}{2}$ around $\theta = \pi/2$ in a Taylor series, one finds

$$\tan \frac{-8Ac}{9} \frac{\theta}{2} = 1 - \frac{8Ac}{9} \left(\frac{\theta}{2} - \frac{\pi}{4} \right) + O \left[\frac{Ac}{2} \left(\frac{\theta}{2} - \frac{\pi}{4} \right)^2 \right] \quad (5.102)$$

since $Ac = 0$ (10^{-3}) in the present experiment. The last term in Equation (5.100) may now be approximated by

$$\int_0^{\theta} \tan \frac{-8Ac}{9} \frac{\theta}{2} \sin^3 \theta \, d\theta = \int_{\pi/2}^0 \cos^3 \eta \, d\eta - \frac{8Ac}{9} \int_{\pi/2}^0 \left(\frac{\eta}{2} - \frac{\pi}{4} \right) \cos^3 \eta \, d\eta \quad (5.103)$$

Even though the series is not valid at $\theta = 0$, the error would be small since the contribution to integral in this region is small because of the $\sin^3 \theta$ term. The order of magnitude of the last term in (5.103) is

$$\int_{\pi/2}^0 \left(\frac{\eta}{2} - \frac{\pi}{4} \right) \cos^3 \eta \, d\eta \geq -\frac{\pi}{4} \int_0^{\pi/2} \sin^3 \theta \, d\theta \quad (5.104)$$

Thus it is possible to write

$$(\bar{z}^2)_{\pi/2} \leq \frac{3}{4} \int_0^{\pi/2} \sin^3 \theta \, d\theta \left[1 + \frac{2\pi}{9} Ac \right] \quad (5.105)$$

For the steady state case

$$(\bar{z}^2)_{\frac{\pi}{2}} = \frac{3}{4} \int_0^{\pi/2} \sin^3 \theta \, d\theta \quad (5.106)$$

and Equation (5.10) simplifies to

$$\left(\frac{Cf_0}{Cf} \right)_{\theta=\frac{\pi}{2}} < 1 + \frac{\pi}{9} Ac \quad (5.107)$$

or

$$\left(\frac{C_f - C_{f_0}}{C_{f_0}} \right)_{\theta = \pi/2} \leq \frac{-\pi}{9} Ac \quad (5.108)$$

Equation (5.108) indicates the effect of acceleration on the skin friction coefficient is the order of 0.03% in the present experiments. Assuming acceleration will not appreciably alter the characteristics of the wake the accelerative effect on drag coefficients is negligible.

Equation (5.108) is valid for other experimental conditions so long as the three assumptions are applicable, namely:

$$\begin{aligned} \frac{\partial}{\partial t} (\text{relative velocity}) &\approx 0 \\ \alpha &= \text{constant} \\ \frac{\partial}{\partial t} \int_0^{\delta} \left(1 - \frac{y}{\delta}\right) dy &\approx 0 \end{aligned}$$

Equation (5.90), however, may be used equally well to consider other sets of conditions.

VI. DISCUSSION OF THEORETICAL AND EXPERIMENTAL RESULTS

6.1 Comparison of Present Experimental and Theoretical Results

Figures 14 and 15 illustrate the experimental and theoretical results of the present experiment. The steady state drag coefficient for a sphere is included for reference. The spread in the experimental points on both curves was attributed to various factors, some of which were:

- 1) relatively large probable error incurred in data reduction.
- 2) particle rotations. As a particle rotated it was conceivable that the wake characteristics, separation angles, and skin friction distributions differed from the fixed sphere results. Differing rotational magnitudes and directions could have given rise to variations in the drag coefficient.

- 3) boundary layer effects. Using Rayleigh's formula⁽⁴¹⁾ for the velocity profile on a impulsively started plate, it was found there would only be a 2% decrease in velocity at a distance of 1/16" from the wall 6 milliseconds after the shock had passed. It was most unlikely that the particles which were closer than 1/16" to the wall were in sharp focus and recorded in the data. However, it was possible the boundary layer was thicker than indicated by Rayleigh's formula and some of the particles experienced a smaller free stream velocity than used in the drag coefficient calculations.

As noted in Figure 14, the experimental results generally fell below the theoretical curve. There appeared to be several reasons for this discrepancy.

One obvious consideration is the assumption made for the "fullness" of the velocity profile in the theoretical analysis. It is possible the assumption was too severe and a velocity profile somewhere between case II and case III was more representative of the physical problem.

Another reason for the lack of agreement between the analytical and theoretical results was the neglect of the wave attenuation due to the presence of the particles. Would it have been possible to consider this effect for every run it would have amounted, at the very most, to an 8% increase in drag coefficient.

A most simplified model of the pressure distribution around the sphere was used in the theoretical analysis. The inability of the simplified model to correctly represent the physical situation could have accounted for a portion of the discrepancy. A more realistic pressure distribution would have given a decreased pressure drag.

The theoretical and experimental results for the burning particles appeared to agree more favorably than in the case of the non burning particles. The same sources of error are applicable in both cases. However, the particle attenuation effect would have been compensated for by the hot gases in the test section as discussed earlier in section III.

Since it was not possible to measure individually the burning rate of each particle considered, the range of burning rates found for each type of gun powder was employed. This gave a range in theoretical results as shown in Figure 15.

Considering the relative crudeness of the theory employed and the possible experimental errors, the agreement between the analytical and experimental results appeared satisfactory.

It is interesting to note that the drag coefficients found in this study were generally larger than the standard steady state curve for a sphere. As found in the theoretical analysis, the effect of acceleration was too small to account for the larger coefficients and, moreover, would have tended to decrease the drag coefficient. Free stream turbulence, undetermined in the present experiment, could have accounted for increased skin frictions. The alteration of the flow field caused by particle rotations could have created larger pressure drags. Lastly, the existence of roughness on the particle could have yielded a large roughness factor due to the smallness of the particles considered.

6.2 Comparison of Present Results with those of Other Experiments

Figure 2 illustrates the data found by other experimenters in similar studies. The data shows very little agreement and an attempt was made here to ascertain the reasons for discrepancy and correlate them with the results of the present study.

6.2.1 Torobin and Gauvin's data

The fundamental purpose of Torobin and Gauvin's experiments⁽¹³⁾ was to determine the effect of free stream turbulence on the critical Reynolds number for a sphere. Figure 27 gives a more detailed representation of the data they obtained. By creating turbulence intensities, based on the particle's relative velocity, of 40% they were able to show the critical Reynolds number would decrease to approximately 400.

In the subcritical regime the results agreed favorably with those of the present experiments, that is; they fell above the standard drag coefficient curve for a sphere. This correlation supported the

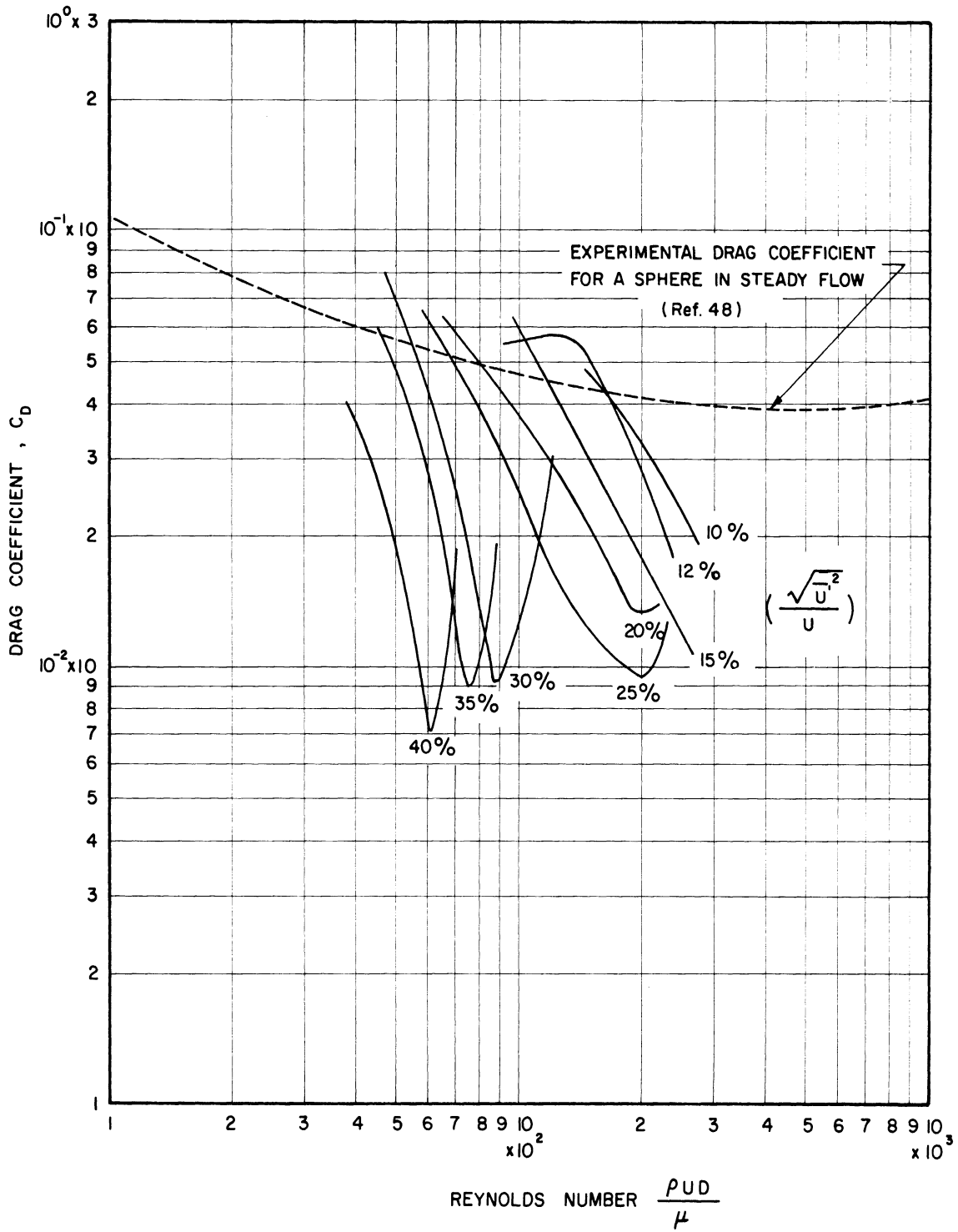


Figure 27. Torobin and Gauvin's Drag Coefficients for Spheres as a Function of Relative Turbulent Intensity.

statement made earlier in regard to turbulence being responsible for the increased drag coefficients. It was also noted that particle rotations, which were immeasurable in both the present and Torobin's experiments, could have contributed to an increased drag coefficient in both sets of experimental results.

The analytical discussion of Torobin's report is presented here since there will be occasion to use the results below.

The goal of Torobin's theoretical studies was to derive a relationship between the relative turbulence intensity and the critical Reynolds number. The basic assumption stated that the critical Reynolds number would occur when the ratio of turbulent energy per unit volume to work done by viscous forces per unit volume attained a definite but unspecified value.

It was assumed that the turbulent energy per unit volume was

$$\rho \overline{u'^2} \tag{6.1}$$

where $\overline{u'^2}$ = mean square of the velocity fluctuations. The viscous work per unit volume was assumed to be

$$\frac{\mu U}{L} \tag{6.2}$$

where

U = relative velocity

L = characteristic length

Taking the sphere diameter as the characteristic length and equating the quotient of the above expressions to a constant gave

$$(Re_c)^{1/2} \left(\frac{\sqrt{\overline{u'^2}}}{U} \right) = \text{CONSTANT} \tag{6.3}$$

Figure 28 shows the agreement between this theoretical relationship and his experimental results.

If the characteristic length were assumed to be the diameter modified by a scale factor of the form

$$L = d Re^n \quad (6.4)$$

an empirical expression, similar to Equation (6.3), would have been obtained, namely

$$Re_c^m \left(\frac{\sqrt{u'^2}}{U} \right) = \text{CONSTANT} \quad (6.5)$$

where $m = \frac{n+1}{2}$. Replotting Torobin's data on log-log paper it was found

$$Re_c^{0.81} \left(\frac{\sqrt{u'^2}}{U} \right) = \text{CONSTANT} \quad (6.6)$$

for $400 < Re_c < 1200$. For the larger critical Reynolds numbers m appeared to approach $\frac{1}{2}$ as predicted by Torobin's theoretical result.

6.2.2 Ingebo's Data

As reported in the introduction, Ingebo⁽¹⁰⁾ found the empirical relationship

$$C_D = 27 Re^{-0.84}$$

held for droplets and small particles accelerating in a gas stream. These results fell well below the steady state results for a sphere and the discrepancy can be attributed to turbulence.

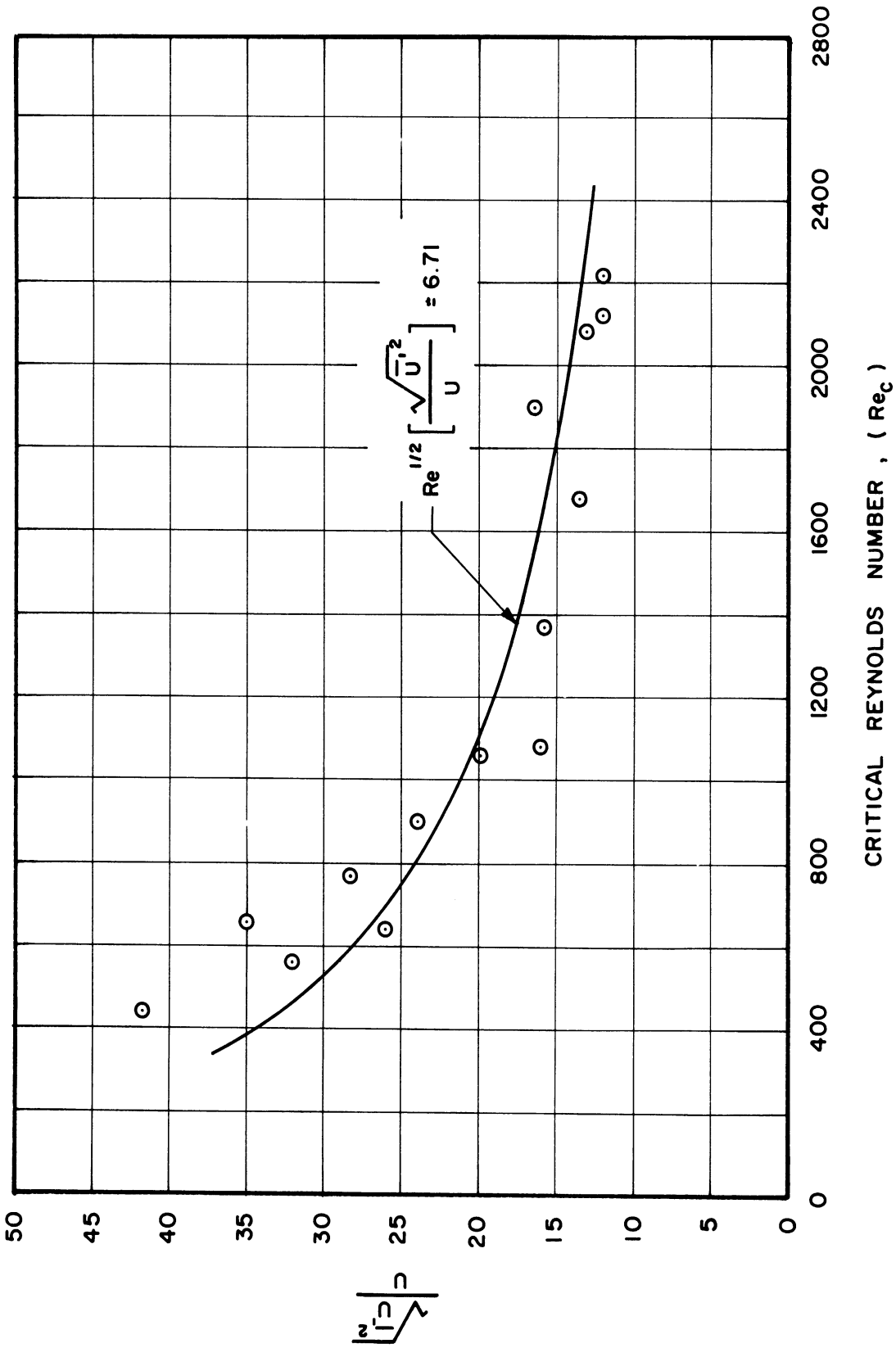


Figure 28. Correlation between Torobin's Theory and Experiment for Effect of Turbulence on Critical Reynolds Number.

In the region of the critical Reynolds number the following formulation for drag coefficient was assumed

$$C_D = 0.3 \left(\frac{Re}{Re_c} \right)^\alpha \quad (6.7)$$

Assuming Torobin's results were valid in the Reynolds number regime of Ingebo's experiments, Equation (6.6) was rewritten as

$$Re_c = \text{CONSTANT} \left(\frac{Re}{Re_0} \right)^{1.235} \left(\frac{\sqrt{u'^2}}{U_0} \right)^{-1.235} \left(\frac{d_0}{d} \right)^{1.235} \quad (6.8)$$

where

Re_0 = Reynolds number when particle velocity is zero

$\frac{\sqrt{u'^2}}{U_0}$ = turbulent intensity based on tunnel flow velocity

U_0

d_0 = particle diameter when velocity is zero.

As a particular example the accelerating isooctone droplets used in Ingebo's experiments were considered. The velocity variation with distance is given in Figure 11 of Reference (10) for a 40 micron drop.

Ingebo employed a 40 x 50 mesh screen to facilitate the drop formation. Turbulence created by the screen would have decayed inversely in proportion to the square root of distance from the screen for approximately a distance equivalent to 200 mesh sizes⁽⁴²⁾, or

$$\frac{\sqrt{u'^2}}{U_0} \propto \frac{1}{x^{1/2}} \quad 0 < \frac{x}{M} < 200 \quad (6.9)$$

where M = size of a single mesh. Consequently, for the particular case in question here, this decay law was valid up to 4" from the screen.

The isooctane droplet travelled this 4 inch distance in roughly 3 milliseconds. Reference (43) indicated the diameter of the drop will change, at most, by 6% and this change was neglected.

Evaluating the velocity variation with distance given in Figure 11 of Reference (10) it was found that the relative velocity varied roughly with the inverse of the distance, or

$$Re \propto \frac{1}{x} \quad (6.10)$$

since the diameter, density, and viscosity were assumed invariant.

Combining Equations (6.9) and (6.10) to eliminate the distance variable yielded

$$\frac{\sqrt{u'^2}}{U_0} \propto Re^{1/2} \quad (6.11)$$

The critical Reynolds number was then expressed as

$$Re_c = \text{const } Re^{0.617} \quad (6.12)$$

Substituting Equation (6.12) into (6.7) gave

$$C_D = \text{const } Re^{0.383\alpha} \quad (6.13)$$

From Torobin's experiments, a reasonable value for α appeared to be

$$\alpha = -2.1 \quad (6.14)$$

Substitution in Equation (6.13) yielded

$$C_D \propto Re^{-0.805} \quad (6.15)$$

This exponent was reasonably close to that obtained experimentally by Ingebo and suggested the discrepancy between his results and those of the present experiment could have been attributed to turbulence.

6.2.3 Rabin's Data

Rabin's results⁽¹²⁾ agreed favourably well with the present data for Reynolds numbers of about 300. As the Reynolds number increased the drag coefficients increase accordingly and diverge from the steady state results for a sphere.

In calculating the drag coefficients, Rabin used, as a representative area, the projected area of the droplet before deformation by aerodynamic forces.* From the photographs presented in his report it appeared the drops deform towards the configuration of a disc normal to the flow. This would have caused a larger projected area and, correspondingly, a smaller drag coefficient. Should this projected area have been used his results would have approached those of the present experiment. However a perfect correlation would not have been expected since the deformed drops were a different aerodynamic shape than the particles used in the present study and the drag coefficients would have correspondingly differed.

* Private communication with author.

An interesting feature of Rabin's results was the larger drag coefficients for the non burning drops. This appeared to substantiate the theoretical results of section V which indicated a smaller drag coefficient for burning particles.

Rabin's results for the low Reynolds numbers agree quite well with Ingebo's results and this may also have been due to the free stream turbulence creation of the critical Reynolds number regime.

6.2.4 Hanson's Results

The drag coefficient obtained experimentally by Hanson⁽¹¹⁾ fell well below the steady state drag coefficient for a sphere.

The theoretical analysis of section V indicated the effect of droplet evaporation could not account for such a discrepancy. Rewriting Equation (5.65) one finds

$$\frac{\Delta C_f}{C_f} < - \frac{0.28 \Delta C}{S_c^{2/3} (1-C_s)^{2/3}} \quad (5.65)$$

where c_e is assumed zero. Under the conditions of Hanson's experiments

$$\Delta C = 0.58$$

$$1-C_s = 0.42$$

$$S_c = 2.08$$

Substitution of these values into (5.65) gave

$$\frac{\Delta C_f}{C_f} < -17.7\%$$

The effect on drag coefficient would have been less. It must be remembered that the above equation is not strictly valid either for the comparatively large vapor concentrations at the surface or the Reynolds number regime of Hanson's experiments but should produce indicative results.

Hanson's results were most likely low as a result of assumptions he used in the data reduction, namely; the applicability of Frössling's equation to determine drop velocity and the invariance of the free stream velocity through the droplet cloud. Other experimenters⁽⁴⁴⁾ have found larger values for the empirical coefficient of $Re^{1/2} Sc^{1/3}$ in Frössling's equation. Using this larger coefficient would have given larger values for droplet velocities and hence smaller relative velocities. Also it seems likely the velocity of the gases encountered by the droplet cloud would have been reduced due to the momentum loss to the droplets. Combining both these effects would have given a smaller relative velocity and perhaps accounted for much of the discrepancy in data.

6.2.5 Balloon experiments

The purpose of the balloon experiment, as stated above, was to obtain a drag coefficient when the acceleration modulus was the order of one. The result was

$$C_D = 0.365 \quad \text{at} \quad Re = 20,800$$

The corresponding steady state value for the sphere in steady flow at this Reynolds number is 0.45. The acceleration modulus being one caused a discernible reduction in drag coefficient and substantiates the importance of the acceleration modulus as a parameter of the drag coefficient. An increase in drag coefficients for balloons accelerating into air at rest

was found by Schmidt in 1920⁽⁴⁵⁾. This increase was to be expected since the acceleration and relative velocity vectors were of opposite sense.

6.2.6 Bolt's Results

No theory exists at present for drag coefficients of burning drops in the Stokes's flow regime. Also Bolt's work⁽¹⁴⁾ appeared to be the only experimental work for drag coefficients of burning particles for Reynolds numbers less than one. Consequently comparison with theory or other results is not possible at this time. It is interesting to note, however, that the usual trend was apparent; reduction of drag coefficient due to burning.

VII. CONCLUSIONS

The purpose of this study was to determine the drag coefficients of reacting particles accelerating in gas streams. The information gained herein was then to be applied to the two phase flow problems in rocket nozzles as discussed in the introduction.

There are five major effects which could influence the drag coefficients of small reacting particles, namely; Reynolds number, acceleration modulus, non dimensional burning or evaporation rate, Knudsen number and Mach number. In this study only the first three were considered. For the other effects, continuum, incompressible flow was assumed. Consequently the present report may only be considered a preliminary attempt to solve the complete problem which would include all five major effects and the interaction of each.

7.1 Reynolds Number Effect

The Reynolds number range investigated in this study extended from 263 to 1610. It was predicted theoretically and experimentally observed that the drag coefficients of reacting and non reacting particles decrease with increasing Reynolds number. The variation with Reynolds number was similar to that for a sphere in steady flow.

7.2 Acceleration Modulus Effect

The theoretical studies indicated a decrease in drag coefficient with increasing acceleration moduli. In particular it was shown that

$$\left(\frac{\Delta C_f}{C_f} \right)_{\theta = \frac{\pi}{2}} < -\frac{\pi A_c}{9}$$

where

$$A_c = \frac{\alpha d}{U^2}$$

The acceleration moduli were the order of 10^{-3} in the present experiments and acceleration effects could not be observed. However an experiment with balloons indicated a discernible decrease in drag coefficient over the steady state value for acceleration moduli of the order of 1.

7.3 Evaporation Effect

Theoretically, evaporation will decrease the drag coefficient. When the mass ratio of particle vapor at the surface is much less than one, the following expression was found

$$\frac{\Delta C_D}{C_D} < -\frac{0.28 C_s}{S_c^{2/3}} \quad (S_c \geq 1)$$

Consequently when the above condition is met, the change in drag will be negligible. Experiments performed in other studies bear out this conclusion.

7.4 Burning Effect

The radial mass flux created by burning theoretically reduced the drag coefficient. The most significant parameter in the burning problem was the ratio between the mass flux from the surface and that in the free stream denoted in this study as "f". Conditions applicable to the present experiment were used to determine the effects of burning on the experimental results. A certain degree of correlation was obtained but once again the effect was too small to be definitely distinguished as burning effects.

However it appeared the magnitude of the effects as predicted by theory was applicable to the physical problem.

With the burning and acceleration effects being small it appeared the drag coefficient for a particle should be that for a sphere in steady flow. The experimental results gave generally larger coefficients which was attributed to particle rotations, turbulence, and roughness effects.

7.5 Application to Rocket Exhaust Problem

The information obtained above was applied to the example discussed earlier in the Introduction(8). That is, a seven micron aluminum particle experienced a 2500 feet per second velocity lag at the throat of a nozzle. The chamber conditions were 6670°R and 1000 psia. The molecular weight of the composition was 30.94 lbm-lbm mole⁻¹ and the specific heat ratio was 1.173.

As determined earlier the Reynolds number of the particle at the throat was 266. The density used to determine the Reynolds number was 0.27 pounds per cubic foot.

The acceleration parameter is approximated by

$$Ac = O\left(\frac{\rho_g}{\rho_p}\right)$$

The density of aluminium being 169 pounds per cubic foot gives

$$Ac = O(1.6 \times 10^{-3})$$

From the experimental and theoretical results of this report, it is concluded that acceleration effects can be neglected.

The burning rate for an aluminum particle was estimated from the work of Blockman and Kuehl⁽⁴⁶⁾. Photographing the luminous streaks of burning particles with a high speed shutter they were able to determine burning times by noting the number of frames for which the luminosity persisted. The photograph of an aluminum particle, approximately 50 microns in diameter, indicated a burning time of approximately 1.5 milliseconds. Since there appeared to be no information as to the variation of the burning rate with time or size, it was postulated that

$$r \text{ (burning rate)} \approx \frac{D_0}{t_b}$$

Employing Blockman and Kuehl's data gave

$$r = 1.3 \text{ in/sec}$$

The ratio of mass flux from the surface to that in the free stream is found to be

$$f = 0.027$$

In the theoretical analysis a temperature ratio between the particle surface and stream was taken as 2. Although the same ratio will not necessarily be valid for the aluminium particle the temperature ratio appeared to have little influence and it appears reasonable to apply the results gained therein to the present case. Consequently this value of "f" would correspond to roughly a 5% decrease in drag coefficient.

In the light of the present experimental and theoretical analysis it was found that the steady state drag coefficient for a sphere is a satisfactory drag law to use for reacting particles in a rocket exhaust.

Should more accurate drag coefficients be required in the range of Reynolds numbers between 200 and 1600, the experimental results for a non reacting particle suggested a drag coefficient variation of the form

$$\ln_{10} C_D = 2.586 - 1.705 \ln_{10} Re + 0.2501 (\ln_{10} Re)^2 \quad 200 < Re < 1600$$

In the majority of cases acceleration effects can be neglected due to the very small magnitude of the acceleration modulus.

The effect of burning on the drag coefficient can be estimated by evaluating the ratio of the mass flux from the burning surface to that in the free stream. To do this, information concerning the particle burning rate must be available.

In summation, the results of this study indicate that the particle drag coefficient is insensitive to evaporation, burning, or accelerating effects if;

$$\frac{C_s}{Sc^{2/3}} < 0.1 \quad (Sc \geq 1), \quad Ac < 0.1, \quad f < 0.025$$

If these conditions are satisfied, other factors, such as free stream turbulence, particle rotations, and particle roughness, can have a larger effect on the particle drag coefficient than the mechanisms considered in this study.

7.6 Suggestions for Further Study

As stated above, the present work can be considered a preliminary study considering only certain aspects of the complete problem. Consequently there are many extensions and refinements of the experimental and analytical work which would give rise to most fruitful research.

The experimental technique employed in this study appears to be sufficiently successful to merit its use in further studies. In particular, by using stronger shock waves and a higher speed camera, the effect of Mach number could be investigated. In addition it appears feasible to study rarefied flow effects by using low density gas in the shock tube and smaller particles. This would necessitate using a camera capable of larger magnification.

There are many refinements which could be applied to the experimental techniques used in the present study. Employing particles with larger burning rates would tend to give more discernible burning effects than in the present experiment. Also if it were possible to have the particle ignite before entering the tube, the wave speed could be measured across the test section and would result in a smaller experimental error. A larger tube would reduce the attenuation effects and lead to more reliable experimental results. The use of smaller particles and more sensitive pressure devices to record the passage of weaker shock waves would make it possible to obtain results for lower Reynolds numbers than achieved in the present study.

Although the present study indicated the magnitude of the acceleration modulus of particles in rocket exhausts was very small, it would be of significant academic interest to perform extensive experiments in which the acceleration modulus was of order one. This could be accomplished, perhaps, by accelerating particles in a fluid such as water.

Extensions and refinements of the analytical work presented herein are numerous. The effect of compressibility could be included by

employing a more realistic pressure and velocity distribution over the sphere. It may also be possible to include the effects of slip flow by modifying the boundary conditions. Although the task appears most formidable, it would be most instructive and fruitful to extend the analytical results to the lower Reynolds number regime where the boundary layer thickness is the order of the particle's characteristic length.

Needless to say there is much work yet to be done towards the better understanding of the fluid dynamics of burning or evaporating particles accelerating in gas streams. The above suggestions only represent a few of the areas of future study concerning this most interesting problem.

A P P E N D I C E S

APPENDIX A

EFFECT OF HOT GASES ON SHOCK WAVE AND CONVECTIVE
FLOW VELOCITY IN A SHOCK TUBE

EFFECT OF HOT GASES ON SHOCK WAVE AND CONVECTIVE
FLOW VELOCITY IN A SHOCK TUBE

A crude analysis is to be made as to the effect of the hot gases above the test section on the wave and convective flow velocity.

The model to be used is shown in Figure 29. The shock tube consists of a driver section and two regions in which the speed of sound of the undisturbed gas is different and

$$a_4 > a_0$$

Assume the gases with differing speeds of sound do not mix. Also the assumption is made that the waves are weak.

The condition to be satisfied is flow continuity between regions 1 and 2, or

$$\rho_1 u_{c1} = \rho_2 u_{c2} \quad (A1.1)$$

Assuming an isentropic expansion wave exists between regions 1 and 2 the pressures and densities are related by

$$\frac{P_2}{P_1} = \left(\frac{\rho_2}{\rho_1} \right)^\gamma \quad (A1.2)$$

For weak shock waves (Reference 21)

$$P_3 = P_4 \left(1 + \frac{\gamma u_{c2}}{a_4} \right) \quad (A1.3)$$

and

$$P_1 = P_0 \left(1 + \frac{\gamma u_{c1}}{a_0} \right) \quad (A1.4)$$

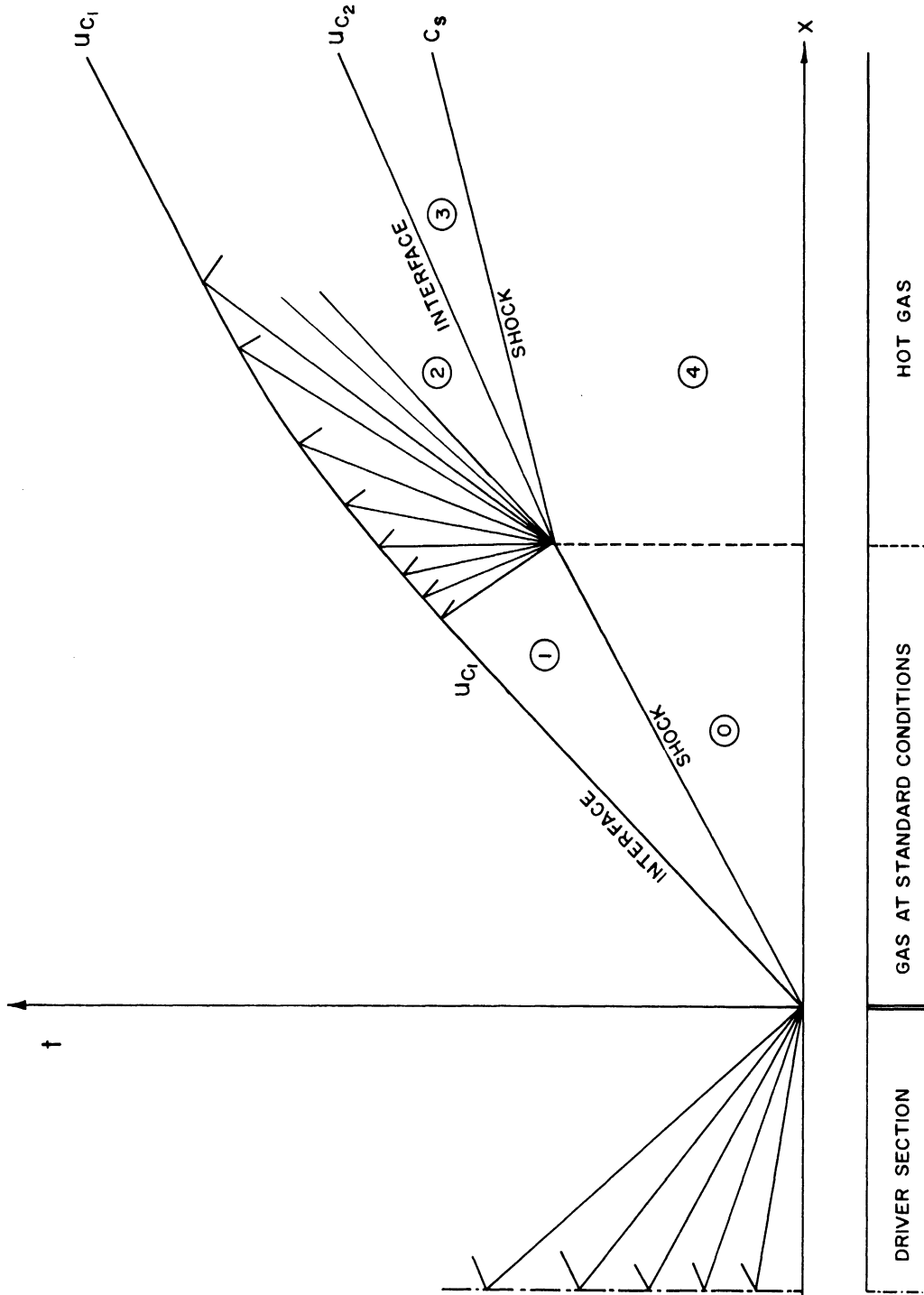


Figure 29. X-T Diagram for Shock Tube with Hot Gas Section.

The pressure across the interface between region 2 and 3 is constant and the pressures of the undisturbed gases in region 0 and 4 are assumed equal, so

$$\frac{P_2}{P_1} = \frac{\left(1 + \frac{\gamma u_{c2}^2}{a_4^2}\right)}{\left(1 + \frac{\gamma u_{c1}^2}{a_0^2}\right)} \quad (A1.5)$$

From Equation (A1.1) and (A1.2) one has

$$\frac{u_{c1}}{u_{c2}} = \frac{\rho_2}{\rho_1} = \left(\frac{P_2}{P_1}\right)^{1/\gamma} \quad (A1.6)$$

Combining Equation (A1.5) and (A1.6) results in

$$\frac{u_{c1}}{u_{c2}} = \left[\frac{1 + \frac{\gamma u_{c2}^2}{a_4^2}}{1 + \frac{\gamma u_{c1}^2}{a_0^2}} \right]^{1/\gamma} \quad (A1.7)$$

As stated in section III, the temperature ratio between the gas above the test section and that below is approximately 2. Thus it follows

$$a_4 = \sqrt{2} a_0 \quad (A1.8)$$

Typical values for the present set of experiments are

$$\begin{aligned} u_{c1} &= 200 \text{ ft/sec} \\ a_0 &= 1140 \text{ ft/sec} \\ \gamma &= 1.4 \end{aligned}$$

Substituting these values into Equation (A1.7) and solving graphically yielded

$$u_{c2} = 230 \text{ ft/sec}$$

Thus the convective flow velocity increases by 30 ft/sec

Using these values of convective flow velocities in the weak shock relationships gives accordingly

$$c_{s1} = 1202 \text{ ft/sec}$$

and

$$c_{s2} = 1687 \text{ ft/sec}$$

The wave speed increases by 485 ft/sec in the hot gases.

APPENDIX B

ORDER OF MAGNITUDE ANALYSIS
ON GOVERNING EQUATIONS

ORDER OF MAGNITUDE ANALYSIS

ON GOVERNING EQUATIONS

An order of magnitude analysis will be performed on the general equations to obtain the governing equations used in section V. The three equations to be considered are:

species continuity equation

$$\frac{\partial}{\partial t}(\rho c_k) + \frac{\partial}{\partial x_\alpha} (\rho u_{\alpha,k} c_k) = W_k \quad (A2.1)$$

overall continuity

$$\frac{\partial \rho}{\partial t} + \frac{\partial}{\partial x_\alpha} (\rho u_\alpha) = 0 \quad (A2.2)$$

momentum equation

$$\rho \frac{\partial v_i}{\partial t} + \frac{\partial}{\partial t} (\rho u_i) + \frac{\partial}{\partial x_\alpha} (\rho u_i u_\alpha) = -\frac{\partial p}{\partial x_i} + \frac{\partial}{\partial x_\alpha} (\tau_{i\alpha}^V + \tau_{i\alpha}^D) \quad (A2.3)$$

If no chemical reaction occurs in the flow, Equation (A2.1) becomes

$$\frac{\partial}{\partial t} (\rho c_k) + \frac{\partial}{\partial x_\alpha} (\rho u_{\alpha k} c_k) = 0 \quad (A2.4)$$

The species flow velocity, u_{ik} , is the sum of the mass averaged velocity, u_i , and the species diffusional velocity.

$$u_{ik} = u_i + u_{ik}^D \quad (A2.5)$$

The diffusional velocity is a function of diffusion coefficients and gradients in concentrations, pressure and temperature as well as external forces. For purposes of an order of magnitude analysis, however, assume Fick's law is valid and write

$$u_{ik}^D = -D \nabla \ln c_k$$

Substituting this expression for diffusional velocity into Equation (A2.4)

gives

$$\frac{\partial}{\partial t} (\rho c_k) + \frac{\partial}{\partial x_\alpha} (\rho c_k u_i) = \frac{\partial}{\partial x_\alpha} \left(\rho D \frac{\partial c_k}{\partial x_\alpha} \right) \quad (A2.7)$$

Introducing the non dimensional variables

$$\bar{x}_i = \frac{x_i}{L} \quad u_i = \frac{u_i}{U} \quad \bar{\rho} = \frac{\rho}{\rho_0} \quad \bar{p} = \frac{p}{\rho U^2} \quad \bar{t} = \frac{tU}{L} \quad \bar{\mu} = \frac{\mu}{\mu_0} \quad \bar{D} = \frac{D}{D_0}$$

where

L = characteristic length

U = relative velocity between particle and gas

$$\bar{U} = \frac{\partial U}{\partial t}$$

into Equations (A2.1), (A2.2) and (A2.7) gives

$$Ac \frac{\partial \bar{p}}{\partial \bar{t}} + \frac{\partial}{\partial \bar{x}_\alpha} (\bar{\rho} \bar{u}_\alpha) = 0 \quad (A2.8)$$

$$Ac \frac{\partial}{\partial \bar{t}} (\bar{\rho} c_k) + \frac{\partial}{\partial \bar{x}_\alpha} (\bar{\rho} \bar{c}_k \bar{u}_\alpha) = \frac{1}{Re Sc} \frac{\partial}{\partial \bar{x}_\alpha} \left(\bar{\rho} \bar{D} \frac{\partial c_k}{\partial \bar{x}_\alpha} \right) \quad (A2.9)$$

$$Ac \left[\bar{\rho} \frac{\partial \bar{v}_i}{\partial \bar{t}} + \frac{\partial}{\partial \bar{t}} (\bar{\rho} \bar{u}_i) \right] + \frac{\partial}{\partial \bar{x}_\alpha} (\bar{\rho} \bar{u}_\alpha \bar{u}_i) = - \frac{\partial \bar{p}}{\partial \bar{x}_i} + \frac{1}{Re} \frac{\partial}{\partial \bar{x}_\alpha} \bar{\tau}_{i\alpha}^V + \frac{1}{(Re Sc)^2} \frac{\partial}{\partial \bar{x}_\alpha} \bar{\tau}_{i\alpha}^D \quad (A2.10)$$

where

$$Ac = \frac{UL}{U^2}$$

$$Re = \frac{\rho_0 UL}{\mu_0}$$

$$Sc = \frac{\mu_0}{\rho_0 D_0}$$

Apply the equation to a boundary layer on a sphere in which the diffusional and velocity boundary layer thicknesses are much less than the sphere diameter, or

$$\bar{\delta}_v, \bar{\delta}_D \ll 1 \quad \text{where} \quad \bar{\delta} = \frac{\delta}{d} \quad (\text{A2.11})$$

The magnitude of a derivative with respect to distance across the boundary layer is then

$$\frac{\partial}{\partial r} = O\left(\frac{1}{\bar{\delta}}\right) \quad (\text{A2.12})$$

In accordance with the conventional order of magnitude analyses (for example, Reference 42) for boundary layers one writes

$$\bar{c}, \bar{\rho}, \bar{u}_\theta, \bar{p}, \bar{\mu}, \bar{D} = O(1) \quad (\text{A2.13})$$

where \bar{u}_θ = nondimensional velocity in the tangential direction.

Writing out the continuity equation in spherical coordinates for axisymmetric flow, one has

$$\begin{matrix} ? & 1 & & \frac{1}{\bar{\delta}_v} & \cdot & ? & & 1 & & 1 \\ & & & & & & & & & \end{matrix}$$

$$Ac \frac{\partial \bar{\rho}}{\partial t} + \frac{1}{r^2} \frac{\partial}{\partial r} (\bar{\rho} \bar{r}^2 \bar{u}_r) + \frac{1}{r \sin \theta} \frac{\partial}{\partial \theta} (\rho \sin \theta u_\theta) = 0 \quad (\text{A2.14})$$

where the orders of magnitude of the terms are written above. For the unsteady term to be significant, $Ac = O(1)$. In addition, in the second term, $\bar{u}_r = O(\bar{\delta}_v)$ in order that the equation be meaningful.

In the species continuity Equation (A2.9) the largest term on the right is that which contains the second derivative with respect to \bar{r} . Neglecting the other terms one may write:

$$Ac \frac{\partial}{\partial t} (\bar{\rho} c_k) + \frac{1}{r^2} \frac{\partial}{\partial r} (\bar{\rho} r^2 c_k \bar{u}_r) + \frac{1}{r \sin \theta} \frac{\partial}{\partial \theta} (\bar{\rho} c_k \bar{u}_\theta \sin \theta) = \frac{1}{\text{Re Sc}} \frac{1}{r^2} \frac{\partial}{\partial r} (\bar{\rho} D \frac{\partial c_k}{\partial r}) \quad (A2.15)$$

Assuming that the diffusion and velocity boundary layers are not an order of magnitude different; the second term in Equation (A2.15) must be of order one. In addition one must have

$$\text{Re Sc} = O\left(\frac{1}{\delta_D^2}\right) \quad (A2.16)$$

There are two components of the momentum equation to be considered, the normal and tangential components to the surface. In the equation for the tangential momentum balance the largest term in the viscous force expression is: (47)

$$\frac{1}{r^2} \frac{\partial}{\partial r} (r^2 u \frac{\partial u_\theta}{\partial r}) \quad (A2.17)$$

and the corresponding term in the diffusion force relation is

$$\frac{\partial}{\partial r} \rho \sum_{k=1}^n c_k \frac{\partial}{\partial r} \ln c_k \frac{\partial}{\partial \theta} \ln c_k \quad (A2.18)$$

Writing out the tangential component of the momentum equation, one has

$$Ac \left[\bar{\rho} \frac{\partial \bar{v}_\theta}{\partial t} + \frac{\partial}{\partial t} (\bar{\rho} \bar{u}_\theta) \right] + \frac{1}{r^2} \frac{\partial}{\partial r} (\bar{\rho} \bar{u}_r r^2 \bar{u}_\theta) + \frac{1}{r \sin \theta} \frac{\partial}{\partial \theta} (\bar{\rho} \bar{u}_\theta \sin^2 \theta) + \bar{\rho} \frac{\bar{u}_\theta \bar{u}_r}{r} = -\frac{1}{r} \frac{\partial \bar{p}}{\partial \theta} + \frac{1}{\text{Re}} \frac{1}{r^2} \frac{\partial}{\partial r} (\bar{\mu} r^2 \frac{\partial \bar{u}_\theta}{\partial r}) + \frac{1}{(\text{Re Sc})^2} \frac{\partial}{\partial r} \bar{\rho} \sum_{k=1}^n \frac{\partial c_k}{\partial r} \frac{\partial}{\partial \theta} \ln c_k \quad (A2.19)$$

From this equation one finds the Reynolds number must be of the order

$$Re = O\left(\frac{1}{\delta_V^2}\right) \quad (A2.20)$$

to have significant viscous forces. The stress tensor due to diffusional velocities is two orders of magnitude smaller than the rest of the terms and can be neglected. In addition the Coriolis acceleration term can be neglected.

The equation for the normal component of momentum may be written

$$\begin{aligned} & \text{as} \\ & \frac{1}{r^2} \frac{\partial}{\partial t} (\rho \bar{u}_r) + \frac{\partial}{\partial t} (\bar{\rho} \bar{u}_r) + \frac{1}{r^2} \frac{\partial}{\partial r} (\bar{\rho} \bar{u}_r^2 r^2) + \frac{1}{r \sin \theta} \frac{\partial}{\partial \theta} (\bar{\rho} \bar{u}_\theta \bar{u}_r \sin \theta) \\ & - \frac{\bar{\rho} \bar{u}_\theta^2}{\bar{r}} = -\frac{\partial \bar{p}}{\partial \bar{r}} + \frac{1}{Re} \frac{1}{\bar{r}^2} \frac{\partial}{\partial \bar{r}} (r^2 \mu \frac{\partial \bar{u}_r}{\partial \bar{r}}) + \frac{1}{(\text{Re Sc})^2} \frac{\partial}{\partial \bar{r}} \left(\bar{\rho} \sum_{k=1}^n \frac{\partial c_k}{\partial \bar{r}} \frac{\partial \ln c_k}{\partial \bar{r}} \right) \end{aligned} \quad (A2.21)$$

Retaining only the significant terms yields

$$\frac{\partial \bar{p}}{\partial \bar{r}} = O(1) \quad (A2.22)$$

or

$$\frac{\partial \bar{p}}{\partial \bar{r}} = O\left(\frac{\rho \bar{u}^2}{L}\right) \quad (A2.23)$$

Thus the basic equations to be used for the analysis are

$$\frac{\partial \rho}{\partial t} + \frac{1}{r^2} \frac{\partial}{\partial r} (\rho r^2 u_r) + \frac{1}{r \sin \theta} \frac{\partial}{\partial \theta} (\rho u_\theta \sin \theta) = 0 \quad (A2.24)$$

$$\begin{aligned} & \frac{\partial}{\partial t} (\rho c_k) + \frac{1}{r^2} \frac{\partial}{\partial r} (\rho c_k u_r r^2) + \frac{1}{r \sin \theta} \frac{\partial}{\partial \theta} (\rho c_k u_\theta \sin \theta) = \\ & \frac{1}{r^2} \frac{\partial}{\partial r} (\rho D \frac{\partial c_k}{\partial r}) \end{aligned} \quad (A2.25)$$

$$\begin{aligned} \rho \frac{\partial v_\theta}{\partial t} + \frac{\partial}{\partial t} (\rho u_\theta) + \frac{1}{r^2} \frac{\partial}{\partial r} (\rho r^2 u_r u_\theta) + \frac{1}{r \sin \theta} \frac{\partial}{\partial \theta} (\rho u_\theta^2 \sin \theta) \\ = - \frac{\partial p}{r \partial \theta} + \frac{1}{r^2} \frac{\partial}{\partial r} (r^2 \mu \frac{\partial u_\theta}{\partial r}) \end{aligned} \quad (A2.26)$$

$$\frac{\partial p}{\partial r} = (\rho \frac{U^2}{d}) \quad (A2.27)$$

APPENDIX C

SERIES SOLUTION FOR A NON LINEAR
ORDINARY DIFFERENTIAL EQUATION

SERIES SOLUTION FOR A NON LINEAR
ORDINARY DIFFERENTIAL EQUATION

A series solution will be presented for solution of Equation (5.81) near the stagnation point. Rewriting the differential equation

$$\sin \theta \frac{d\beta^2}{d\theta} + 14 \cos \theta \beta^2 = f \sqrt{\text{Re}} \beta + \frac{3}{4}$$

one notes it is a non linear ordinary equation of the first degree.

Since $\theta = 0$ is a regular singular point of the equation assume a series of the form*

$$\beta = \sum_{j=0}^{\infty} A_j \frac{\theta^j}{j!} \quad (\text{A3.1})$$

Squaring this series yields

$$\beta^2 = \sum_{n=0}^{\infty} \bar{A}_n \frac{\theta^n}{n!} \quad (\text{A3.2})$$

where $\bar{A}_n = \sum_{i=0}^n (i) A_i A_{n-i}$. Differentiating the expression for β^2 with

respect to θ results in

$$\frac{d\beta^2}{d\theta} = \sum_{n=0}^{\infty} A_{n+1} \frac{\theta^n}{n!} \quad (\text{A3.3})$$

* In the theory of ordinary differential equation a series of the form⁽⁴⁹⁾:

$$\beta = \theta^r \sum_{j=0}^{\infty} A_j \frac{\theta^j}{j!}$$

should be assumed. The corresponding indicial equation to determine r cannot be formed for this non linear equation so a value of $r = 0$ will be assumed from physical considerations.

The series representation for sine and cosine are⁽⁵⁰⁾

$$\sin \theta = \sum_{j=0}^{\infty} \frac{\theta^{2j+1}}{(2j+1)!} (-1)^j \quad (\text{A3.4})$$

and

$$\cos \theta = \sum_{j=0}^{\infty} \frac{\theta^{2j}}{(2j)!} (-1)^j$$

Combining the series as dictated by the form of Equation (5.81) gives the following series

$$\sin \theta \frac{d\beta^2}{d\theta} = \sum_{j=1}^{\infty} c_j \frac{\theta^j}{j!} \quad (\text{A3.5})$$

where

$$c_j = \sum_{\tau=0}^{\tau \leq \frac{j-1}{2}} \bar{A}_{j-2\tau} (j-1-2\tau)^j (-1)^\tau$$

and

$$\cos \theta \cdot \beta^2 = \sum_{j=0}^{\infty} \bar{c}_j \frac{\theta^j}{j!} \quad (\text{A3.6})$$

where

$$c_j = \sum_{\tau=0}^{\tau \leq \frac{j}{2}} (-1)^\tau \bar{A}_{j-2\tau} (j-2\tau)^j$$

Substituting the above expressions in the differential equation and collecting like powers of θ^j gives

$$\sum_{j=1}^{\infty} (c_j + 14 \bar{c}_j - f \sqrt{\text{Re}} A_j) \frac{\theta^j}{j!} + 14 C_0 - f \sqrt{\text{Re}} A_0 - \frac{3}{4} = 0$$

To satisfy the above equation for arbitrarily chosen θ it is necessary that

$$14 C_0 - f \sqrt{\text{Re}} A_0 - \frac{3}{4} = 0 \quad (\text{A3.7})$$

and

$$c_j + 14 \bar{c}_j - f \sqrt{\text{Re}} A_j = 0 \quad (\text{A3.8})$$

Using the definition of c_j given above, Equation (A3.7) can be rewritten as

$$14 A_0^2 - f \sqrt{\text{Re}} A_0 - \frac{3}{4} = 0 \quad (\text{A3.9})$$

This equation determines the first coefficient A_0 .

Employing the series representations of c_j and \bar{c}_j in Equation (A3.8) gives

$$\sum_{\tau=0}^{\tau \leq \frac{j-1}{2}} \bar{A}_{j-2\tau} \binom{j}{j-1-2\tau} (-1)^\tau + 14 \sum_{\tau=0}^{j \leq \frac{j}{2}} (-1)^\tau \binom{j}{j-2\tau} \bar{A}_{j-2\tau} = f \sqrt{\text{Re}} A_j \quad (\text{A3.10})$$

For j even this expression becomes

$$\sum_{\tau=0}^{\tau \leq \frac{j}{2}} \bar{A}_{j-2\tau} \left[\binom{j}{j-1-2\tau} + 14 \binom{j}{j-2\tau} \right] (-1)^\tau + 14 (-1)^{\frac{j}{2}} \bar{A}_0 = f \sqrt{\text{Re}} A_j \quad (j \neq 0) \quad (\text{A3.11})$$

while for j odd one finds

$$\sum_{\tau=0}^{\tau \leq \frac{j-1}{2}} \bar{A}_{j-2\tau} \left[\binom{j}{j-1-2\tau} + 14 \binom{j}{j-2\tau} \right] (-1)^\tau = f \sqrt{\text{Re}} A_j \quad (\text{A3.12})$$

Specializing (Ae.12) to $j = 1$ results in

$$15 \bar{A}_1 = f \sqrt{\text{Re}} A_1 \quad (\text{A3.13})$$

or

$$A_1 (30 A_0 - f \sqrt{\text{Re}}) = 0 \quad (\text{A3.14})$$

But it can be shown from Equation (A3.9) that

$$(30 A_0 - f\sqrt{Re}) \neq 0 \quad (A3.15)$$

so

$$A_1 = 0 \quad (A3.16)$$

Realizing that \bar{A}_{odd} is a series of terms which consist of $A_{\text{even}} \cdot A_{\text{odd}}$ products it can be reasoned that all the A_{odd} 's are zero.

The first six A_{even} 's, found from Equation (A3.11), are

$$A_0 = \frac{f\sqrt{Re} + \sqrt{f^2 Re + 42}}{28} \quad (A3.17)$$

$$A_2 = \frac{14 \bar{A}_0}{32 A_0 - f\sqrt{Re}} \quad (A3.18)$$

$$A_4 = \frac{-108 A_2^2 + 88 \bar{A}_2 - 14 \bar{A}_0}{36 A_0 - f\sqrt{Re}} \quad (A3.19)$$

$$A_6 = \frac{-600 A_2 A_4 + 230 \bar{A}_4 - 216 \bar{A}_2 + 14 \bar{A}_0}{40 A_0 - f\sqrt{Re}} \quad (A3.20)$$

$$A_8 = \frac{-1232 A_2 A_6 - 1540 A_4^2 + 448 \bar{A}_6 - 1036 \bar{A}_4 + 400 \bar{A}_2 - 14 \bar{A}_0}{44 A_0 - f\sqrt{Re}} \quad (A3.21)$$

$$A_{10} = \frac{-2160 A_2 A_8 - 5040 A_4 A_6 + 750 \bar{A}_8 - 3192 \bar{A}_6 + 3060 \bar{A}_4 - 1270 \bar{A}_2 + 14 \bar{A}_0}{48 A_0 - f\sqrt{Re}} \quad (A3.22)$$

An attempt shall now be made to prove convergence of the series. In Equation (A3.11) introduce a new coefficient related to \bar{A} by

$$B_{j-2\tau} = \bar{A}_{j-2\tau} \binom{j}{j-2\tau} \quad (A3.23)$$

and rewrite the equations as

$$\sum_{\tau=0}^{\frac{j}{2}} B_{j-2\tau} \left[\frac{j-2\tau}{1+2\tau} + 14 \right] (-1)^\tau = 0 \quad (A3.24)$$

considering first the special case $f\sqrt{Re} = 0$. As j approaches infinity, this expression becomes an infinite series which is convergent and whose sum is zero. From Reference (51) it may be concluded that terms in the series form a null sequence and it is always possible to choose a ν such that

$$B_{j-2\tau} \left[\frac{j-2\tau}{1+2\tau} + 14 \right] < \epsilon \quad \tau < \nu \quad (A3.25)$$

where ϵ is some arbitrarily small number. Therefore one may conclude

$$\frac{B_{j-2\tau+2}}{B_{j-2\tau}} \frac{\left[\frac{j+2-2\tau}{1+2\tau-2} + 14 \right]}{\left[\frac{j-2\tau}{j+2\tau} + 14 \right]} \leq 1 \quad (A3.26)$$

or

$$\frac{B_{j-2\tau+2}}{B_{j-2\tau}} < 1 \quad (A3.27)$$

Rewriting the expression in terms of the \bar{A} 's one finds

$$\frac{\bar{A}_{j-2\tau+2}}{\bar{A}_{j-2\tau}} < \frac{(j+1)(j+2)}{2\tau(2\tau-1)} < \frac{(j+1)(j+2)}{2} \quad (\text{A3.28})$$

Thus one may write

$$\lim_{n \rightarrow \infty} \frac{\bar{A}_{n+2}}{\bar{A}_n} = \frac{n^2}{2} \quad (\text{A3.29})$$

Applying the ratio test for convergence of series (A3.2) it is sufficient that

$$\lim_{n \rightarrow \infty} \frac{\bar{A}_{n+2}}{\bar{A}_n} \frac{\theta^2}{n^2} < 1 \quad * \quad (\text{A3.30})$$

Using Equation (A3.29) in Equation (A3.30) gives

$$\theta < \sqrt{2}$$

Thus the radius of convergence is $\theta < \sqrt{2}$. In addition since (A3.2) represents the square of series (A3.1) it will be concluded that series (A3.1) will also converge in the same radius of convergence.

When $f\sqrt{\text{Re}} \neq 0$ the last term in the sequence is

$$[(j+14)A_0 - f\sqrt{\text{Re}}] A_j + (j+14)(\bar{A}_j - A_0 A_j)$$

Since $A_0 \neq 0$, as j becomes large and the series becomes a infinite series, $f\sqrt{\text{Re}}$ can be neglected in comparison with $j A_0$. Thus the terms \bar{A}_n for n large will tend to have the same convergence characteristics as those in the $f\sqrt{\text{Re}} = 0$ case. Consequently the radius of convergence will be $\theta < \sqrt{2}$.

* The fact that the odd terms are zero has been employed here.

In the computation, however, the series solution was used up to $\theta < 1$ since convergence is slow for $\theta > 1$. These solutions then provided a starting point for Adams method of numerical integration. In order to assess the accuracy of the technique an analytical solution was found for $f\sqrt{\text{Re}} = 0$ and $\theta = \pi/2$ and was found to differ from the result of numerical integration by 2%. This generated a certain amount of faith in the technique.

REFERENCES

1. Wood, A. W. "Metal Combustion in Deflagrating Propellant." Solid Propellant Rocket Research. Academic Press, 1960.
2. Maxwell, W. R., Dickinson, W. and Caldin, E. F. "Adiabatic Expansion of a Gas Stream Containing Solid Particles". Aircraft Engineering, Vol. 18, 1946.
3. Gilbert, M., Davis, L. and Altman, D. "Velocity Lag of Particles in Linearly Accelerated Combustion Gases". Jet Propulsion, Vol. 25, 1955.
4. Carrier, G. F. "Shock Waves in a Dusty Gas". Journal of Fluid Mechanics, Vol. 4, 1958.
5. Kliegel, J. R. "One Dimensional Flow of a Gas-Particle System". IAS Preprint no. 60-5, Jan. 25, 1960.
6. Kliegel, J. R. and Nickerson, G. R. "Flow of Gas-Particle Mixtures in Axially Symmetric Nozzles". Paper no. 1713-61 presented at ARS Propellants, Combustion and Liquid Rocket Conference, April 26-28, 1961.
7. Bailey, W. S., Nilson, E. N., Serra, R. A. and Zupnik, T. F. "Gas Particle Flow in Axisymmetric Nozzle". ARS Journal, Vol. 31, no. 6 1961.
8. Stonecypher, T. E. "Dynamic and Thermal Non-Equilibrium in Two Phase Flow in Rocket Nozzles", Report no. P-60-17, Rohm and Haas Company, Dec. 27, 1960.
9. Brown, B. "Particle Velocity Lag in Metallized Propellants". Paper no. 1607-61 presented at ARS Solid Propellant Rocket Conference, Feb. 1-3, 1961.
10. Ingebo, R. D. "Drag Coefficients for Droplets and Solid Spheres in Clouds Accelerating in Airstreams". NACA TN 3762, 1956.
11. Hanson, A. R. "The Effect of Relative Velocity on Evaporation of a Liquid Fuel Spray". University of Michigan Ph D Thesis, 1951.
12. Rabin, E., Schallenmuller, A. R. and Lawhead, R. B. "Displacement and Shattering of Propellant Droplets" Rocketdyne, AFOSR-TR-60-75, 1960.

13. Torobin, L. B. and Gauvin, W. H. "The Drag Coefficients of Single Spheres Moving in Steady and Accelerated Motion in a Turbulent Fluid". Pulp and Paper Research Institute of Canada and Department of Chemical Engineering, McGill University, Technical Report no. 193, 1960.
14. Bolt, J. A. and Wolf, L. W. "Drag Coefficients for Burning Kerosene Drops" University of Michigan ERI Project no. 2253: 3-6-P, 1954.
15. Lunnon, R. G. "Fluid Resistance to Moving Spheres" Proceedings of the Royal Society, Series A, Vol. 110, 1926.
16. Allen, H. S. "The Motion of a Sphere in a Viscous Fluid". Philosophical Magazine. Series 5, Vol. 50, P. 519, 1900.
17. Basset, A. B. A Treatise on Hydrodynamics, Deighton, Bell and Co., Cambridge, 1888.
18. Pearcey, T. and Hill, G. W. "The Accelerated Motion of Droplets and Bubbles". Australian Journal of Physics, Vol. 9, no. 1, 1956.
19. Schaaf, S. A. and Chambré, P. L. "Flow of Rarefied Gases". Fundamentals of Gas Dynamics. Vol. III of High Speed Aerodynamics and Jet Propulsion. Princeton University Press, 1958.
20. Tsien, H. S. "Superaerodynamics, Mechanics of Rarefied Gases". Journal of Aeronautical Sciences, Vol. 15, no. 12, 1946.
21. Liepmann, H. W. and Roshko, A. Elements of Gas Dynamics. John Wiley and Sons, Inc., 1957.
22. Handbook of Engineering Fundamentals. Eshbach, O. W., (ed.) John Wiley and Sons, Inc., 1952.
23. Penner, S. S. Chemistry Problems in Jet Propulsion, Pergamon Press, 1957.
24. Nusselt, W. "Wärmeübergang, Diffusion and Verdunstung". Zeitschrift für Angewandte Mathematik und Mechanik. Band 10, Heft 2. 1930.
25. Jeffreys, H. and Jeffreys, B. Methods of Mathematical Physics, Cambridge University Press, 1956.
26. Covert, E. E. "Some Approximations to the Solution of the Binary Boundary Layer Problem". Mass. Inst. of Tech. Naval Supersonic Lab. TN 390, 1959.
27. Tomotika, S. "The Laminar Boundary Layer on the Surface of a Sphere in a Uniform Stream". Aeronautical Research Council R & M 1678, 1935.

28. Taneda, S. "Experimental Investigation of the Wake behind a Sphere at Low Reynolds Numbers". Kyushu University, Research Inst. for Applied Mechanics, Vol. 4, p. 99, 1956.
29. Garner, F., Jenson, V. and Kery, R. "Flow Pattern Around Spheres and the Reynolds Analogy". Transactions of the Institution of Chemical Engineers. Vol. 37, no. 4, 1959.
30. Ermisch, H. "Stromungsverlauf und Druckverteilung an Widerstandskörpern in Abhängigkeit von der Kennzahl-Untersuchungen an der Kugel". Abhandlungen aus der Aerodynamischen Institute an der Technischen Hochschule Aachen. Heft 6, 1927.
31. Hersch, M. "Experimental Method of Measuring Intensity of Turbulence in a Rocket Chamber". ARS Journal, Vol. 31, no. 1, p. 39, 1961.
32. Fuks, N. A. Evaporation and Droplet Growth in Gaseous Media. Pergamon Press, 1959.
33. Frössling, N. "Über die Verdunstung Fallender Tropfen". Gerland Beitrage Geophysik, Band 52, Heft 1/2, p. 170, 1938.
34. Eckert, E. R. G. Introduction to the Transfer of Heat and Mass. McGraw-Hill Book Co., Inc., 1950.
35. Handbook of Chemistry and Physics. Chemical Rubber Publishing Co. 37th ed., 1955.
36. Huggett, C., Bartley, C. E. and Mills, M. M. Solid Propellant Rockets. Princeton Aeronautical Paperback, no. 2, Princeton University Press, 1960.
37. Kennard, E. H. Kenetic Theory of Gases. McGraw-Hill Book Co. Inc., 1938.
38. Wiley, Jr., C. R. Advanced Engineering Mathematics. McGraw-Hill Book Co. Inc., 1951.
39. Schlichting, H. Boundary Layer Theory. Trans. by J. Kestin. McGraw-Hill Book Co. Inc., 1955.
40. Hildebrand, F. B. Advanced Calculus for Engineers. Prentice Hall, Inc., 1954.
41. Lukasiewicz, J. "Shock Tube Theory and Applications". National Aeronautical Establishment, Canada, Report 15, 1952.
42. Keuthe, A. M. and Schetzer, J. D. Foundations of Aerodynamics, John Wiley and Sons, Inc., 1957.

43. Ingebo, R. D. "Vaporization Rates and Drag Coefficients for Iso-octane Sprays in Turbulent Air Streams" NACA TN 3265, 1954.
44. Garner, F. H. and Suckling, R. D. "Mass Transfer from a Soluble Solid Sphere". American Institute of Chemical Engineers Journal, Vol. 4, no. 1, 1958.
45. Schmidt, F. S. "Zur Beschleunigten Bewegung kugelförmiger Körper in widerstehenden Mitteln". Annalen der Physik, Band 61, Heft 7, 1920.
46. Blockman, A. W. and Kuehl, D. K. "The Use of Binary Light Metal Mixtures and Alloys as Additives for Solid Propellants". ARS Solid Propellant Rocket Conference, paper no. 1595, Feb. 1-3, 1961.
47. Modern Developments in Fluid Mechanics. S. Goldstein, (ed.) Vol. 1, Oxford University Press, 1950.
48. Chemical Engineers' Handbook. J. Perry, (ed.) McGraw-Hill Book Co. Inc., 1941.
49. Rainville, E. D. Intermediate Differential Equations. John Wiley and Sons, Inc., 1959.
50. Kaplan, W. Advanced Calculus. Addison-Wesley Publishing Co. Inc., 1959.
51. Knopp, K. Infinite Sequences and Series, Trans. by Bagemihl, Dover Publications, Inc., 1956.

UNIVERSITY OF MICHIGAN



3 9015 02845 3382